



University
of Glasgow

Qi, Nan (2016) *Modelling of soft tissue and fluid structure interaction with physiological applications*. PhD thesis.

<http://theses.gla.ac.uk/7264/>

Copyright and moral rights for this thesis are retained by the author

A copy can be downloaded for personal non-commercial research or study

This thesis cannot be reproduced or quoted extensively from without first obtaining permission in writing from the Author

The content must not be changed in any way or sold commercially in any format or medium without the formal permission of the Author

When referring to this work, full bibliographic details including the author, title, awarding institution and date of the thesis must be given

UNIVERSITY OF GLASGOW

**Modelling of soft tissue and fluid
structure interaction with physiological
applications**

by

Nan Qi

A thesis submitted in partial fulfillment for the
degree of Doctor of Philosophy

in the
School of Mathematics and Statistics
College of Science and Engineering

April 21, 2016

Declaration of Authorship

I, NAN QI, declare that this thesis titled, ‘modelling of soft tissue and fluid structure interaction with physiological applications’ and the work presented in it are my own. I confirm that:

- This work was done wholly or mainly while in candidature for a research degree at this University.
- Where any part of this thesis has previously been submitted for a degree or any other qualification at this University or any other institution, this has been clearly stated.
- Where I have consulted the published work of others, this is always clearly attributed.
- Where I have quoted from the work of others, the source is always given. With the exception of such quotations, this thesis is entirely my own work.
- I have acknowledged all main sources of help.
- Where the thesis is based on work done by myself jointly with others, I have made clear exactly what was done by others and what I have contributed myself.

Signed: Nan Qi

Date: 21/04/2016

Scientific innovation is built on three pillars, namely; theory, experimentation and modelling.

The theorists are only able to convince themselves.

The experimenters are only doubted by themselves

The poor modellers (like me), however, convince no-one, including themselves.

Abstract

Mathematical modelling is an essential and convenient tool to understand the systemic mechanism of human bodies and to assist the diagnosis and/or the treatment of various diseases. The main objective of this thesis is to develop soft tissue mechanics models and use these to address a number of particular clinical topics, namely, the human iris, the artery and the mitral valve. Important modelling aspects such as fluid-structure interaction, fibre reinforcement, material anisotropy and organ-organ interaction are included.

To avoid the acute closed-angle glaucoma and the buckling of floppy iris syndrome in Descemet's stripping endothelial keratoplasty, three-dimensional linear human iris is studied and the intraocular pressure is found to be a critical factor in determining the involving complications.

Human arteries usually consist of two or more families of collagen fibres in each of the three distinct layers (the intima, the media and the adventitia). One challenge is to explain the recent experimental observation that only one family of (circumferential) fibres exists in the media of the iliac artery. Using an invariant-based fibre-reinforced nonlinear constitutive model, we are able to provide a plausible explanation from the mechanics viewpoint, and show that such fibre architecture achieves the optimal energy or stress distributions. We also find that the axial pre-stretch plays a vital role in different fibre structures.

We finally develop a patient-specific human mitral valve model using the immersed boundary finite element method. A major advantage of this approach is that we can incorporate experimentally based constitutive laws for material properties in a coupled three-dimensional fluid-structure interaction framework. This mitral valve model is extended by coupling with a contractile left ventricular model and a comparative analysis is further conducted.

Acknowledgements

First and foremost, I would like to show my deepest gratitude to my supervisor and dear friend, Prof. Xiaoyu Luo, a respectable, responsible and resourceful scholar, who has provided me with valuable guidance at every stage of my four-year PhD study. Without her enlightening instruction, impressive kindness and patience, I could not have completed my thesis. Her keen and vigorous academic observation and devotion to mathematical biology enlighten me not only in this thesis, but also in my future study. Other than work, we have a lot of connections, e.g. poor sense of direction, enthusiasm for losing things, trying to keep or keeping Squeakers, Honey alive.

My sincere appreciation also goes to Dr. Gao Hao for all his kindness in providing advice when I get depressed by programs and for his assistance on building up the fundamental ideas of various techniques and theories. Thank him for encouraging me not to give up by sharing a lot of his much more horrible experience!

I am also very thankful for the support from Prof. Nick Hill, Prof. Yufeng Nie, Prof. Ray Ogden, Prof. Gerhard Holzapfel and many others senior scholars. I am honoured that you were able to find the time in your busy schedules to read my works and give me valuable advice. I would like to thank the kind host and guidance of Prof. Boyce Griffith during my academic visit to University of North Carolina in Chapel Hill, particularly about the IB/FE framework. I also give special thanks to my group members as being always my strong backbone, especially Xingshuang Ma, Andrew Allan, Wenguang Li, Weiwei Chen, Lei Wang, Xin Zhuan, Danyang Wang, Liuyang Feng, Vytautas Zickus, Muzheng Duan and Ahmed Ismaeel.

I also want to express my appreciation to Prof. Michel Destrade and Dr. David MacTaggart for being my thesis examiners. It is of my great fortune that you would be willing to serve on my thesis committee.

I must thank my officemates Benn Macdonald, Cameline Orlando, Lei Wang, Abdullah Al-Omir, Stefania Mele and others. We shared a lot of happiness (free drinks, magic tricks, fridge and boiler) and sadness (power being cut) in the room 328, Mathematics Building.

I would also like to thank my primary financial sponsor—the Engineering and Physical Sciences Research Council [grant number EP/I029990/1] who paves the way for me to

have all these wonderful experience, and Jim Gatheral Scholarship which funded me to visit America and be able to engage in those productive collaborations.

Please let me express my extreme thanks to my lovely and cherished friends, Weiwei Chen, Yuji Chen, Eway Zhang, Ying Shi, Ermes Toninelli, Saizi Xiao, Junyi Zhang, Laiminzi Li, Beibei Li, Di Xu, Ameneh Asgari, Luis Silva, Ian Murry, Ivor Tiefenbrun and David Blenkinson. Ultimately, let me finish by thanking my families in China for their constant support, my husband Baoqing Sun for his unremitting encouragement and our coming little peanut for (97%) her increasingly strong 'kicking' during the writing up period!

Happy New Year!

Glasgow, Jan. 2016

Contents

Declaration of Authorship	i
Abstract	iii
Acknowledgements	iv
List of Figures	ix
List of Tables	xiv
Abbreviations	xv
List of Publications	xvi
1 Overall introduction	1
1.1 History and brief background	1
1.2 Physiological background	3
1.2.1 The human iris	3
1.2.2 The iliac arteries	4
1.2.3 The mitral valve and the left ventricle	5
1.3 Comparison between imaging modalities	7
1.4 The thesis layout	10
2 Linear and nonlinear elasticity	11
2.1 The concept of strain and deformation	12
2.2 The concept of stress	13
2.3 Linear constitutive equations	14
2.4 Nonlinear constitutive equations	15
2.5 Summary	18
3 Application to human iris	19
3.1 The optimum size of iridotomy to prevent acute angle close glaucoma in a uveitic eye	19
3.1.1 Description of the clinical case	20
3.1.2 Mathematical modelling of the iris bulging	21

3.1.3	Results	23
3.1.4	Discussion and conclusion	25
3.2	Modelling of iris buckling within floppy iris syndrome	28
3.2.1	Iris Buckling Model	30
3.2.2	Model set up	31
3.2.3	Linear buckling analysis	31
3.2.4	Nonlinear static analysis	32
3.2.5	Elastic properties	32
3.2.6	Results	33
3.2.6.1	Buckling analysis for isotropic iris tissue	33
3.2.6.2	Buckling analysis for orthotropic iris tissue	34
3.2.6.3	Post-buckling analysis and angle closure	36
3.2.6.4	Implication for ‘floppy iris syndrome’	37
3.2.7	Discussion and conclusion	38
4	Investigation of the optimal collagen fibre orientation in human iliac arteries	40
4.1	Introduction	40
4.2	Methodology	42
4.2.1	Geometry of a 3D aorto-iliac bifurcation	42
4.2.2	Constitutive κ model	44
4.2.3	Finite element simulation	47
4.3	Criteria to determine the optimal angle	48
4.3.1	Hypothesis I: uniformity factor	48
4.3.1.1	Comparison between the bifurcation and the tube structure	50
4.3.1.2	Effect of the circumferential residual stress	50
4.3.2	Hypothesis II: stress-driven remodelling	54
4.3.3	Hypothesis III: energy-minimisation	57
4.4	Discussion	60
4.4.1	Role of pre-stretch	60
4.4.2	Opening angle in the human iliac artery	61
4.4.3	Adventitia fibre orientation β^A	62
4.4.4	Limitations	63
4.5	Conclusion	64
5	The immersed boundary/finite element method	65
5.1	Models for blood and valve interaction	65
5.2	The IB/FE formulations	67
5.3	The IB/FE numerical scheme	74
5.3.1	Spatial discretizations	74
5.3.2	Lagrangian-Eulerian interactions	76
5.3.3	Temporal discretizations	77
5.4	Summary	78
6	A fluid-structure interaction model of a nonlinear human mitral valve	80
6.1	Introduction	80
6.2	Methodology	83

6.2.1	MV geometrical model	83
6.2.2	Material models	85
6.2.3	Boundary conditions and numerical implementations	86
6.3	Results	88
6.4	Discussion	95
6.5	Conclusion	98
7	Fluid-structure interaction model of human mitral valve within left ventricle	99
7.1	Introduction	99
7.2	Model settings	101
7.2.1	Geometry models of MV and LV	101
7.2.2	Material models of MV and LV	102
7.2.3	Loading conditions	103
7.3	Results	104
7.4	Discussion and Conclusion	107
8	Conclusion and future work	111
	Bibliography	115

List of Figures

1.1	The human eye anatomy, adopted from http://ygraph.com/chart/1597 .	3
1.2	(a) Anatomy of the abdominal aorta and iliac arteries and (b) the schematic graph of human large artery [1].	4
1.3	The schematic graph of human heart, along with details of the mitral valve, adapted from http://www.heartmdinstitute.com/health-topics/heart-disease/447-mitral-valve-prolapse and [2].	6
1.4	The most commonly used imaging planes in CMR: SA (blue), 4C (black) and 2C (red).	8
2.1	A body deforms from its reference configuration \mathcal{B}_0 to its current configuration \mathcal{B}_t . The particle has position vector \mathbf{X} in \mathcal{B}_0 and \mathbf{x} in \mathcal{B}_t relative to origin $o(O)$. $\mathbf{u} = \mathbf{x} - \mathbf{X}$ is the displacement vector. In general O and o need not coincide.	11
2.2	Notation of the Cauchy stress components.	13
3.1	Left UBM: marked iris bombe with the peripheral iris in contact with the cornea in all quadrants, very thin iris measuring approximately 0.3mm. A drainage tube is in situ at the 1 o'clock position. The iris is pointing at the tip of the tube and occluding it, adopted from [3].	21
3.2	The geometry of the model has been scaled from the UBM image in Fig. 3.1: the iris is modelled as a deformable elastic disc with a central circular aperture [4]; the cornea and the lens are assumed to be rigid and impermeable.	22
3.3	Computations of the iris shape as a function of this transiris pressure difference were conducted in the Finite Element software ABAQUS 6.13 (SIMULIA, Providence, RI), assuming the iris to be of uniform initial thickness h with elastic moduli listed in Table 3.1. The elastic stiffness of the iris tissue is represented by its Young's modulus, E , and its compressibility by its Poisson ratio, ν . Three snapshots of the iris deformation as a function of the pressure difference ΔP are presented. The black lines indicate the computational mesh used in simulations and the colour shading indicates the displacement of the iris tissue.	23
3.4	ΔP vs. θ : predicted acute angle θ between the cornea and the iris as a function of pressure difference ΔP for $E = 9.6$ kPa and $E = 0.96$ kPa . . .	24
3.5	ΔP vs. r : predicted radius of PI as a function of the pressure drop for $E = 9.6$ kPa and $E = 0.96$ kPa with corresponding prediction for $\zeta = 1.0$ mPa-s, 1.6 mPa-s, 3.0 mPa-s and 10.0 mPa-s.	24
3.6	The procedure of DSEK showing the anterior chamber of the eye with diseased endothelium on Descemet membrane, adapted from [5].	28

3.7	(a) The side view of a general eye structure; (b) the iris structure with the geometric information, and (c) the three dimensional model of the iris, its relation with (b) is indicated.	30
3.8	The first five buckling modes in the r - θ plane view for the isotropic iris model, in which $E = 4.00$ kPa. The colour indicates the longitudinal displacement.	34
3.9	The first five buckling modes in the r - θ plane view for the orthotropic material model.	35
3.10	The configurations of mode $n = 1$ with cornea shown in the r - z cut-plane view where (a) $\eta = 1.0$ and (b) $\eta = 0.5$. We note that when η is below 0.5, the iris makes contact with the cornea.	36
3.11	The critical IOP for the first buckling mode as a function of the reduction in η	37
3.12	The minimum angle between iris and cornea as a function of the reduction in η	38
4.1	The density of the measured angles of fibre families for the descending thoracic aorta T, the abdominal aorta A and the common iliac arteries CI. The three columns are for (a) intima, (b) media and (c) adventitia. The degree of the fibre angle is measured with respect of the circumferential direction of the arteries. The grey box highlights the unusual distribution in the medial layer of CIAs, where the preferred direction of the fibre families is along the circumferential direction. Adapted from [6] with permission.	41
4.2	Three-dimensional geometry of the aorto-iliac bifurcation model. The geometric information is taken from the literature. The inner and outer diameters are chosen to be 14.2 mm and 15.6 mm, respectively, for the abdominal aorta, and 9.3 mm and 10.7 mm, respectively, for the CIAs, following [7] and [8]. The length of the aorta and each iliac artery is taken to be 57 mm [9, 10]. The two iliac branches are assumed to deviate from the centreline of the aorta symmetrically at 30° [11, 12]. The labels ‘C’ to ‘E’ correspond to Fig. 4.3.	43
4.3	Special scheme to connect the aorta and the two iliac branches. We use sequences of ellipses approaching from the aorta in blue (‘D’ to ‘C’) and approaching from one of the iliac branch in black (‘E’ to ‘C’) to mimic the bifurcation neck) . To connect them, we use two sequences of perpendicular semi-ellipses at ‘C’ (highlighted in red in Fig. 4.2) such that the following stacks progressively become flat.	44
4.4	The circumferential and axial stress-stretch responses of (a) the medial and (b) the adventitial layers of a human iliac artery fitted to experimental data. The experimental data shown in symbols (circumferential: circle; axial: square) are from sample no. IV in [13]. The parameters used are listed in Table 4.1.	47
4.5	Transmural stress distribution σ_θ at different medial fibre angle alignments. The x-axis shows the sampling point n from the inner to the outer radius. The curves of the circumferential stress σ_θ are interpolated from the centre points of the finite elements. The thick solid curve at $\beta = 20^\circ$ is shown to be more uniform than all other angles since its UF value is the smallest, as listed at the bottom.	49

4.6	Cylindrical arterial wall in the stress-free configuration Ω_r , the unloaded configuration Ω_0 , and the current configuration Ω_t , replotted following [14].	51
4.7	UF plotted against the fibre angle β^M for the opening angles $\alpha = 0^\circ$ (dashed curve) and $\alpha = 160^\circ$ (solid curve). The optimal fibre angle (solid diamond symbol) shifts from 16° to 0° when the circumferential residual stress is included in the model. Results are obtained for a pre-stretch value of $\lambda_z = 1.07$.	54
4.8	Inverse procedure for determining the fibre orientation using the stress-driven criterion.	54
4.9	(a) The maximal medial fibre angle difference between two successive iterations and (b) the remodelled fibre orientation against the medial layer of the arterial wall at the pre-stretch 1.07. On one hand, all three simulations converge since the angle differences reach to zeros eventually and on the other hand, these convergent results are indistinguishable, in other words, they converge to the same results.	56
4.10	Dependence of the remodelled fibre orientation (characterized by β^M) on the medial radial coordinate r as a function of the axial pre-stretch given as 1.05 (dashed), 1.07 (solid), 1.10 (dash-dotted) and 1.12 (dotted). Residual strains are included through the opening angle of $\alpha = 160^\circ$.	57
4.11	Values of Π^{\min} plotted against β^A and β^M , with the optimum values of the other parameters listed in the table. The red dot indicates the maximum value of Π^{\min} .	58
4.12	Relation between the axial stretch λ_z , internal pressure P , and optimal medial fibre angle β_{opt}^M , as indicated by the colour bar. The black solid line highlights the variation of β_{opt}^M with P at $\lambda_z = 1.07$; for a wide range of pressure ($\beta_{\text{opt}}^M = 0$).	59
4.13	(a) Π^{\min} vs. β^M , with the red dot denoting $\beta_{\text{opt}}^M = 0^\circ$ when Π^{\min} reaches its maximum; (b) Π^{\min} vs. α , with the red dot denoting the optimal position at $\alpha = 45^\circ$ when Π is minimised.	60
5.1	Evolution of a continuum material in IB method. If not specified, capital letters refer to the Lagrangian variables, and small letters refer to the Eulerian ones.	68
5.2	The procedure of prolonging the elastic force density from (a) the Lagrangian nodes onto (b) Gaussian quadrature points and then onto (c) the Cartesian grid.	76
6.1	Procedure to reconstruct the MV geometry from MR images including (a) capture of anterior (blue) and posterior (red) profiles from LVOT images, (b) identification of papillary muscle cap points denoted by two green points, (c) assembly of the segmented curves to get the leaflet surface, reconstruction of the three-dimensional MV model with (d) a spatial annulus ring and (e) the ideal chordal architecture and (f) definition of the fibre structure for the anterior and posterior leaflets.	84
6.2	The saddle shaped mitral annulus is fixed to a non-planar rigid housing disc mounted to a semi-rigid circular tube of length 16 cm (not shown). The chordae are anchored to two papillary attachment points. These structures are all immersed in a cubic fluid box.	86

6.3	A typical human pressure profile, scaled to the subject-specific peak systolic pressure, as used in our simulations. Note that only the rapid diastolic filling and the systolic phases are modelled; see text for further discussion.	87
6.4	The in-plane view of the fluid pressure fields perpendicular to z-axis, when the MV is (a) fully opened, (b) just closed, and (c) fully loaded at the peak pressure.	89
6.5	The fluid velocity fields at the three time instants, corresponding to the ones in Fig. 6.4.	90
6.6	Instantaneous streamlines when the MV is fully opened.	90
6.7	Cine MR images showing the MV shapes (a) at the beginning of the simulation (middle diastole), (b) when fully opened, and (c) just closed. The corresponding MV model predictions are shown in (d, e, f), coloured by displacement.	91
6.8	Flow rate comparison among the predictions of the IB/FE model, the previous IB model [15], and the measurements obtained from the cine MR scan. Note again that only the time period in rapid filling of diastole lasting for 0.2 s can be properly modelled.	91
6.9	The fibre strain when the MV is (a) fully opened, (b) just closed, and (c) fully loaded. The corresponding fibre stress distributions are shown in (d-f), respectively, the stress values are capped at a peak stress of 500 kPa to avoid unrealistic high stress concentrations at the chordal insertion areas.	92
6.10	Three local regions in the anterior leaflet are selected for quantitative stress analysis.	93
6.11	Deformed MV models (a) without chordae, and (b) with chordae at the time when the MVs are fully opened. The corresponding deformations right before the models (c) without chordae, and (d) with chordae break down, respectively. The black arrows in (c) indicate the prolapse regions.	94
7.1	(a)The short-axis view gives one extraction of LV wall boundary; (b) the long-axis view provides the positional information of MV and LV; (c) the rebuilt LV geometry superimposed on one MR image and (d) the fibre architecture of MV and LV are depicted.	101
7.2	The sketches of (a) the MRI-derived MV-LV model, and (b) the MV-tube model, adopted from [16].	102
7.3	Cine MR images showing the MV and LV deformations (a) at the beginning of the simulation, (b) when MV is fully opened, and (c) most closed. The corresponding simulated results are given in (d, e, f), coloured by displacement	104
7.4	The fully opened MV in (a) the MV-LV model, (b) the MV-tube model (b). The most closed MV in (c) the MV-LV model, and (d) the MV-tube model. Coloured by the displacement.	105
7.5	Streamlines in the MV-LV model (a) in the early diastolic filling, (b) in the late diastolic filling, (c) when the MV is closing and (d) at the middle of the systolic ejection. Coloured by the velocity magnitude and adapted from [16].	106
7.6	Streamlines in the MV-tube model (a) in the early diastolic filling, (b) at the late diastolic filling, (c) when the MV is closing and (d) when the MV is fully closed. Coloured by the velocity magnitude and adapted from [16].	107

7.7	The comparison of the flow patterns in LV between the models with and without the MV structure at different time points in diastole. The colour shows the magnitude of velocity.	108
7.8	The vortices compared between the models with and without the MV structure.	109

List of Tables

3.1	<i>Parameters used in the mathematical model.</i>	22
3.2	<i>Minimal PI radius as a function of the viscosity of aqueous humour. The last column A is πr^2, thus the minimal area of PI, which is more applicable clinically.</i>	25
3.3	<i>Critical pressures (mmHg) in the first five modes under different elastic moduli (kPa) in the isotropic case. The buckling modes for $E = 4.00$ kPa are shown in Fig. 3.8.</i>	33
3.4	<i>Critical pressures (mmHg) in the first five modes in the orthotropic case.</i>	35
4.1	<i>Layer-specific material and structural parameters for a human CIA based on the κ model.</i>	47
4.2	<i>Optimal fibre angles with different pre-stretches for the bifurcation and the tube structure.</i>	50
4.3	<i>Geometrical parameters used for the iliac artery, chosen from [6–8]. As no measured opening angle is available for human iliac arteries, the corresponding opening angle of rat is used [1, 17] for both the medial and the adventitial layers.</i>	53
4.4	<i>Minimum value of UF and corresponding β^M obtained for different values of pre-stretch λ_z, when including the opening angle ($\alpha = 160^\circ$).</i>	53
4.5	<i>Optimal medial fibre angle β^M and corresponding UF_{\min} at various values of pre-stretches λ_z for a rabbit carotid artery.</i>	61
4.6	<i>Optimal medial fibre angle β^M at various values of pre-stretches λ_z for human iliac arteries when the opening angle is set to 45°.</i>	62
6.1	<i>Material parameter values for Ψ_{leaflet}</i>	85
6.2	<i>Average regional stresses and strains along the fibre direction on the three local regions defined in Fig. 6.10, again when the MV is fully opened, just closed, and fully loaded.</i>	93

Abbreviations

FEM	finite element method
FDM	finite difference method
MV	mitral valve
LA	left atrium
LV	left ventricle
MR	magnetic resonance
CT	computed tomography
CMR	cardiac magnetic resonance
SA	short-axis
4C	four-chamber
2C	two-chamber
1st PK	first Piola Kirchoff
SEF	strain-energy function
IOP	intraocular pressure
Nd:YAG	neodymium-doped yttrium aluminium garnet
PI	peripheral iridotomy
AACG	acute angle closure glaucoma
PS	posterior synechiae
PTK	penetrating keratoplasty
DSEK	Descemet's stripping endothelial keratoplasty
CIA	common iliac artery
FSI	fluid-structure interaction
ALE	arbitrary Lagrangian Eulerian
FD	fictitious domain
IB	immersed boundary
IB/FE	immersed boundary finite element
AMR	adaptive mesh refinement

List of Publications

- N. Qi, H. Gao, R. W. Ogden, N. A. Hill, G. A. Holzapfel, H. C. Han and X. Y. Luo. Investigation of the optimal collagen fibre orientation in human iliac arteries. *Journal of the Mechanical Behavior of Biomedical Materials*, 52: 108–119, 2015.
- N. Qi, P. S. Stewart, H. M. Wang, H. Gao, N. A. Hill, D. Lockington, K. Ramaesh and X. Y. Luo. Modelling of iris buckling within floppy iris syndrome. (to be submitted).
- N. Qi, Y. F. Nie and W. W. Zhang. Acceleration strategies based on an improved bubble packing method. *Commun. Comput. Phys.*, 16(1):115–135, 2014.
- U. Agrawal, N. Qi, P. S. Stewart, X. Y. Luo, G. Williams, A. Rotchford and K. Ramaesh. Optimum size of iridotomy in uveitis. In *Clinical & Experimental Ophthalmology*, 43(7):692–696, 2015.
- H. Gao, N. Qi, X. S. Ma, B. E. Griffith, C. Berry and X. Y. Luo. Fluid-structure interaction model of human mitral valve within left ventricle. In *Functional Imaging and Modeling of the Heart*, 330–337, 2015.
- H. Gao, X. S. Ma, N. Qi, C. Berry B. E. Griffith, and X. Y. Luo. A finite strain nonlinear human mitral valve model with fluid-structure interaction. *International Journal for Numerical Methods in Biomedical Engineering*, 30:(12) 1597–1613, 2014.
- Y. F. Nie, W. W. Zhang, N. Qi and Y. Q. Li. Parallel node placement method by bubble simulation. *Computer Physics Communications*, 185:(3) 798–808, 2014.
- W. W. Zhang, Y. F. Nie, C. Li and N. Qi. An adaptive discretization of incompressible flow using node-based local meshes. *CMES: Computer Modeling in Engineering & Sciences*, 102:(1) 55–82, 2014.

To my grandmother ☺.

Chapter 1

Overall introduction

1.1 History and brief background

Soft tissue mechanics is the science of force and motion in the soft tissue state, which relates structure to the function at all hierarchical levels: from biomolecules to cells, tissues, organs, and individuals. Human soft tissue is highly deformable and its mechanical properties vary significantly from one person to another. Although a living cell is not a homogeneous continuum, it is a protein machine with internal machinery that functions in an orderly way according to the laws of mechanics [18].

The beginning of biomechanics goes back to more than two millennia ago; the classical Chinese book Huangdi Neijing, or the Yellow Emperor's Inner Classic in the late Warring States Period (475-221 BC) and the book On the Parts of Animals written by Greek scientist Aristotle (384-322 BC) include many theories of biomechanics. In the Renaissance period, many well-known mechanics scientists contributed to this area, e.g. Leonardo da Vinci (1452-1519), Galileo Galilei (1564-1642), Robert Hooke (1635-1703), Isaac Newton (1642-1727), Leonhard Euler (1707-1783), Thomas Young (1773-1829), Simeon Poisson (1781-1840), Louis Navier (1785-1836) and Augustin Cauchy (1789-1857). With the works of George Green (1793-1841), Lord Kelvin (1824-1907) and others, the fundamental mathematical theory was established. More recently, with the fast development of

new science and technology, this area has increasingly become a worth-digging interdisciplinary study; Yuan-Cheng Fung (1919-), particularly, is considered to be the founder of modern biomechanics.

Mathematical models of the biological system, followed by the use of advanced continuum mechanics and efficient, accurate numerical algorithms have allowed applied mathematicians to make significant progresses in the interpretation of the system functionality and dysfunctionality. However, there are numbers of challenges we should think of in modelling, for instance, material property characterization, linear and nonlinear analysis, large deformation modelling, fluid-structure interaction as well as organ to organ interaction.

Forces applied to solids cause deformation, and forces applied to fluid cause flow. Often, the major objective of a mechanical analysis is to find the deformation or the flow, in other words, the displacement, the stress and the strain under given loading and/or boundary conditions. Material models characterize the relationship of the stress and the strain, which is usually determined by the material itself and its surrounding environment. Equilibrium equations of forces give the description of the internal stress in terms of the exterior forces, for example, using Newton's law of motion. The geometry of deformation completes the equation system by adding the compatible relationship of the displacement and the strain.

It is usually hard or even impossible to solve the complex mechanical system involving partial differential equations by purely analytical means and one has to resort to numerical approximations. The finite element method (FEM) is a very powerful tool for numerical analysis in solid and structural mechanics. It subdivides the whole computational domain into simpler finite elements, and the element equations are commonly generated by a weak form as in the Galerkin method. The global system is systematically assembled by all sets of element equations. In contrast to FEM, finite difference method (FDM) is much simpler and easier to implement, and it has a broad application particularly in fluid mechanics. It is based upon the application of a local Taylor expansion to approximate the differential equations and uses a topologically regular network to construct the discretization.

This thesis is driven by specific clinical requests, and focuses on a number of different soft tissue related research topics. These range from linear anisotropic soft tissue mechanics applied to human iris, nonlinear fibre reinforced modelling applied to iliac arteries, and nonlinear anisotropic fluid-structure interaction modelling applied to human mitral valve, to fully coupled left ventricle-mitral valve modelling.

1.2 Physiological background

To help to explain the modelling approaches adopted in this thesis, we first provide some essential background for the physiological problems studied.

1.2.1 The human iris

As shown in Fig. 1.1, the iris is a thin, circular structure in an eye, responsible for controlling the diameter and the size of the pupil and thus the amount of light reaching the retina. The anterior chamber of eyeball is the fluid-filled space inside the eye between the iris and the cornea.

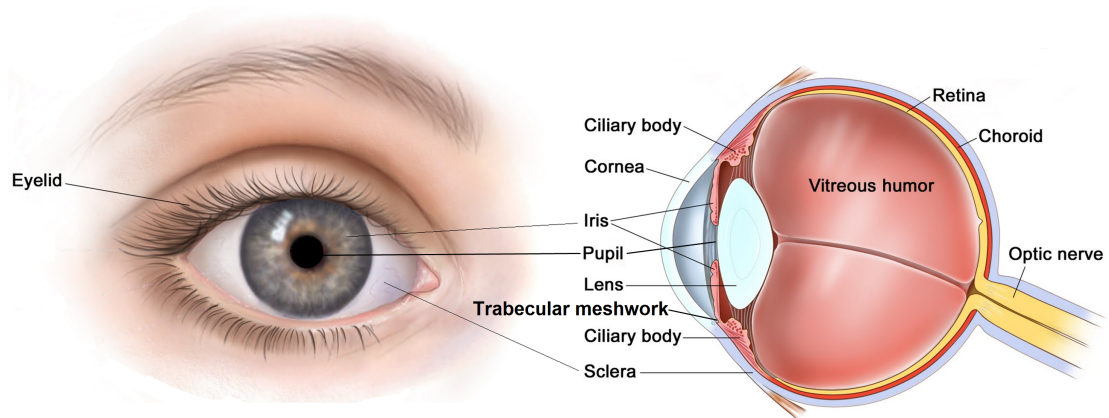


FIGURE 1.1: The human eye anatomy, adopted from <http://ygraph.com/chart/1597>.

A human iris is an important component of an eye, and its many properties need to be explored in some of the most frequently conducted ocular surgeries, such as cataracts, glaucoma and complications that may occur during surgical procedures, e.g. floppy-iris syndrome. Among these, closed-angle glaucoma is an eye disorder in which the iris and

the lens block the movement of fluid between the anterior and posterior chambers of the eye. The blockage of fluid causes pressure to build up in the eye. This causes the iris to press on the drainage system (trabecular meshwork) of the eye. The increased pressure can cause damage to the optic nerve, which leads to severe vision loss and blindness. Treatment may include medicines to lower the pressure in the eye, monitoring of the drainage angle, and possibly surgery [19]. The floppy iris syndrome normally occurs in cataract surgery, and is characterized by a flaccid iris which billows in response to ordinary intraocular flow. This floppy iris prolapses towards the area of cataract extraction during surgery, and further causes progressive intraoperative pupil constriction and other complications [20]. The ophthalmologists at Tennent Institute of Ophthalmology, Gartnavel General Hospital reported two interesting clinical cases regarding to human iris. Here, we develop linear models for iris to study these problems.

1.2.2 The iliac arteries

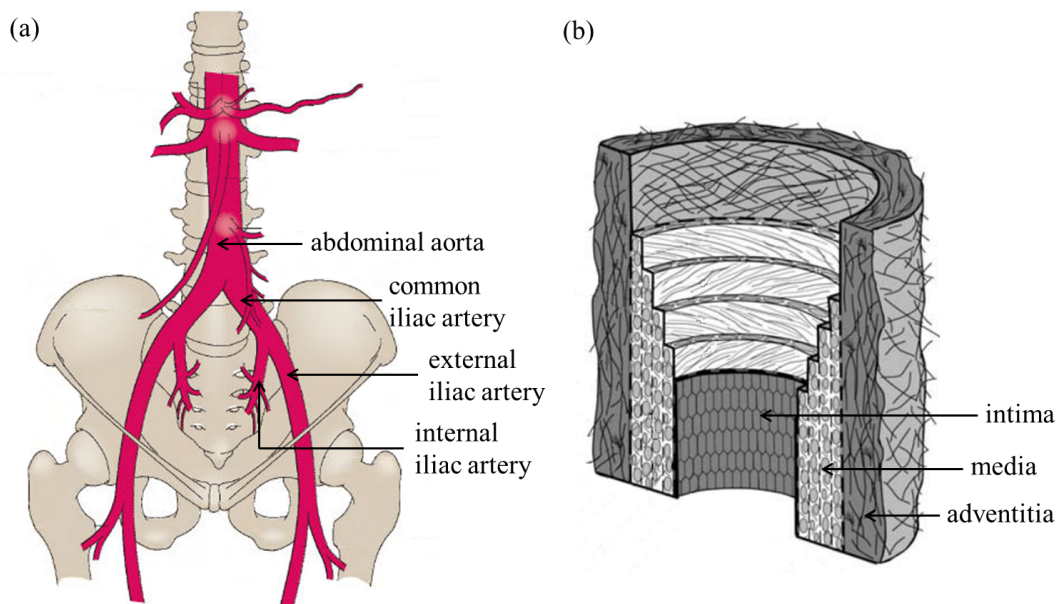


FIGURE 1.2: (a) Anatomy of the abdominal aorta and iliac arteries and (b) the schematic graph of human large artery [1].

In human anatomy, the common iliac arteries are two large arteries that originate from the aortic bifurcation at the level of the fourth lumbar vertebra and bifurcate further into the external and internal iliac arteries, see in Fig. 1.2(a). Aortoiliac occlusive disease is

the narrowing or blockage of the main arteries in the pelvis, which supply blood to the legs. It is a type of peripheral arterial disease which affects arteries that carry blood away from the heart to the head, torso, arms, and legs. Iliac artery angioplasty and selective stent placement for isolated iliac artery stenosis have become the preferred treatments for localized aortoiliac occlusive disease [21].

Large arteries have long been a popular area of biomechanical studies as they are mechanically typical, geometrically simple and relatively easy to harvest. A fundamental knowledge and understanding of the entire arterial histology is required to accurately describe the mechanical behaviour of arterial walls. As many large arteries, common iliac arteries are composed of normally three distinct layers, the intima, the media and the adventitia, see in Fig. 1.2(b). The innermost layer, known as the intima, is made up of one layer of endothelial cells which are in direct contact with the blood flow. It lines the entire circulatory system, from the heart and the large arteries all the way down to the very tiny capillary beds. The medial and adventitial layers are much thicker compared to the intimal layer, and are mechanically significant walls [1]. The muscular middle layer, or media, contains smooth muscle cells and this allows the arteries to constrict and dilate to adjust the volume of blood needed by the tissues. The elastic fibres within the medial layer unite to form lamellae which alternate with the layers of muscular fibres; these lamellae are united to one another by elastic fibres which pass between the muscular bundles, and are connected with the fenestrated membrane of the inner coat. The adventitia is mainly composed of collagen fibrils arranged in helical structures and is supported by external elastic lamellae. It serves to anchor the blood vessel to nearby organs to maintain its stability. The outer two layers are generally reinforced by two or more families of fibres and so are intrinsically anisotropic. Understanding this anisotropy due to the fibre construction is of crucial importance for studying the functionality and diseases of arterial walls.

1.2.3 The mitral valve and the left ventricle

The hearts of large mammals, such as humans, have four heart valves. The mitral valve (MV) is a switch-like membrane sitting between the left atrium (LA) and the left

ventricle (LV). MVs have the largest area between heart valves and bear the highest pressure load during systole. During diastole, the MV opens to allow the blood to enter the LV from the LA. As the LV contracts during systole, blood is pumped out through the aortic valve into the aortic arch and onward to the rest of the body. At the end of atrial contraction, in particular, the MV closes off the LA collecting the oxygenated blood coming in from the lung and prevents a reversal of blood flow.

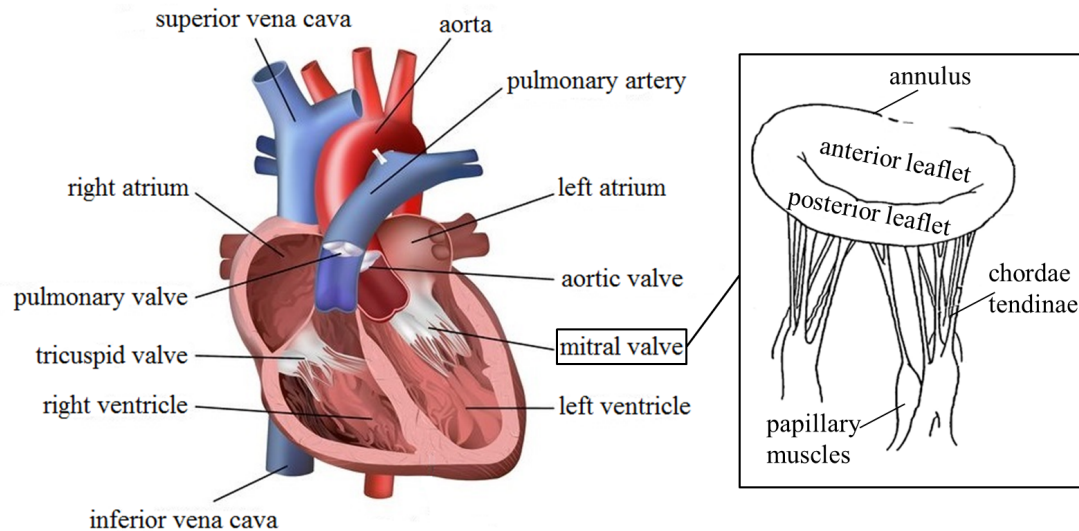


FIGURE 1.3: The schematic graph of human heart, along with details of the mitral valve, adapted from <http://www.heartmdinstitute.com/health-topics/heart-disease/447-mitral-valve-prolapse> and [2].

Shown in Fig. 1.3, the MV has two cusps, the anterior and posterior leaflets. The fibrous ring connecting the MV to the left ventricular wall is known as the annulus. The anterior leaflet rises higher and has a larger area, while the posterior leaflet is narrower and takes up a larger part of the ring. These valve leaflets are prevented from prolapsing into the LA by the action of tendons attached to the posterior surface of the valve, known as the chordae tendinae. The papillary muscles are finger-like extruded muscles from the left ventricular wall and give origin at their apices to the chordae tendinae; they contract to prevent inversion or prolapse of the MV in systole [22]. The LV is the thickest of the heart's chambers; it generates high blood pressure and actively contracts due to ionic signals. Any congenital or acquired disorder of individual components can disturb the finely coordinated mechanism of the MV and the LV and result in an incompetent valve, heart failure and even death [23].

MV cycles roughly 100,000 times/day. More than 300,000 patients each year undergo open-heart surgery to treat malfunctioning or diseased heart valves. Dysfunction of the MV causes significant morbidity and premature mortality and remains a leading medical problem worldwide [24]. According to the recent report from the British Heart Foundation (<https://www.bhf.org.uk/research/heart-statistics>), cardiovascular disease causes more than a quarter of all deaths in UK, or around 155,000 deaths each year—an average of 425 people each day or one every three minutes. Around 41,000 people under the age of 75 in the UK die from cardiovascular disease each year. Understanding the biomechanics of human MV can lead to the development of new therapies and treatment strategies to related diseases, such as mitral regurgitation, mitral prolapse and MV stenosis. Changes in mitral leaflet geometry could perturb the stress patterns and affect repair device durability [25–27]. However, measuring detailed stress patterns in the MV is extremely challenging *in vitro* and nearly impossible *in vivo*. Computational models can fill in this knowledge gap by providing estimated stress patterns from structure-based models of the tissue mechanics, dynamic loading conditions, and *in vivo* deformation [28–30]. Developments of such models are critically required to develop quantitative methods for determining patient-specific medical and surgical strategies for the treatment of valvular heart diseases.

1.3 Comparison between imaging modalities

Before proceeding, let us summarize the current imaging techniques that are utilized as the pre-processing tools in our computation. We rely on those tools to provide more information, e.g. geometry. The development of diagnostic imaging techniques in recent year, has enabled us to meet the growing need for patient-specific and integrated modelling of human organs, and support comprehensive disease diagnoses and intervention planning as well as therapeutic prediction. Amongst these techniques, cardiovascular imaging is the most important [31]. This is in accordance with the enormous efforts worldwide, such like the Virtual Physiological Human framework (<http://vph-institute.org/>) aiming towards the combination of personalised data and population-based representations.

Currently, a variety of non-invasive imaging modalities have been involved in *in vivo* studies, including magnetic resonance (MR) imaging, ultrasound, X-rays, computed tomography (CT) and nuclear imaging. To simplify the presentation, we restrict our attention to the cardiac imaging techniques.

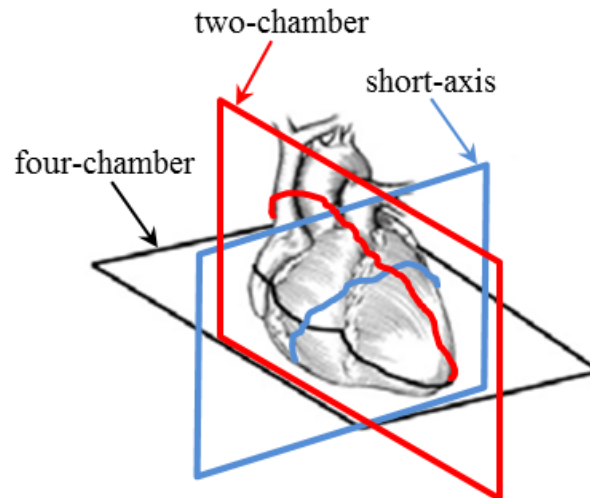


FIGURE 1.4: The most commonly used imaging planes in CMR: SA (blue), 4C (black) and 2C (red).

Cardiac MR (CMR) imaging is a type of scan technique that uses strong magnetic fields and radio waves to visualise the inside of one's heart, and is usually performed along the major axes of the LV. The most frequently acquired orientations in CMR are short-axis (SA) view, four-chamber (4C) view and two-chamber (2C) view, see in Fig. 1.4. Cine CMR can provide both anatomical and functional information of the heart. It produces consecutive frames corresponding to different phases of the cardiac cycle. In cine CMR images, the blood is bright and the tissue is dark, and the contrast between them is usually quite high. Among various acquisition protocols used in CMR imaging, contrast-enhanced MR images offer the capability to directly discriminate infarcted tissue from normal myocardium and also indicate the severity of myocardial injury [32]. Similar to cine CMR, tagged CMR is also a dynamic image so as to provide heart motion; the difference is that tagged CMR gives more direct and accurate quantification of the regional motion and strain.

CMR has been shown to be an accurate and secure tool for the estimation of heart valve motion and blood flow field. It can offer an unrestricted choice of scanning planes together with three-dimensional coverage of the whole heart [33]. Geometric assumptions regarding the shape and size of the heart are therefore not necessarily required in the calculation [34]. In addition, its excellent reproducibility makes temporal follow-up of any individual patient in the clinical setting a realistic possibility [34]. Such technique, however, can be a lengthy and noisy procedure, and is subject to potential inaccuracies caused by patient motion and respiration occurring between images [35].

Echocardiography or echo, another widely available technique, is an ultrasound scan technique of the heart and has the advantage of being relatively inexpensive and safe. It can provide an efficient assessment of global cardiac and valvular function. Two-dimensional and three-dimensional echocardiography combined with Doppler interrogation plays a crucial role in the identification of the MV mechanisms, in the accurate quantification of the severity of mitral regurgitation, and in the assessment of the suitability for repair [36]. Yet, due to its highly dependence on acoustic windows[†], this method has less reproducibility in comparison to MR imaging [34], and its high intraobserver variability is a limitation [37].

Since its introduction, CT has been subject to constant technological improvement and optimization in order to increase its use in everyday medical practice. It makes use of computer-processed combinations of many X-ray images to produce cross-sectional images of specific areas of a scanned object. CT scanning requires less time than MR, it usually allows for a comprehensive assessment within a few minutes [38]. It is useful in the diagnosis of coronary artery diseases due to its high resolution [31]. Similarly as using radiation, during a nuclear cardiology test, a very small amount of radionuclide (radioactive tracer) is injected into a vein and is then taken up by the heart, which is recorded by gamma camera. Nuclear imaging evaluates how organs function, unlike other imaging methods that assess how organs appear. Although these radiation-involved cardiologies are said to provide an accurate assessment of LV function with good reproducibility,

[†]Typically, acoustic windows in cardiac ultrasound scanning involve areas conducive to ultrasound transmission such as the liver, intercostal muscles and chest wall. These structures are hypoechoic and when placed in the near field, facilitate sound transmission (little attenuation or weakening of the signal).

their exposure to ionising radiation (X-rays in CT and gamma-rays in nuclear imaging) is problematic when repeated measurements are required. This increases the risk of cancer in the future, especially for children.

1.4 The thesis layout

The thesis is organized as follows: A brief overview of the linear and nonlinear constitutive laws is summarized in Chapter 2. Chapter 3 presents two specific clinical cases regarding the human iris, and mathematical tools are used to analyse the causes of the complications during ocular surgeries. An unusual phenomenon of the fibre structure in the medial layer of iliac arteries is discussed in Chapter 4. We next derive the mathematical and numerical formulations of immersed boundary finite element method in Chapter 5. In Chapter 6, we model the dynamics and fluid-structure interaction of an image-derived human MV under a physiological pressure loading. A transversely isotropic material constitutive model is used for characterizing the mechanical behaviour of the MV tissue based on recent mechanical tests of healthy human mitral leaflet. Finally, we study the dynamic MV model coupled with a contractile LV chamber, and preliminary results are given in Chapter 7.

Chapter 2

Linear and nonlinear elasticity

In this chapter, we will introduce the mathematical theory used to analyse the mechanical properties of solid materials. Stress and strain are critical and basic concepts to understand continuum mechanics. At the end of the chapter, some popular constitutive equations for elastic biological materials will be discussed.

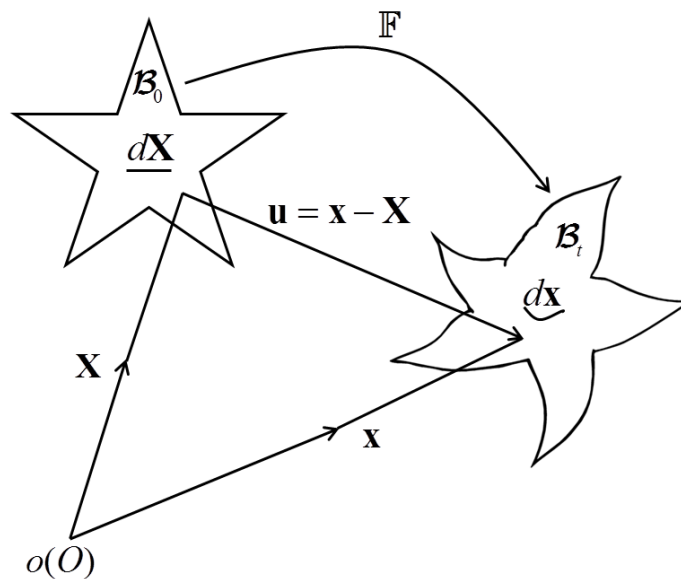


FIGURE 2.1: A body deforms from its reference configuration \mathcal{B}_0 to its current configuration \mathcal{B}_t . The particle has position vector \mathbf{X} in \mathcal{B}_0 and \mathbf{x} in \mathcal{B}_t relative to origin $o(O)$. $\mathbf{u} = \mathbf{x} - \mathbf{X}$ is the displacement vector. In general O and o need not coincide.

2.1 The concept of strain and deformation

We define the relationship between what is known as the reference, or undeformed, configuration \mathcal{B}_0 of a body and the current, or deformed, configuration \mathcal{B}_t , as depicted in Fig. 2.1 [39]. In order to analyse the deformation locally, we use the relationship

$$d\mathbf{x} = \mathbb{F}d\mathbf{X},$$

where

$$\mathbb{F} = \frac{\partial \mathbf{x}}{\partial \mathbf{X}} = \nabla \mathbf{u} + \mathbb{I}$$

is the deformation gradient tensor, \mathbb{I} is the identity tensor, \mathbf{u} is the displacement vector. \mathbb{F} is a second-order tensor and is not necessarily symmetric. It is then convenient to define the Jacobian determinant $J \equiv \det \mathbb{F}$ to be interpreted as the local ratio of the current to the reference volume of a material element. If the local volume of a material in a neighbourhood of each point is constant in time, then we say the material is incompressible and $J = 1$. This is usually being assumed for soft biological tissue, for example arteries [40, 41].

We can now define the *Green* or *Lagrangian finite strain tensor* \mathbb{E} by

$$\mathbb{E} = \frac{1}{2}(\mathbb{F}^T \mathbb{F} - \mathbb{I}).$$

Note that \mathbb{E} is a second-order symmetric tensor. In addition to the finite strain tensor, other deformation tensors are often defined in terms of the deformation gradient. The most used deformation measures are the *right* and *left Cauchy-Green tensors*, defined as:

$$\mathbb{C} = \mathbb{F}^T \mathbb{F}, \quad \mathbb{B} = \mathbb{F} \mathbb{F}^T,$$

respectively. Physically, they give us the square of local changes in distances due to deformation in reference and current configurations, respectively.

From the expression of \mathbb{F} , it follows that $\mathbb{E} = \frac{1}{2}[(\nabla \mathbf{u})^T + \nabla \mathbf{u} + (\nabla \mathbf{u})^T \cdot \nabla \mathbf{u}]$. If we assume the displacement of a material particle is infinitesimally small then the *infinitesimal*

strain tensor is defined by $\boldsymbol{\epsilon}$, so that

$$\boldsymbol{\epsilon} = \frac{1}{2}((\nabla \mathbf{u})^T + \nabla \mathbf{u}) \approx \mathbb{E}.$$

We introduce this as it will be used in Chapter 3 for human iris modelling. Again, $\boldsymbol{\epsilon}$ is a second-order symmetric tensor. Although the stress-strain law in infinitesimal strain theory is linear and much simpler to use, the assumption is not valid for most soft tissues undergoing large deformation.

2.2 The concept of stress

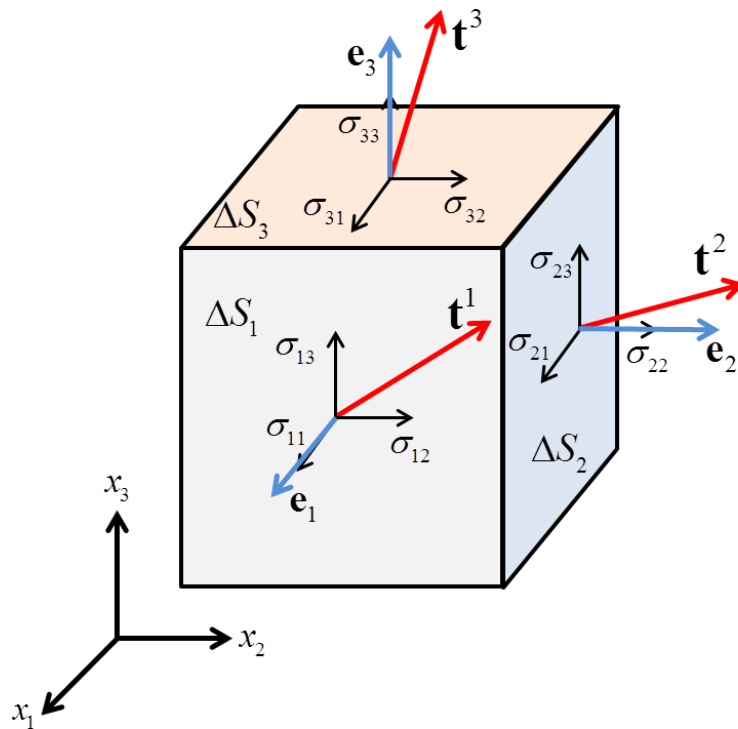


FIGURE 2.2: Notation of the Cauchy stress components.

Stress occurs when forces are applied to a body. Let us consider a three dimensional object in a Cartesian frame (x_1, x_2, x_3) , and a traction force vector \mathbf{t} acting internally on an area of an arbitrary direction; then each traction vector will have three components. For instance, on $\Delta S_i, i = 1, 2, 3$ in Fig. 2.2, the three components $\sigma_{i1}, \sigma_{i2}, \sigma_{i3}$ denote the traction vector \mathbf{t}^i in the directions of the standard vectors $\mathbf{e}_1, \mathbf{e}_2, \mathbf{e}_3$, respectively.

Then $\mathbf{t}^i = \sigma_{ij}\mathbf{e}_j$, $i, j = 1, 2, 3$, where σ_{ij} are known as the *Cauchy stresses*. We assume that the volume of the cube can be sequentially shrunk down to a point if the volume is homogeneous, so that the three components of each of the traction vectors on the cube faces become nine components of the second order Cauchy stress tensor. It is important to note that this stress tensor is symmetric due to the balance of moment and is defined in the deformed state of the material.

Another alternative stress tensors, usually used in large deformation mechanics include the first Piola-Kirchhoff (1st PK) stress tensor. It is expressed via the Cauchy stress by

$$\mathbb{P} = J\boldsymbol{\sigma}\mathbb{F}^{-\text{T}},$$

and the transpose \mathbb{P}^{T} is known as the nominal stress. Note that $\boldsymbol{\sigma}$ denotes the current force over the current area whereas \mathbb{P} denotes the current force over the reference area, and that \mathbb{P} is not necessarily a symmetric tensor.

2.3 Linear constitutive equations

The properties of a material are specified by constitutive equations which describe the nature of the material and the distinct types of material behaviours. The simplest linear constitutive law is Hooke's law, i.e.,

$$\boldsymbol{\sigma} = \mathbf{C}\boldsymbol{\epsilon},$$

where \mathbf{C} is a fourth-order tensor of elastic constants, or moduli, which are independent of stress or strain. Note that the infinitesimal strain tensor $\boldsymbol{\epsilon}$ is only suitable to describe materials in the small strain regime.

The greatest reduction of \mathbf{C} is when the material is isotropic, i.e. when the elastic properties are identical in all directions. In this case, \mathbf{C} involves only two independent elastic moduli, for instance, the elastic modulus E and the Poisson's ratio ν via

$$\sigma_{ij} = \frac{E}{1+\nu} \left[\epsilon_{ij} + \frac{\nu}{1-2\nu} \epsilon_{kk} \delta_{ij} \right], \quad i, j, k = 1, 2, 3. \quad (2.1)$$

where δ_{ij} is the Kronecker delta. If the material is assumed to be incompressible, then $\nu = 0.5$.

Consider an orthotropic material which has three mutually orthogonal axes of rotationally symmetric material properties; then \mathbf{C} has nine independent parameters and its inverse is

$$\mathbf{C}^{-1} = \begin{pmatrix} \frac{1}{E_1} & -\frac{\nu_{12}}{E_2} & -\frac{\nu_{13}}{E_3} & 0 & 0 & 0 \\ -\frac{\nu_{21}}{E_1} & \frac{1}{E_2} & -\frac{\nu_{23}}{E_3} & 0 & 0 & 0 \\ -\frac{\nu_{31}}{E_1} & -\frac{\nu_{32}}{E_2} & \frac{1}{E_3} & 0 & 0 & 0 \\ 0 & 0 & 0 & \frac{1}{G_{23}} & 0 & 0 \\ 0 & 0 & 0 & 0 & \frac{1}{G_{31}} & 0 \\ 0 & 0 & 0 & 0 & 0 & \frac{1}{G_{12}} \end{pmatrix}$$

where E_i and ν_{ij} , $i = 1, 2, 3$ are the elastic moduli and the Poisson's ratios in the three mutually orthogonal directions, $\nu_{ij}/E_i = \nu_{ji}/E_j$, and G_{ij} are the shear moduli [42]. We will use these material properties in Chapter 3.

2.4 Nonlinear constitutive equations

Most living tissues behave nonlinearly and can not be described by the linear theory. Here we are only concerned with pure elastic and homogeneous mechanical theories relating to soft tissues and we exclude other aspects such as plasticity/viscoelasticity and temperature/electrical conductivity. Some of the constitutive equations are phenomenological or experimentally determined, although there are more and more models that are derived from inherent structures of the material and related to morphological aspects of the material, especially for biological tissues [1]. Soft tissues are often modelled via the hyperelastic idealization, for which the stress-strain relationship derives from a strain-energy density function, or a strain-energy function (SEF) Ψ . Thus, we can write a general relationship between various stresses and finite strain tensors using a SEF as

$$\mathbb{P}^T = \frac{\partial \Psi(\mathbb{F})}{\partial \mathbb{F}}$$

or

$$\boldsymbol{\sigma} = \frac{1}{J} \mathbb{F} \frac{\partial \Psi(\mathbb{F})}{\partial \mathbb{F}}. \quad (2.2)$$

For an isotropic material, the SEF is expressible as a function of the principal stretches $\lambda_1, \lambda_2, \lambda_3$ as $\Psi(\lambda_1, \lambda_2, \lambda_3)$. It follows that the principal Cauchy stresses are

$$J\sigma_i = \lambda_i \frac{\partial \Psi}{\partial \lambda_i}, i = 1, 2, 3. \quad (2.3)$$

Instead of using stretches, we can use equivalently the invariants [39] defined by

$$\begin{aligned} I_1 &= \text{tr}(\mathbb{C}) \equiv \lambda_1^2 + \lambda_2^2 + \lambda_3^2, \\ I_2 &= \frac{1}{2}[I_1^2 - \text{tr}(\mathbb{C}^2)] \equiv \lambda_2^2 \lambda_3^2 + \lambda_1^2 \lambda_3^2 + \lambda_1^2 \lambda_2^2, \\ I_3 &= \det(\mathbb{C}) \equiv \lambda_1^2 \lambda_2^2 \lambda_3^2 = J^2. \end{aligned}$$

Therefore, we can get the expression of the Cauchy stress from Eq. (2.2) via

$$\boldsymbol{\sigma} = \frac{1}{J} \mathbb{F} \frac{\partial \Psi(\mathbb{F})}{\partial I_i} \frac{\partial I_i}{\partial \mathbb{F}}, i = 1, 2, 3, \quad (2.4)$$

where the derivatives are

$$\frac{\partial I_1}{\partial \mathbb{F}} = 2\mathbb{F}^T, \quad \frac{\partial I_2}{\partial \mathbb{F}} = 2I_1 \mathbb{F}^T - 2\mathbb{F}^T \mathbb{F} \mathbb{F}^T, \quad \frac{\partial I_3}{\partial \mathbb{F}} = 2I_3 \mathbb{F}^{-1} \quad (2.5)$$

If the considered material is incompressible, Eq. (2.4) is replaced by

$$\boldsymbol{\sigma} = -\varrho \mathbb{I} + \mathbb{F} \frac{\partial \Psi(\mathbb{F})}{\partial I_i} \frac{\partial I_i}{\partial \mathbb{F}}, i = 1, 2, 3. \quad (2.6)$$

where ϱ is a *Lagrangian multiplier*.

The simplest nonlinear SEF, known as the *neo-Hookean* material, has the form

$$\Psi = \frac{c_1}{2}(I_1 - 3), \quad (2.7)$$

where $c_1 > 0$ is the shear modulus of the material in the reference configuration. The chordae tendineae in Chapter 6 and 7 is modelled as a *neo-Hookean* material.

This isotropic elastic response is valid to a limited extent for some biological soft tissues. However, soft tissues usually exhibit anisotropy in their mechanical response. This is associated with distributions of collagen fibres that endow the material locally with preferred directions [1]. In chordae and tendons, for example, the material can be treated as *transversely isotropic*, characterized by a single family of parallel fibres. Other soft tissues have two distinct distributions of collagen fibres with two preferred directions, typically in the layers of an arterial wall. In the following contents, we illustrate the expressions of these two types of anisotropic SEFs.

Let the unit vector \mathbf{a}_0 be along a preferred direction in the reference configuration \mathcal{B}_0 . In general, \mathbf{a}_0 varies with position \mathbf{X} . We then introduce two more invariants I_4, I_5 given by

$$I_4 = \mathbf{a}_0 \cdot (\mathbb{C}\mathbf{a}_0), \quad I_5 = \mathbf{a}_0 \cdot (\mathbb{C}^2\mathbf{a}_0).$$

The direct interpretation of I_4 is as the square of the stretch in the direction of \mathbf{a}_0 ; I_5 is also associated with the fibre stretch but introduces an additional relationship to the behaviour of the reinforcement under shear deformation [43]. So the SEF becomes $\Psi(I_1, I_2, I_3, I_4, I_5)$. Selective invariants are included in various constitutive laws. The mitral valve leaflets simulated in Chapter 6 and 7 uses I_4 to characterise the mechanical contribution from their embedded fibres. Similarly consider the situation in which there are two distinct preferred directions in the reference configuration. Let \mathbf{a}_{01} and \mathbf{a}_{02} be the associated unit vectors. Then, the SEF Ψ additionally depends on [44]

$$I_4 = \mathbf{a}_{01} \cdot (\mathbb{C}\mathbf{a}_{01}), I_5 = \mathbf{a}_{01} \cdot (\mathbb{C}^2\mathbf{a}_{01}), I_6 = \mathbf{a}_{02} \cdot (\mathbb{C}\mathbf{a}_{02}), I_7 = \mathbf{a}_{02} \cdot (\mathbb{C}^2\mathbf{a}_{02}), I_8 = \mathbf{a}_{01} \cdot (\mathbb{C}\mathbf{a}_{02}).$$

Note that I_6, I_7 are the counterparts for \mathbf{a}_{02} of I_4, I_5 , respectively, and I_8 is the coupling term between the two direction vectors. Typical examples are the fibre-reinforced models [1, 45] for arteries, detailed in Chapter 4, and for passive myocardium tissue, in Chapter 7.

2.5 Summary

Material mechanics, and especially tissue mechanics, can be quite complex, and assumptions have to be made when deriving a constitutive equation. It is basically impossible to derive a particular law that could accurately model all aspects of tissue behaviour under any type of loading. Therefore, whenever we develop a constitutive equation to model a tissue, we need to balance the need to accurately reflect the tissue behaviour under the range of loading with the need to have a constitutive equation that is simple and plausible enough to implement in a numerical model and to experimentally measure all the variables in the equation. In the following chapters, we will apply both linear and nonlinear constitutive laws to different biological tissues problems.

Chapter 3

Application to human iris

In this chapter, we use the linear material properties described in Sec. 2.3 to investigate two clinical cases relating to the human iris. The first part has been published in *Clinical & Experimental Ophthalmology* [3] and the second part is to be submitted.

3.1 The optimum size of iridotomy to prevent acute angle close glaucoma in a uveitic eye

Uveitic glaucoma is a condition in which ocular inflammation causes a persistent or recurrent elevation in intraocular pressure (IOP). It is relatively uncommon, however in chronic uveitis its incidence can be as high as 46% [46]. Both secondary open angle and closure mechanisms are implicated in this condition with the pathogenesis considered to be multi-factorial.

The complex relationship between IOP and inflammation makes the management of uveitic glaucoma a challenge. Usually the secondary angle closure glaucoma presents itself acutely and therefore requires immediate anti-glaucoma medical therapy to reduce the IOP. If the mechanism is pupil block, the standard practice is neodymium-doped yttrium aluminium garnet (Nd:YAG) peripheral iridotomy (PI). During episodes of uveitis, multiple mechanisms can increase the resistance to aqueous outflow leading to an elevated IOP.

Acute angle closure glaucoma (AACG), despite having a Nd:YAG PI, have been reported with a high failure rate in a uveitic eyes. It has also been well documented in the literature that the failure is attributed to the inadequate size of PI [47–49]. In cases of uveitis and iris bombe associated AACG, the failure rate is significantly higher, being reported in the region of 40-61% [47, 49].

We present a case of a recurrence of AACG in a uveitic patient where Nd:YAG PI failed to prevent further AACG. We believe a much larger PI is required to prevent recurrent episodes of AACG in a uveitic eye. Therefore, we constructed and applied a mathematical model to determine the optimal size of iridotomy, and ultimately to help understand and modify treatment options.

3.1.1 Description of the clinical case

A 22 year old female presented to the eye casualty with a one-day history of a severely painful left eye, headache, nausea and vomiting. Her vision was counting fingers in the left eye and 6/6[†] in the right. On examination she had corneal oedema, iris bombe, 360° posterior synechiae (PS) and an IOP of 58 mmHg[‡] left, 18 mmHg right. Medical therapy was initiated. She attended three weeks prior to this presentation with a similar episode of AACG, and was treated with Nd:YAG PI, which appeared potent. She has a one-year history of left chronic anterior uveitis resulting in raised IOP, which remained stable following insertion of Ahmed valve and cataract surgery, five months prior to her presentation. And she also developed peripheral anterior synechiae secondary to the chronic uveitis, with resultant damage and scarring to the trabecular meshwork.

Imaging techniques were undertaken to investigate the mechanism of AACG. A high resolution image with ultrasound biomicroscopy (UBM) in Fig. 3.1 showed the marked iris bombe with the peripheral iris in contact with the cornea in all quadrants. Medical therapy was initiated for AACG and a further Nd:YAG laser PI was performed reducing the IOP to 28 mmHg. The PI reduced the degree of iris bombe but did not resolve the occlusion of the drainage angle.

[†]This is a measurement of visual acuity, 6/6 corresponds to an acuity of 1.0.

[‡]Note that this pressure is too high compared to a typical human IOP.

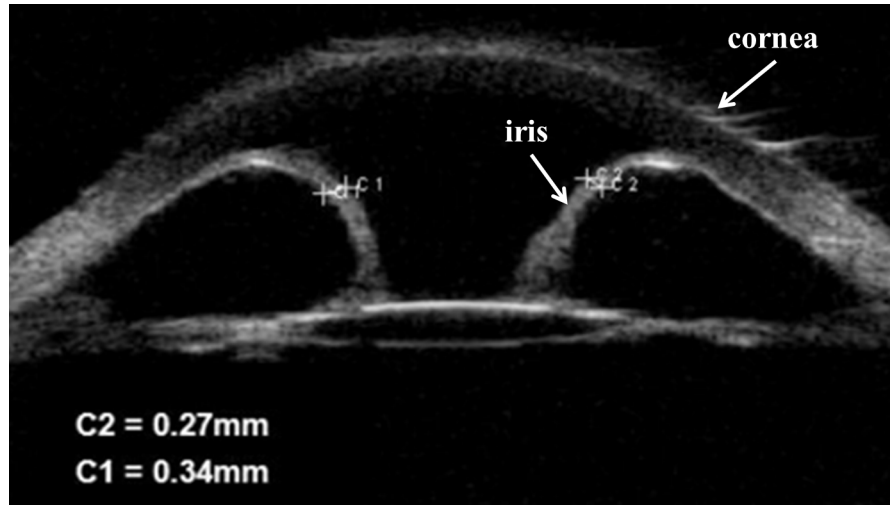


FIGURE 3.1: Left UBM: marked iris bombe with the peripheral iris in contact with the cornea in all quadrants, very thin iris measuring approximately 0.3mm. A drainage tube is in situ at the 1 o'clock position. The iris is pointing at the tip of the tube and occluding it, adopted from [3].

The next day she underwent a left surgical iridectomy. The size of the initial Nd:YAG PI was $195 \times 110 \mu\text{m}^2$. Eight months on, she has remained stable with an IOP of 12 mmHg on no anti-glaucoma medication with a visual acuity of 6/9.

3.1.2 Mathematical modelling of the iris bulging

A mathematical model is constructed to determine the optimal size of PI required in patients with uveitis related iris bombe and angle closure. The model setup is illustrated in Fig. 3.2 where the geometrical data has been scaled from the UBM image in Fig. 3.1. The iris is modelled as a deformable elastic disc with a central circular aperture [4]. To mimic the PS, the inner edge of the iris is assumed to adhere to the lens, preventing flow of aqueous humour between the posterior and anterior chambers. As fluid accumulates in the posterior chamber, it drives a pressure difference (ΔP) across the iris and causes it to deform. Computations of the iris shape are conducted in Abaqus 6.13 (SIMULIA, Providence, RI) assuming the iris to be of uniform initial thickness h with linear elastic moduli listed in Table 3.1.

The PI formed in the iris to reduce the IOP is modelled as a small cylindrical aperture of radius r . For the system to be in equilibrium, the liquid flow through the PI (between the anterior and posterior chambers) must be matched exactly by the production flow Q

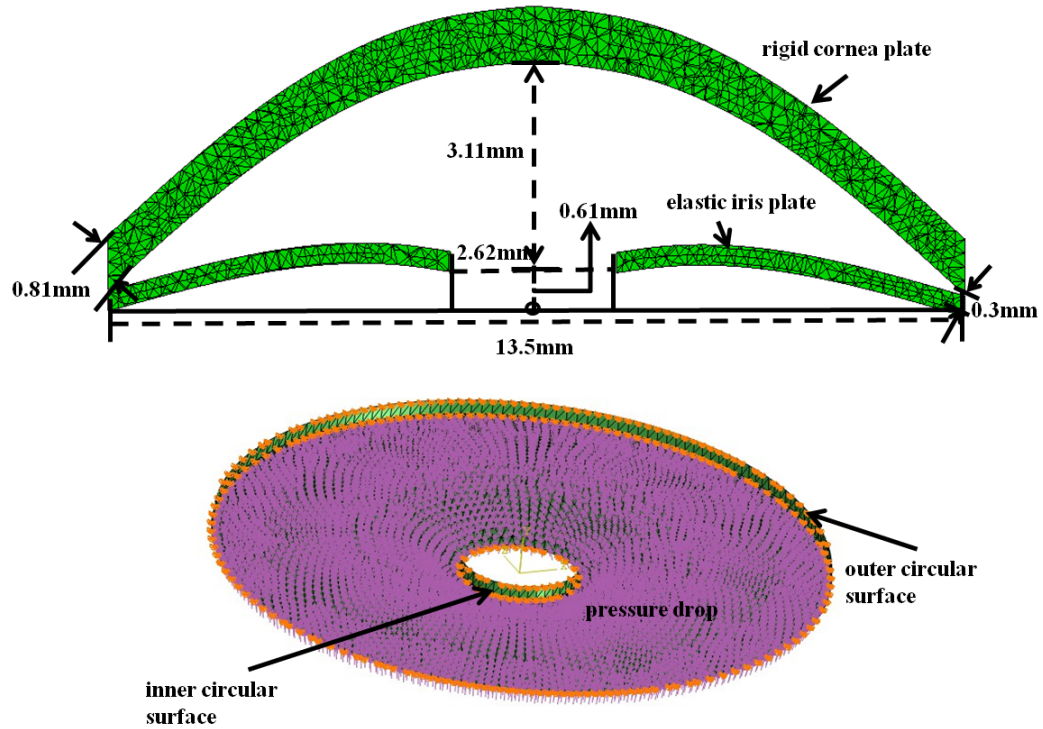


FIGURE 3.2: The geometry of the model has been scaled from the UBM image in Fig. 3.1: the iris is modelled as a deformable elastic disc with a central circular aperture [4]; the cornea and the lens are assumed to be rigid and impermeable.

of the aqueous humour. Assuming the flux of liquid through the PI can be approximated by Poiseuille's law, it emerges that the transiris pressure difference ΔP can be written as

$$\Delta P = \frac{8\zeta h Q}{\pi r^4}, \quad (3.1)$$

where ζ is the viscosity of the aqueous humour, the value of which is also listed in Table 3.1. This formula is used to determine the optimal radius r of the PI.

TABLE 3.1: Parameters used in the mathematical model.

Symbol	Parameter	Value
E	Young's modulus of normal iris	9.6 kPa [50]
ν	Poisson's ratio of iris	0.48
h	thickness of iris	0.3 mm
ζ	viscosity of aqueous humour	1.6 mPa·s [51]
Q	production flux of aqueous humour	2.75 $\mu\text{L}/\text{min}$ [52]

3.1.3 Results

Three typical examples of the iris shape for various ΔP are shown in Fig. 3.3; as ΔP increases the iris bulges axis-symmetrically into the anterior chamber, which is generally consistent with Fig.3.1.

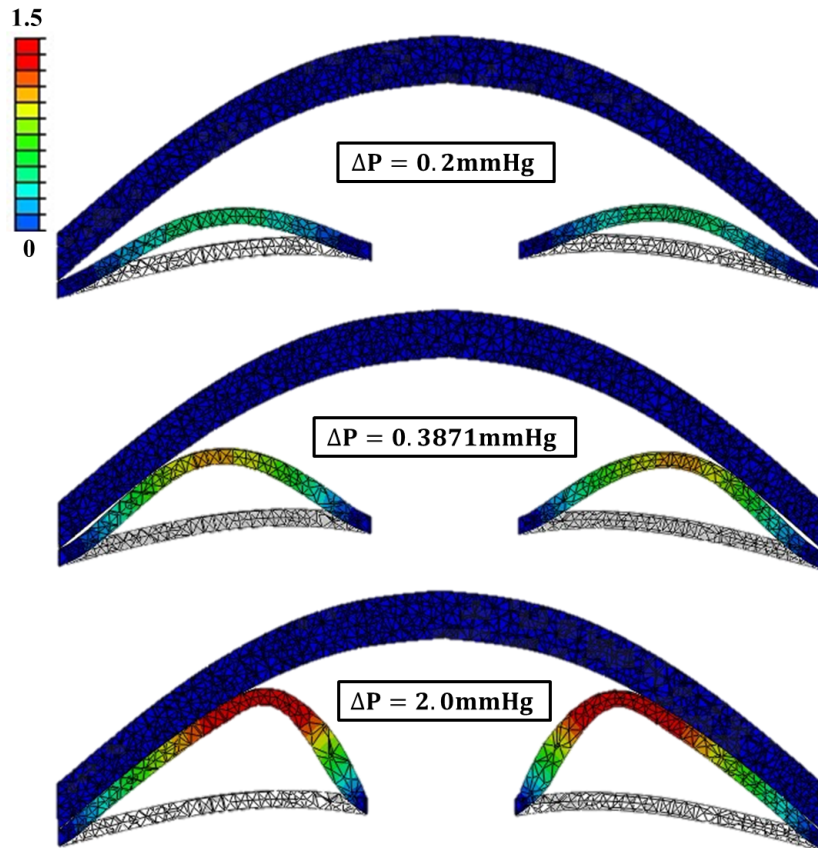


FIGURE 3.3: Computations of the iris shape as a function of this transiris pressure difference were conducted in the Finite Element software ABAQUS 6.13 (SIMULIA, Providence, RI), assuming the iris to be of uniform initial thickness h with elastic moduli listed in Table 3.1. The elastic stiffness of the iris tissue is represented by its Young's modulus, E , and its compressibility by its Poisson ratio, ν . Three snapshots of the iris deformation as a function of the pressure difference ΔP are presented. The black lines indicate the computational mesh used in simulations and the colour shading indicates the displacement of the iris tissue.

The simulations elucidate that the angle between the iris and cornea, denoted as θ , decreases as the pressure difference across the iris increases, and for ΔP above a certain threshold, denoted ΔP_{cr} , the iris makes contact with the cornea leading to acute angle closure, as shown in Fig. 3.4. For the model parameters listed in Table 3.1, this critical pressure difference is calculated to be $\Delta P_{cr} = 0.3871 \text{ mmHg}$ as for the normal iris

elastic properties. This value is slightly larger than the pressure differences assumed in other modelling studies [48, 53]. Decreasing the Young's modulus by a factor of 10 ($E = 0.96$ kPa), the critical pressure difference for this atrophic/floppy iris takes a much smaller value $\Delta P_{cr} = 0.0385$ mmHg.

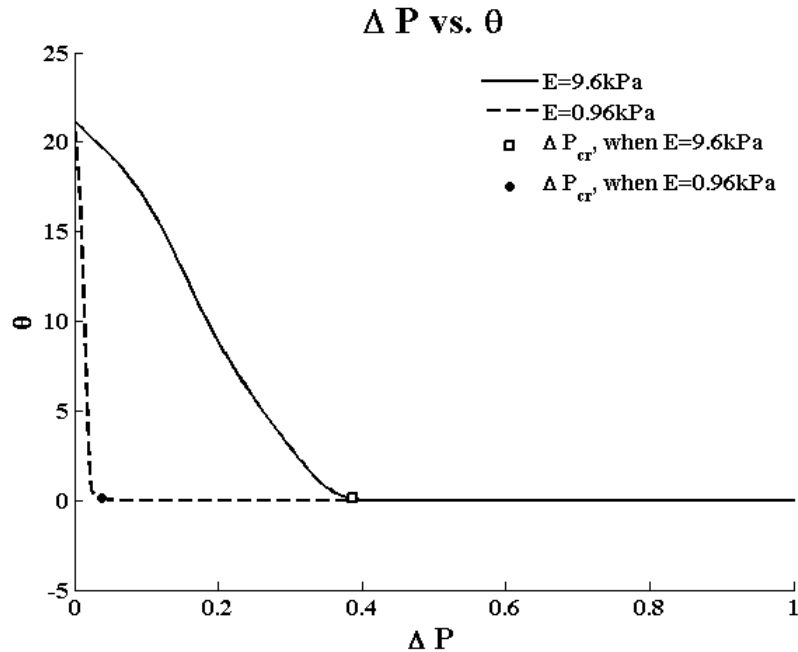


FIGURE 3.4: ΔP vs. θ : predicted acute angle θ between the cornea and the iris as a function of pressure difference ΔP for $E = 9.6$ kPa and $E = 0.96$ kPa

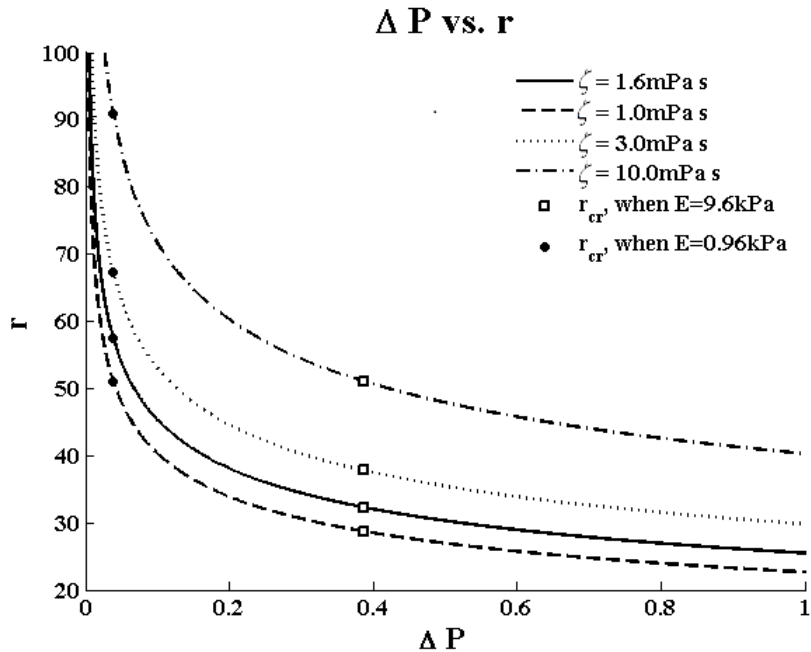


FIGURE 3.5: ΔP vs. r : predicted radius of PI as a function of the pressure drop for $E = 9.6$ kPa and $E = 0.96$ kPa with corresponding prediction for $\zeta = 1.0$ mPa·s, 1.6 mPa·s, 3.0 mPa·s and 10.0 mPa·s.

The predicted curve of ΔP versus PI radius r is plotted as the solid line in Fig. 3.5, where the required pressure difference between the anterior and posterior chambers decreases as the radius of the PI increases. The predicted minimal PI radius can be as large as $32.27 \mu\text{m}$ for a normal iris ($E = 9.6 \text{ kPa}$). In Table 3.2, we demonstrate a ten-fold decrease in the Young's modulus of the iris as predicted in uveitic eyes, resulting in the critical area of the PI increasing by approximately a factor of three, and the predicted minimal PI radius to be larger at $57.47 \mu\text{m}$.

TABLE 3.2: *Minimal PI radius as a function of the viscosity of aqueous humour. The last column A is πr^2 , thus the minimal area of PI, which is more applicable clinically.*

E [kPa]	ζ [mPa·s]	ΔP_{cr} [mmHg]	r [μm]	A [$\times 10^3 \mu\text{m}^2$]
9.6	1.0	0.3871	28.69	2.58
	1.6		32.27	3.27
	1.8		33.24	3.47
	3.0		37.77	4.48
	10.0		51.03	8.18
0.96	1.0	0.0385	51.10	8.20
	1.6		57.47	10.37
	3.0		67.25	14.21
	10.0		90.88	25.94

In addition, the change in the flow pattern in the anterior and posterior chambers due to the PI can also induce an increase in the aqueous viscosity due to non-Newtonian rheology; in Table 3.2, increases in the viscosity of the aqueous humour ζ also results in an increase in the critical area of the PI.

3.1.4 Discussion and conclusion

In our case we believe multiple factors contributed to the development of AACG. The patient had damaged/scarred trabecular meshwork and 270° of peripheral anterior synechiae, implying she had elements of both secondary open and closed angle glaucoma prior to having tube surgery. She went on to develop AACG on two occasions despite having a functioning tube. Both were due to the formation of 360° PS causing pupil block, iris bombe and resulting in occlusion of the Ahmed valve and angle closure in a pseudophakic eye.

There are other factors in this case which we believe contributed to the failure of the Nd:YAG PI. The increased viscosity of the aqueous humour due to the chronic uveitis increases the resistance in the aperture of the PI, and thus reduces the flow through it. Coupled with a floppy, atrophic iris, the pressure required to cause the iris bombe was similar to blowing up a balloon. To blow a balloon initially a high amount of pressure is needed followed by minimal effort.

In our patient, the first episode was treated with a Nd:YAG PI but a second episode occurred despite this. The literature reports high failure rates in uveitis [47, 49], however, the size of the PI is not determined in these studies. Furthermore, there is no report in the literature documenting the average size of PI created by Nd:YAG, possibly because this is variable and often operator dependent. Fleck [48] reported cases of primary AACG despite patent Nd:YAG PI, which have been considered to be due to inadequate size of PI.

To determine the optimal size of PI required to prevent AACG, Fleck [48] constructed a mathematical model which predicted a minimal size of iridotomy of 10-15 μm based on an estimate of the transiris pressure difference, which is difficult to measure *in vivo*. Their mathematical model was based on the assumptions of aqueous viscosity to be equal to the viscosity of water, aqueous flow rate of 2 $\mu\text{L}/\text{min}$ and iris thickness of 50 μm . Based on clinical case and experience, they recommended that the minimal size iridotomy required to prevent AACG should be at least 150-200 μm in diameter, incorporating a large safety margin.

In our patient, the size of the initial Nd:YAG PI was measured to be $195 \times 110 \mu\text{m}^2$, which suggests a PI size greater than Fleck's [48] recommendation of 150-200 μm required in a uveitic eye. In our model, we improved on their approach by predicting the transiris pressure difference using computational solid mechanics. Assuming the viscosity of the aqueous in the eye to be the same as plasma and the iris stiffness to be comparable to a normal iris, the minimum diameter of PI predicted by our model is 64.54 μm . This critical value is significantly less than the YAG PI size used on our patient, explaining its initial success in reducing the patient's IOP.

However, due to the ongoing pathology of the disease the IOP eventually increased again, and a further surgical PI was required to control the IOP. The model demonstrates that this further increase in IOP can be attributed to a decrease in the iris stiffness and/or an increase in the aqueous viscosity. To account for changes in viscosity, the critical diameter for a tenfold decrease in the iris stiffness ($E = 0.96$ kPa) and plasma aqueous viscosity of 1.6 mPa·s is predicted as 114.94 μm . Therefore, in order to prevent AACG in patients with uveitis related iris bombe, we recommend a diameter for the PI of at least $300\text{-}350$ μm^\dagger . For a PI of the size 300 μm , this would be equivalent to 11 Nd:YAG PIs of similar size to that conducted on our patient (195×110 μm^2). For a diameter of 350 μm , 21 Nd:YAG PIs would be needed.[‡]

The mathematical model constructed is deliberately simple and has limitations, with several of the model parameters, excluding the thickness of the iris, based on estimated values from the literature [50–52]. Parameters such as the aqueous viscosity and the iris stiffness are dependent on the pathology of the disease and these values can only be estimated.

This case highlights the therapeutic challenge of managing a patient with uveitic glaucoma due to the complex relationship between IOP and inflammation. The mathematical model allows us to explore the possible mechanism and variables in a uveitic eye. The model shows increasing aqueous viscosity and the atrophic/floppy properties of the iris, as postulated in a uveitic eye, requires a larger diameter of PI than previously recommended by Fleck et al. [48] of $150\text{-}200$ μm . Based on our model, we advise a minimum diameter of PI to be $300\text{-}350$ μm to prevent AACG in a uveitic eye, and we suggest that a surgical approach rather than Nd:YAG PI may be more beneficial for these complex patients.

[†]This range is calculated from a safety factor of three.

[‡]Suppose that the area of Nd: YAG PI is A_{Nd} and the area of a required single PI is A , then the model predicts that the number of Nd:YAG PI can be approximated by $n = (\frac{A}{A_{Nd}})^2$ (see the relationship of ΔP and area $A = \pi r^2$ in Eq. 3.1). Hence, based on our recommendation of a diameter of 300 μm ($A = 7.0684 \times 10^4$ μm^2) and the Nd:YAG PI area of the first PI of 195×110 μm^2 ($A_{Nd} = 2.1450 \times 10^4$ μm^2), then the number of YAG PI required is 10.86. So to obtain the desired flow rate with our predicted PI size, we need comparatively 11 Nd:YAG PIs. In the same manner, for a diameter of 350 μm that would equate to 21 Nd:YAG PIs.

3.2 Modelling of iris buckling within floppy iris syndrome

In recent years, conventional penetrating keratoplasty (PTK) has given way to new posterior lamellar keratoplasty techniques for selective replacement of the diseased posterior layers of the cornea in patients with endothelial insufficiency, such as Descemet's stripping endothelial keratoplasty (DSEK) [5, 54]. DSEK has established itself as a preferred corneal transplantation technique worldwide, because patients achieve satisfactory visual acuity more quickly than after PTK, and have minimal change in corneal surface topography or refraction [54, 55].

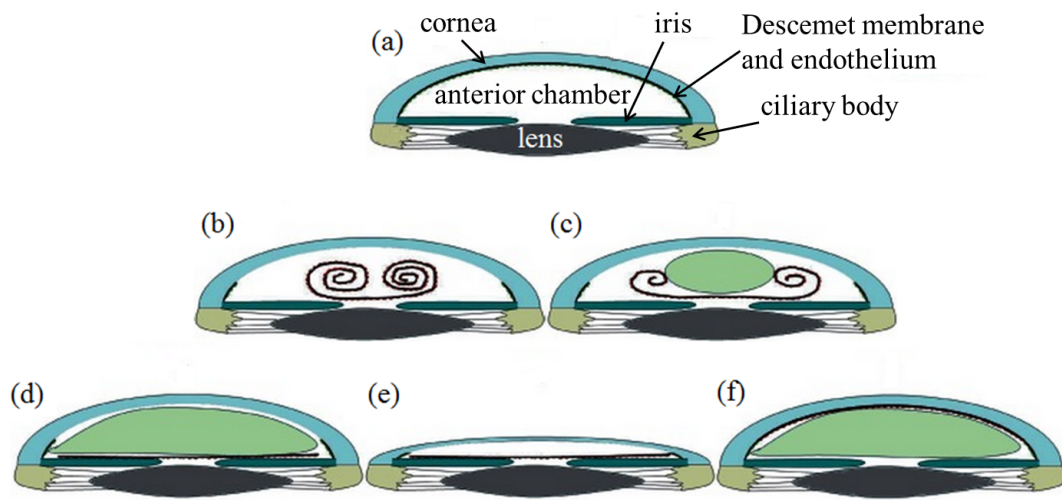


FIGURE 3.6: The procedure of DSEK showing the anterior chamber of the eye with diseased endothelium on Descemet membrane, adapted from [5].

During a DSEK procedure, two small incisions are made to allow microsurgical instruments to strip off the diseased endothelium from the central portion of the patient's cornea (Fig. 3.6(a)). After the donor replacement corneal tissue layer is prepared, it is gently folded and placed within the fluid-filled anterior chamber of the eye, beneath the patient's cornea (Fig. 3.6(b)). Injected sterile air creates a tamponading air bubble (Fig. 3.6(c)), which is used to slowly unroll the donor tissue until it lies against the iris (Fig. 3.6(d)). Then the air bubble is removed causing the anterior chamber to collapse such that the graft cannot roll up again (Fig. 3.6(e)). Finally a second air bubble is introduced and inflated to carefully press the graft against the posterior surface of the host cornea and hold it in the exact location where the abnormal tissue was removed to

ensure sutureless apposition and graft attachment (Fig. 3.6(f)). The smaller incisions, the need for fewer or no sutures, and the shorter procedure and recovery time make the DSEK procedure safer and produce better visual results than conventional full thickness PTK [5, 56].

However, despite the many advantages of the DSEK procedure compared to the full thickness corneal transplantation, it is not completely free of post operative complications, which include posterior graft dislocation, graft failure and iatrogenic pupil block glaucoma [54, 57]. Recently, the incidence of floppy iris syndrome during the DSEK procedure has acquired a lot of clinical attention. This syndrome is characterised by uncontrollable billowing, pupillary miosis and prolapse of iris into the corneal incisions. In addition, the iris can roll up and block the peripheral angle, which in turn rises the intraocular pressure (IOP) sharply due to mechanical obstruction of fluid through the drainage structures present in the angle of the anterior chamber of the eye (trabecular meshwork). Attempts to relieve this iridocorneal contact by removal of the second air bubble are typically unsuccessful. Injection of balanced salt solution into the angle can create a wave of fluid pushing the iris back, but the iris quickly returns to its highly deformed configuration [4]. In order to develop better management or prevention of this clinical scenario, we need to understand the mechanical behaviour of the iris during the DSEK procedure.

We hypothesize that the reason for the angle closure following the surgery is due to the iris buckling under the increased IOP induced by the presence of the second air bubble. To test this hypothesis, we have developed a three-dimensional elastic model of the iris, which can account for the anisotropic material properties, and predict deformation of the iris under pressure. This model is solved using finite element method and used to investigate the critical IOP required to cause the iris buckling (roll-up). Post-buckling deformation of the iris may then block the superior angle.

The majority of eye modelling studies have focused on ocular fluid mechanics [48, 58, 59], or simplified fluid-structure interaction [60, 61]; some of these studies have considered the iris and its interaction with aqueous humour [53, 58, 59]. However, to the best of our knowledge, three-dimensional modelling of iris buckling under pressure loading

accounting for the anisotropy of the iris tissue has not been reported. We believe that a detailed mathematical modelling of mechanical behaviour of the iris plays a vital role on the effective management for clinical complications such as these associated with the floppy iris syndrome, and our model of iris buckling is the first step towards understanding complications during the DSEK.

3.2.1 Iris Buckling Model

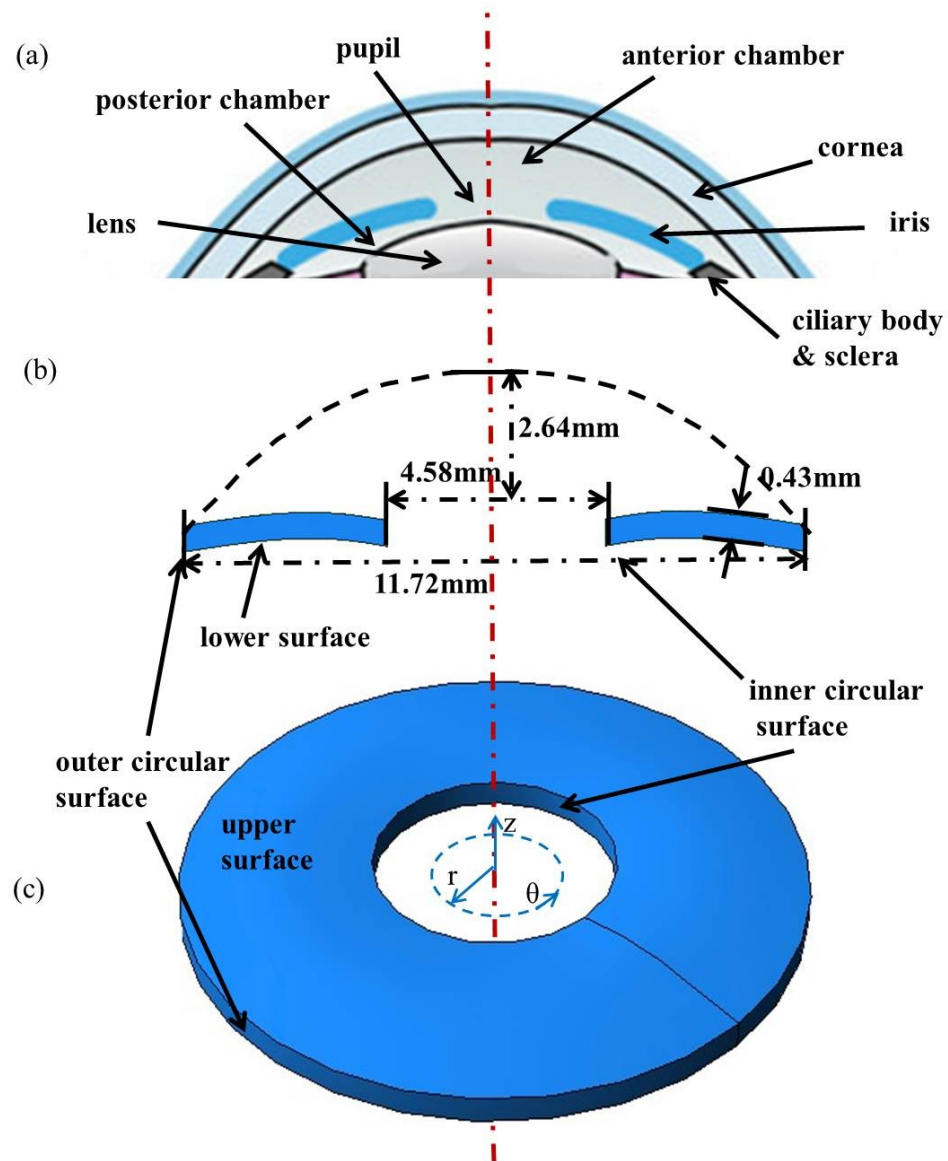


FIGURE 3.7: (a) The side view of a general eye structure; (b) the iris structure with the geometric information, and (c) the three dimensional model of the iris, its relation with (b) is indicated.

3.2.2 Model set up

The iris is again modelled as a curved annular disc with a central aperture (mimicking the pupil). The external edge of the tissue is fixed to the ciliary body and sclera, as shown in Fig. 3.7, which is the same as described in Section 3.1.2. However, unlike our patient-specific geometrical data from the UBM image in the first clinical case, we use averaged human data available from the literature [62–65], and assume that the iris has a uniform thickness of 0.43 mm with a convexity of 0.27 mm, the anterior chamber width and depth are 11.72 mm and 2.64 mm, respectively, and the pupil length is 4.58 mm[63]. We define this configuration as the reference configuration described by a cylindrical coordinate system (r, θ, z) . The IOP is denoted as P and we assume that the iris behaves as a linear elastic material occupying volume V with boundary Γ . We also assume that all free surfaces of the iris are subject to a constant IOP of magnitude P , while the additional pressure gradient due to the slow viscous flow of aqueous humour is negligible.

3.2.3 Linear buckling analysis

In the absence of body force, the total potential energy is

$$\Pi = \frac{1}{2} \int_V \boldsymbol{\epsilon}^T \mathbf{C} \boldsymbol{\epsilon} dv - \int_{\Gamma} \mathbf{u}^T P \mathbf{n} ds. \quad (3.2)$$

where \mathbf{C} is the elasticity tensor and \mathbf{n} is the unit normal vector at the boundary Γ .

Using the principle of virtual displacement, and evaluating $\delta\Pi = 0$ with respect to the displacements, we obtain the equilibrium equations. With the finite element discretization, i.e. using the nodal displacement vector \mathbf{U} to represent \mathbf{u} and $\boldsymbol{\epsilon}$, we can express the equilibrium equations in the matrix form:

$$\mathbf{K}\mathbf{U} = \mathbf{R} \quad (3.3)$$

where \mathbf{K} is the stiffness matrix, and \mathbf{R} is the discretised load vector [66].

We use buckling analysis to assess the stability characteristics of the iris structure [67]. We find the critical pressure load for which the stiffness matrix \mathbf{K} becomes singular in the following eigenvalue problem. An incremental loading pattern, $P = P^{base} + \lambda_k P^{inc}$, is defined, where λ_k is the scaling factor which becomes the eigenvalue when the critical conditions are reached:

$$(\mathbf{K}_0^{cr} + \lambda_k \mathbf{K}_\Delta^{cr}) \mathbf{U}_k^{cr} = \mathbf{0} \quad (3.4)$$

where \mathbf{K}_0^{cr} is the stiffness matrix corresponding to the base state, \mathbf{K}_Δ^{cr} is due to the incremental loading, and \mathbf{U}_k^{cr} are the eigenvectors of the k th buckling mode [68].

3.2.4 Nonlinear static analysis

A general analysis in which the effects of nonlinearity is considered in this model. It is carried out as a series of linear analyses and the material properties are assumed to be constant in the whole analysis. The maximum time increment allowed is 0.1, if convergence is not possible it will re-solve with a reduced time step. In ABAQUS this procedure is repeated until convergence is reached in its minimum increment (1×10^{-5} in our case). To trigger instability we apply a small amplitude sinusoidal perturbation of period 2π along the circular ring.

3.2.5 Elastic properties

We assume that the iris tissue is nearly incompressible, so that the Poisson's ratio is nearing 0.5. In the simulations reported below we choose the Poisson's ratio to be 0.497 [50]. We consider both isotropic and orthotropic elastic responses of the iris following from Sec. 2.3.

For the isotropic case, we choose the elastic modulus E in the range of 2.00 to 10.00 kPa, based on measurements of cadaveric porcine and bovine iris, where moduli of 2.97 kPa and 9.60 kPa are reported, respectively [50, 69]. For the orthotropic case, we choose the azimuthal elastic modulus to be 2.97 kPa, and the radial elastic modulus to be 4.00 kPa, based on the tests of porcine iris tissue [69].

The typical IOP in humans is around 10-21 mmHg in normal subjects [4, 70]. However, it can exceed 35 mmHg in pathological situations [4]. To mimic the increase in IOP during graft surgery caused by the injection of an intracameral air bubble into the aqueous fluid, we apply a pressure loading incrementally from $P^{base} = 10$ mmHg onwards. This loading is applied simultaneously to the upper, lower and inner circular surfaces of the iris as indicated in Fig. 3.7(c). The displacement of the outer circular surface is fully constrained to mimic the anchoring by the ciliary muscles. Surface tension and shear forces due to the air/aqueous flow are considered to be negligible as the flow is very slow.

Following the grid independence test, we construct a finite element mesh with 17,000 nodes and 12,240 hexhedral elements. The finite element model is implemented using the commercial package ABAQUS 6.13 (SIMULIA, Providence, RI).

3.2.6 Results

3.2.6.1 Buckling analysis for isotropic iris tissue

TABLE 3.3: *Critical pressures (mmHg) in the first five modes under different elastic moduli (kPa) in the isotropic case. The buckling modes for $E = 4.00$ kPa are shown in Fig. 3.8.*

E [kPa]	P [mmHg]				
	$n = 0$	$n = 1$	$n = 2$	$n = 3$	$n = 4$
2.00	14.09	16.14	20.44	25.28	28.67
2.97	17.63	21.28	28.88	37.51	46.85
4.00	22.24	27.77	39.17	52.32	66.88
6.00	33.23	42.62	61.80	84.43	110.20
8.00	46.27	59.55	86.62	119.22	156.99
10.00	60.83	77.88	112.78	155.58	205.75

We choose $P^{base} = P^{inc} = 10$ mmHg and increase the pressure (i.e. increase the scale factor λ_k) until the critical conditions are reached. The critical buckling load when the iris first buckles is found to be 22.24 mmHg at $E = 4.00$ kPa, as listed in Fig. 3.8. With further increases in IOP, higher buckling modes also occur. We label each buckling mode according to the number of local maxima across the structure, for example, mode $n=2$

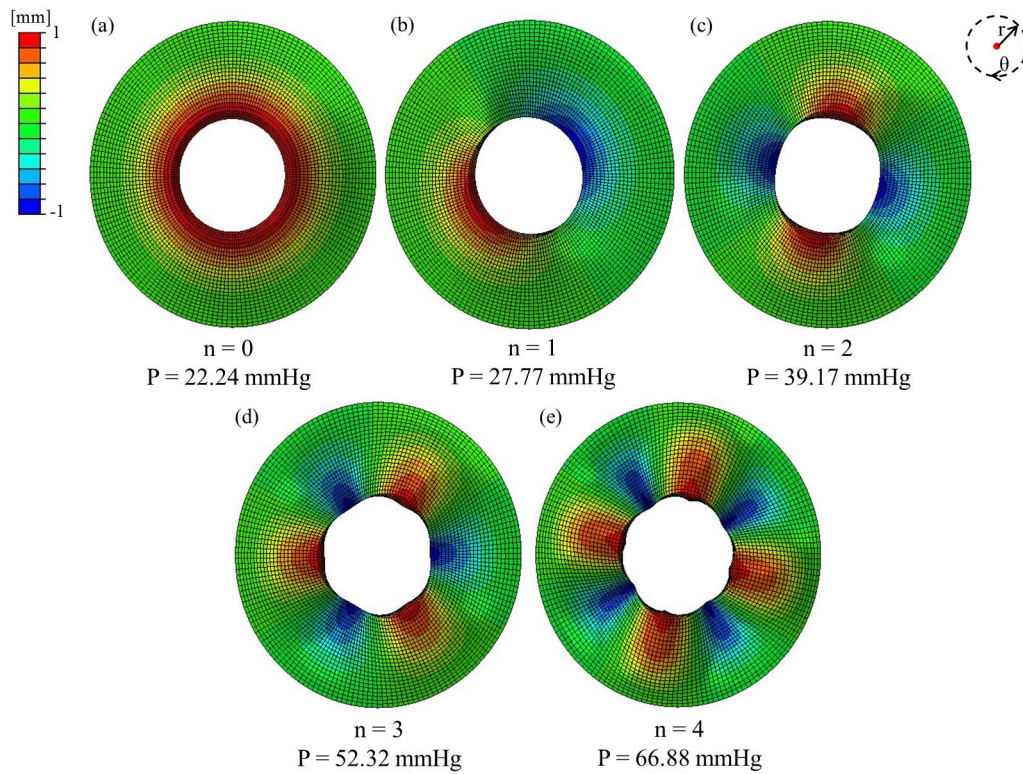


FIGURE 3.8: The first five buckling modes in the r - θ plane view for the isotropic iris model, in which $E = 4.00$ kPa. The colour indicates the longitudinal displacement.

has 2 maxima as shown in Fig. 3.8.(c) The critical buckling pressures for each mode for different elastic moduli are listed in Table 3.3.

The critical IOP required for each buckling mode is significantly lowered as the material becomes less stiff (floppy), as expected from other buckling studies in elastic tissue [71, 72]. In addition, the differences in the critical pressure between individual modes become greater with increased material stiffness. In other words, the higher modes are more likely to occur for a floppy material. However, all buckling modes have some symmetries for the isotropic material. The $n = 0$ mode is axis-symmetric while for $n > 0$, mode n has n symmetries. As in the analytical solution [73], the annular isotropic plate always buckles into the axisymmetric form regardless of the hole size.

3.2.6.2 Buckling analysis for orthotropic iris tissue

Here the iris is instead modelled as an orthotropic material and we repeat the stability analysis as in Sec. 3.2.6.1. Again, we label the modes in the same manner as before,

and the critical buckling pressures for the first five modes are listed in Table 3.4, with the corresponding onsets of unstable shapes shown in Fig. 3.9. However, in this case we find distinct modes with the same number of symmetries for $n \geq 2$, which we label with the suffix ‘a’, ‘b’ *etc.*

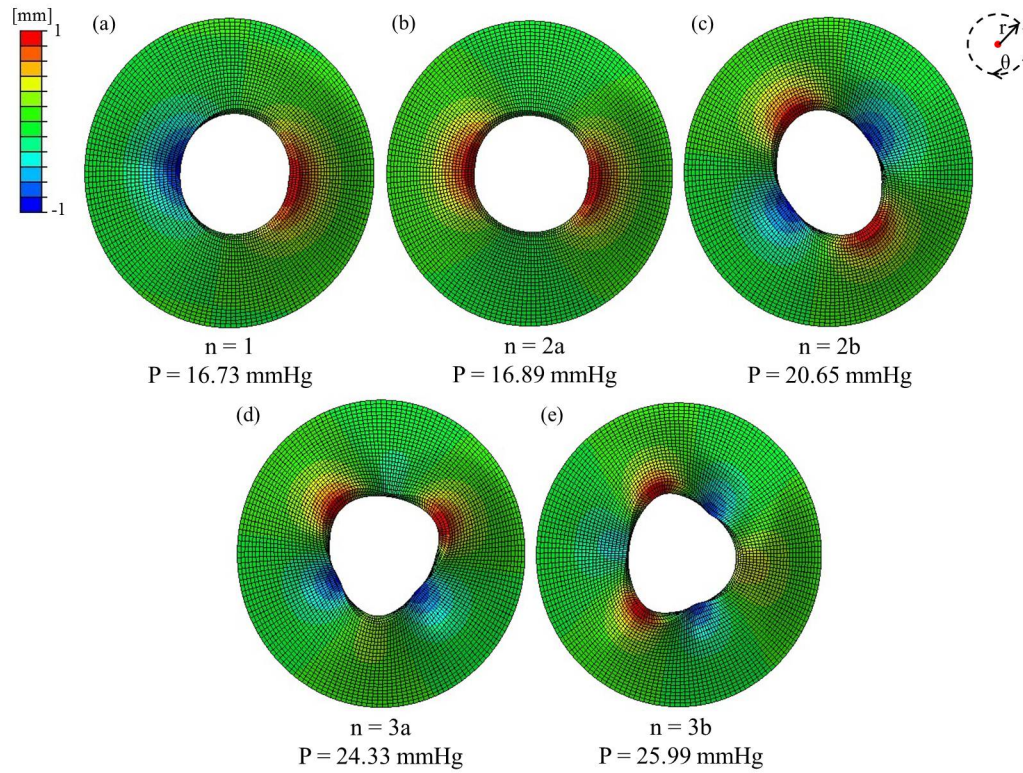


FIGURE 3.9: The first five buckling modes in the r - θ plane view for the orthotropic material model.

TABLE 3.4: Critical pressures (mmHg) in the first five modes in the orthotropic case.

E_r [kPa]	E_θ [kPa]	E_z [kPa]	P [mmHg]				
			$n = 1$	$n = 2a$	$n = 2b$	$n = 3a$	$n = 3b$
4.00	2.97	4.00	16.73	16.89	20.65	24.33	25.99

In this case the mode $n = 1$ is the most unstable at a critical pressure of 16.73 mmHg for the choice of the elastic moduli. As expected, the critical buckling pressures are lower than for the corresponding isotropic material with $E = 4$ kPa (listed in Table 3.4).

These results suggest the importance of modelling the iris as an orthotropic material. For example, with this model, the post-buckling deformation may cause the angle closure in an asymmetric manner as was observed during the surgery. The subsequent increase

in pressure due to the fluid blockage could eventually lead to complete angle closure and pupil block glaucoma.

3.2.6.3 Post-buckling analysis and angle closure

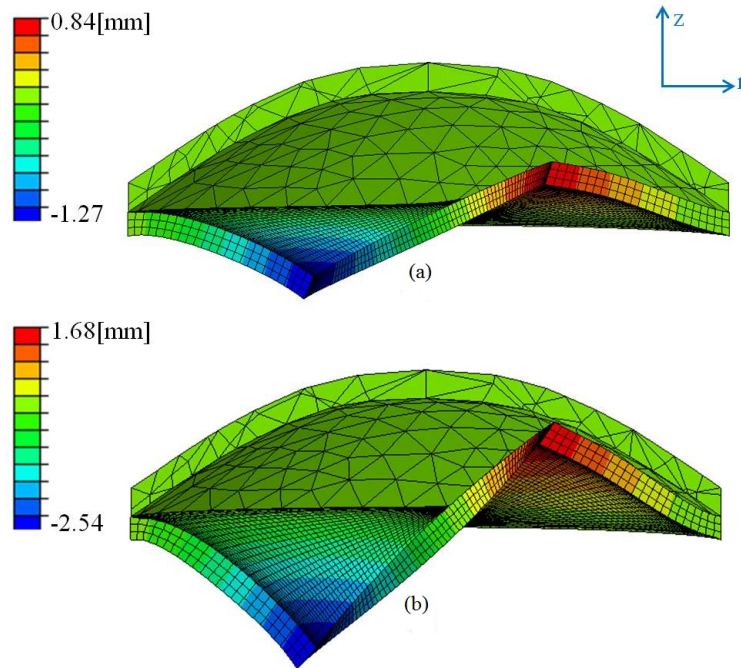


FIGURE 3.10: The configurations of mode $n = 1$ with cornea shown in the r - z cut-plane view where (a) $\eta = 1.0$ and (b) $\eta = 0.5$. We note that when η is below 0.5, the iris makes contact with the cornea.

Furthermore, we investigate the fully nonlinear deformation of the orthotropic iris as the loading continues beyond the critical buckling pressure. In particular, we consider the case where the IOP is close to the critical value for the first buckling mode ($P = 16.73$ mmHg) and introduce a circumferentially sine-shaped pressure with magnitude of 0.001 mmHg. The corresponding static iris profile is shown in Fig. 3.10(a). The predicted iris deformation agrees very well with the eigenfunction of the $n = 1$ buckling mode shown in Fig. 3.9.

3.2.6.4 Implication for ‘floppy iris syndrome’

We note that the elastic properties of the iris can be very different in abnormal situations: for example, in the case of floppy iris syndrome the elastic moduli decrease significantly [4]. To further analyse the floppy iris behaviour, we changed the elastic moduli in the orthotropic iris model using a proportion factor η , so that the elastic moduli become $\eta E_i, i = r, \theta, z$. The relationship between the first critical pressure and η is shown in Fig. 3.11, highlighting how a uniform reduction in stiffness can reduce the critical pressure in the range of the normal IOP. This may explain why the complications associated with the floppy iris syndrome were observed in the DSEK procedure [4].

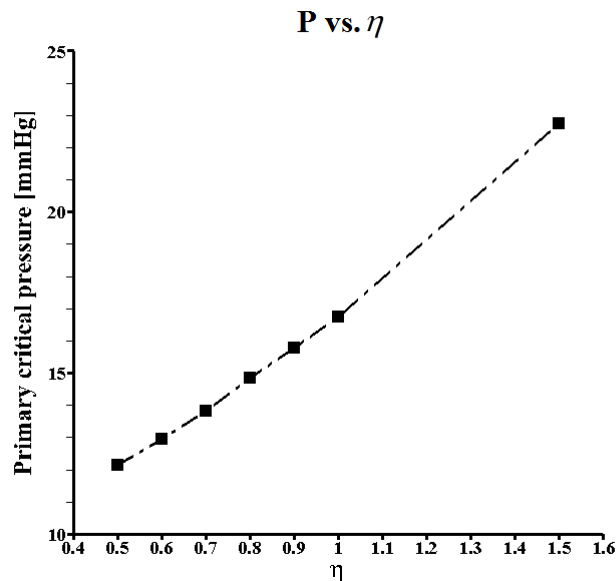


FIGURE 3.11: The critical IOP for the first buckling mode as a function of the reduction in η .

A plot of the minimum angle between iris and cornea (denoted α) as a function of the IOP is shown in Fig. 3.12. As the structural material becomes less stiff, i.e. η is smaller, the minimum angle tends to zero, indicating angle closure and obstruction of the fluid drainage into the Schlemm’s canal, as is shown in Fig. 3.10(b) when $\eta = 0.5$. This in turn can lead to acute angle glaucoma.

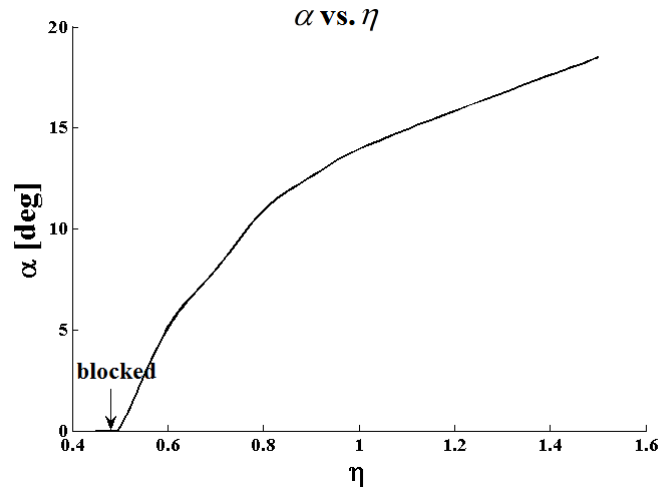


FIGURE 3.12: The minimum angle between iris and cornea as a function of the reduction in η .

3.2.7 Discussion and conclusion

This study aims to understand the mechanism of acute rise in the IOP in the case of corneal transplant surgery using a finite element mechanical model of iris. The model is used to identify the key parameters in the iris buckling, the air bubble induced pressure, and the material properties of iris. These are helpful in the understanding and treatment of complications. As a result, we have modified our clinical approach to control the initial pressure rise in surgery which may cause the iris buckling.

It is worth mentioning that although our iris model is built on a symmetric ring structure, when the critical pressure is reached, it buckles into many asymmetric modes. This suggests that such analyses must be done with three-dimensional models. Importantly, the critical pressure is sensitive to the material properties, especially during surgery when inflammation may occur. In this sense, it is crucial to obtain measurements of the human iris tissues under both physiological and pathological conditions. Since the mechanical properties of human iris tissue are not available, we have to estimate our model parameters based on measurements of animal (canine and porcine) iris, hence we cannot validate our model prediction directly with the clinical case without the knowledge of the iris property of the subject in question. Therefore, although our model predictions can explain the mechanism in general, these are not patient-specific.

To conclude, we have developed a finite element orthotropic iris mechanical model to understand the mechanism of acute rise in the IOP. Using a buckling analysis, we are able to predict the critical pressures under which the iris may lose its stability. This situation is exacerbated by the floppiness of the iris since the critical pressure is much lower when the iris is less stiff. We believe the buckling of the iris is the key reason leading to the blockage the superior angle, and subsequent complications.

Chapter 4

Investigation of the optimal collagen fibre orientation in human iliac arteries

The distribution of collagen fibres plays a significant role in the mechanical behaviour of arterial walls. Experimental data show that in most arterial wall layers there are two (or more) in-plane symmetrically disposed families of fibres. However, a recent investigation revealed that some arterial wall layers have only one preferred fibre direction, notably in the medial layer of human common iliac arteries (CIAs). This paper aims to provide a possible explanation for this intriguing phenomenon. The results have been published in *Journal of the Mechanical Behaviour of Biomedical Materials* [74].

4.1 Introduction

The collagen fibres within arterial walls play a significant role in the macroscopic behaviour of the walls [1, 75]. Human CIAs are of particular clinical interest, as atherosclerosis-prone vessels, since they frequently undergo endovascular treatment. Iliac arteries are relatively easy to access for vascular diagnostic procedures [7].

Most of the aforementioned studies focused on the mechanical properties of coronary arteries [76]. In this study we concentrate on the human iliac artery. This is because an exception to the fibre structure has been found in the medial layer of human CIAs in the recent work by Schriefl et al. [6]. Using polarised light microscopy on stained arterial tissues, these researchers measured the layer-specific collagen fibre density distribution in human thoracic and abdominal aortas, and in CIAs. They found that unlike in most of the investigated arterial layers where there are two or more distinct families of the collagen fibres, fibres are found to be mostly parallel to the circumferential direction in the media of the human CIAs, as is shown in Fig. 4.1. Various fibre dispersions in different layers of arteries were also reported.

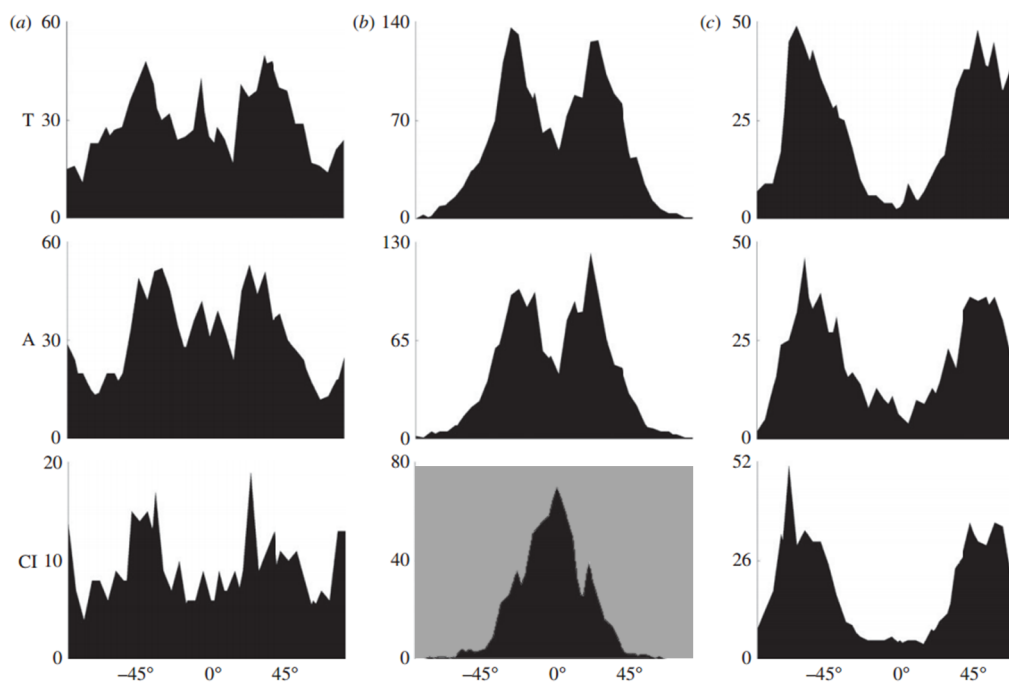


FIGURE 4.1: The density of the measured angles of fibre families for the descending thoracic aorta T, the abdominal aorta A and the common iliac arteries CI. The three columns are for (a) intima, (b) media and (c) adventitia. The degree of the fibre angle is measured with respect of the circumferential direction of the arteries. The grey box highlights the unusual distribution in the medial layer of CIAs, where the preferred direction of the fibre families is along the circumferential direction. Adapted from [6] with permission.

The work [6] raises interesting questions. In particular, what determines the optimal fibre orientation? Can we explain the fibre distribution in the media of the CIA from the mechanics standpoint?

In this chapter, we attempt to answer these questions using a combined analytical and computational approach.

We treat the iliac artery as a two-layer thick-walled model, including only the media and adventitia. We use the κ model [75] in which the effect of the fibre dispersion is taken into account. Both the axial pre-stretch and the circumferential residual stress are considered. To separate the effects of the circumferential and axial residual stresses from the geometric influences, we also investigate a straight tube model with the corresponding material properties as well as the residual stresses in the circumferential direction. Inflation and extension experiments are simulated numerically with 13.33 kPa blood pressure loading. For simplicity, we confine our study to static loading only. Finally, three different hypotheses are used to determine the ‘optimal fibre angle’ in the iliac artery model. Results from all three hypotheses support the experimental observation that there is probably a single fibre family in the media of human iliac arteries.

4.2 Methodology

4.2.1 Geometry of a 3D aorto-iliac bifurcation

Based on human data documented in the literature [7–10], an ideal but typical bifurcation geometry of an iliac artery is built, as shown in Fig. 4.2. The bifurcation is constructed such that the cross section at the end of the aorta is gradually changed from a sequence of circles to ellipses, see in Fig. 4.3. This is then smoothly connected to the two iliac arteries via cubic spline positional polylines using Matlab (R2012b). By this special treatment, the quality of the hexahedral elements can be guaranteed. In addition, the label and the corresponding position of every single element are fully captured, which makes it convenient to assign the fibre orientations on each finite element later on.

We model the iliac bifurcation as a two-layer thick-walled structure, and the thickness ratio between the medial and adventitial layers is taken to be 4:3 [6]. A total of seven hexahedral elements (four in the media and three in the adventitia) through the wall

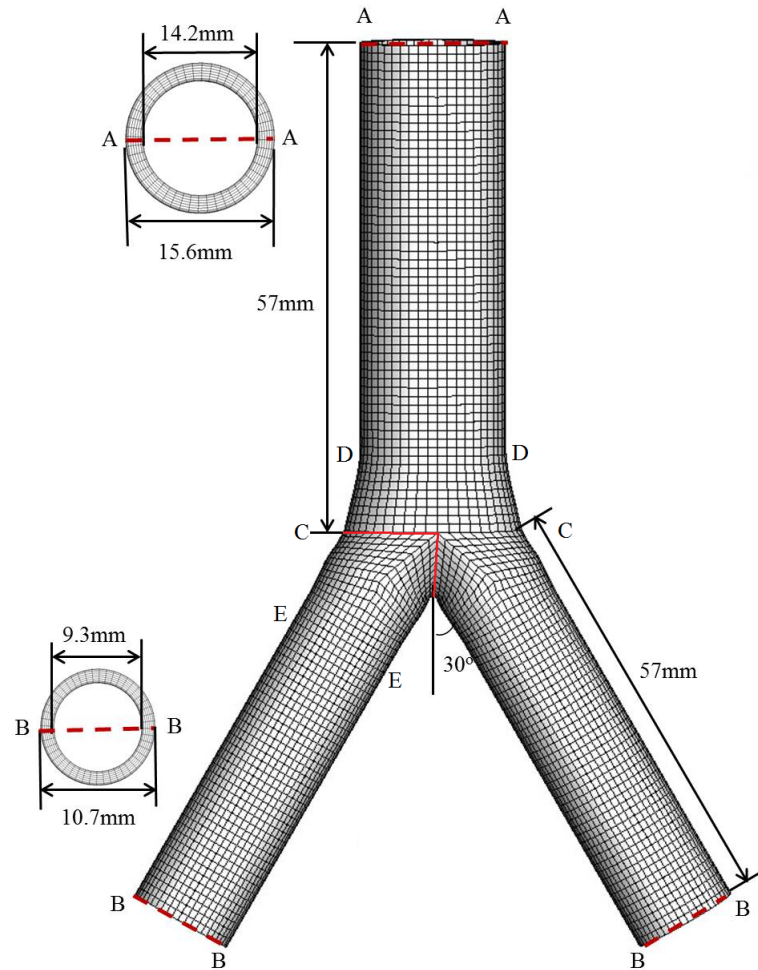


FIGURE 4.2: Three-dimensional geometry of the aorto-iliac bifurcation model. The geometric information is taken from the literature. The inner and outer diameters are chosen to be 14.2 mm and 15.6 mm, respectively, for the abdominal aorta, and 9.3 mm and 10.7 mm, respectively, for the CIAs, following [7] and [8]. The length of the aorta and each iliac artery is taken to be 57 mm [9, 10]. The two iliac branches are assumed to deviate from the centreline of the aorta symmetrically at 30° [11, 12]. The labels ‘C’ to ‘E’ correspond to Fig. 4.3.

thickness is constructed. Although the geometry is symmetric and the modelling could be achieved by considering a quarter of the whole section, we choose to use the whole geometry so that the modelling can be easily extended to include the fluid-structure interaction in future studies, for which the flow field can be asymmetric. We also note that the three-dimensional simulation of the whole section is not costly in computational time.

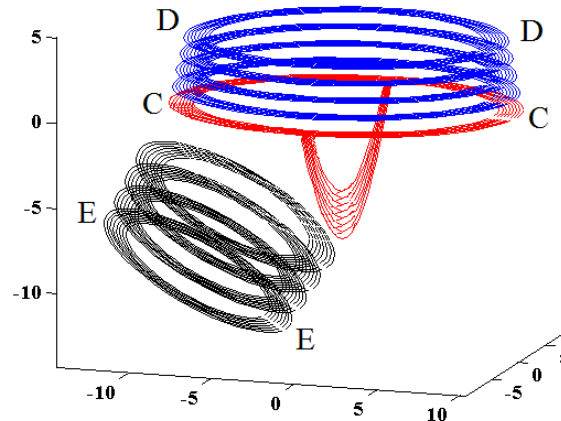


FIGURE 4.3: Special scheme to connect the aorta and the two iliac branches. We use sequences of ellipses approaching from the aorta in blue ('D' to 'C') and approaching from one of the iliac branch in black ('E' to 'C') to mimic the bifurcation neck). To connect them, we use two sequences of perpendicular semi-ellipses at 'C' (highlighted in red in Fig. 4.2) such that the following stacks progressively become flat.

4.2.2 Constitutive κ model

Artery walls are usually composed of three distinct layers, the intima, the media and the adventitia, and it is widely accepted that variations exist in both the structural composition and the material properties of arterial walls in different regions of the arterial tree, even from the same individual [1, 13, 77]. Collagen fibres are key ingredients in the structure of arterial walls. In most regions, load bearing layers such as the media and adventitia are shown to have two (or more) in-plane symmetrically disposed families of fibres.

Therefore, continuum constitutive models of arterial layers integrate information about the tissue morphology and allow investigation of the interrelation between structure and function in response to mechanical loading. Carefully constructed constitutive laws based on experiments are of critical importance for analysing the physiological and pathological load-carrying mechanisms in soft tissues [75].

A number of experimental studies, based on polarised light microscopy of stained arterial tissue, have shed light into the detailed structural organisation of the complex three-dimensional elastin, collagen and smooth muscle arrangement within the arterial wall [6,

78–80]. These studies show not only that artery tissues are highly anisotropic, but also provide an explanation for the exponential response of the tissues. The gradual recruitment of the collagen fibres, which are considered to be crimped in their natural configuration, is responsible for the exponentially increased stiffness of the tissue when stretched [81, 82].

With this understanding, more advanced constitutive laws have been developed to make use of the microscopic information of arterial wall structures [1, 75, 83, 84]. The anisotropic elastic energy functions proposed by [1], [85] and [86] represent one category of such structure-based approaches. For example, the constitutive model by [1] is used to represent the ground matrix and the distinct fibre families in the arterial wall. The model assumes that the fibres are symmetrically disposed relative to the axial direction and have no component in the radial direction.

This model assumes that the strain-energy function Ψ is the sum of an isotropic potential Ψ_{iso} associated with the ground matrix and an anisotropic potential Ψ_{aniso} associated with the embedded families of perfectly aligned collagen fibres [87]. It is assumed that the artery material is incompressible, so we have $J = 1$. We have the two fibre families aligned in the directions of the unit vectors \mathbf{a}_{01} and \mathbf{a}_{02} in the reference configuration. These are symmetric and lie in the tangent plane (no radial component). Let λ_r , λ_θ and λ_z be the principal stretches in the cylindrical system. Then, the strain-energy function[†] associated with the right Cauchy–Green tensor \mathbb{C} is

$$\begin{aligned} \Psi &= \Psi_{\text{iso}}(\mathbb{C}) + \Psi_{\text{aniso}}(\mathbb{C}, \mathbf{a}_{01}, \mathbf{a}_{02}) \\ &= \frac{c}{2}(I_1 - 3) + \frac{k_1}{2k_2} \sum_{i=4,6} [\exp(k_2(I_i - 1)^2) - 1], \end{aligned} \quad (4.1)$$

with the I_4 term only included if $I_4 > 1$ and same for the I_6 term. This ensures that the load-bearing collagen fibres embedded in the arterial wall only bear loads when stretched, not compressed. For the walls of most large arteries, these two fibre families are located symmetrically about the axial direction, so that, for the deformation considered here,

[†]Note, this strain-energy function is designed as an incompressible formulation. A modified version of Eq. (4.1) with an isochoric/volumetric split is used in the finite element implementation.

$I_4 = I_6 = \lambda_\theta^2 \cos^2 \beta + \lambda_z^2 \sin^2 \beta$, where β denotes the angle between \mathbf{a}_{01} (or \mathbf{a}_{02}) and the circumferential direction of the artery.

However, the above constitutive model does not include the fibre dispersion observed in experiments, and to take account of fibre dispersions, two extended models have been developed subsequently. One of these is the ρ model [76, 88] in which a constant scalar ρ is introduced to account for the fibre dispersion. The other is the κ model which is derived from a generalised structure tensor [75]. Both the ρ and the κ models are invariant-based and include the effect of fibre dispersion, but unlike ρ , κ can be directly estimated from the measured fibre density distributions using, for example, polarised light microscopy [6, 78–80]. In particular, the κ model extends the model of [1] by changing the anisotropic part to [75, 86]

$$\Psi_{\text{aniso}} = \frac{k_1}{2k_2} \sum_{i=4,6} \left[\exp(k_2 \hat{E}_i^2) - 1 \right], \quad (4.2)$$

where

$$\hat{E}_i = \kappa I_1 + (1 - 3\kappa)I_i - 1, \quad i = 4, 6,$$

and $\kappa \in [0, 1/3]$ is a dispersion parameter (the same for each fibre family). Notice that when $\kappa = 0$, the κ model is the same as the one published in [1], and when $\kappa = 1/3$ we recover the isotropic potential similar to that used in [89].

Recall from Eq. (2.6), that for the considered model the Cauchy stress tensor is given by

$$\boldsymbol{\sigma} = -\varrho \mathbb{I} + c\mathbb{B} + 2k_1 \sum_{i=4,6} \hat{E}_i \exp(k_2 \hat{E}_i^2) [\kappa \mathbb{B} + (1 - 3\kappa)(\mathbf{a}_i \otimes \mathbf{a}_i)],$$

in which $\mathbf{a}_i = \mathbb{F}\mathbf{a}_{0i}$, $i = 1, 2$, where ϱ is a *Lagrangian multiplier*.

We adopt the κ model in Eq. (4.2) and assume that the material properties of the abdominal aorta are the same as for the descending CIAs. Figure 4.4 shows a comparison between the experimental data and the fitted results for both the circumferential and axial direction of the medial and adventitial layers in the iliac artery. The ‘goodness

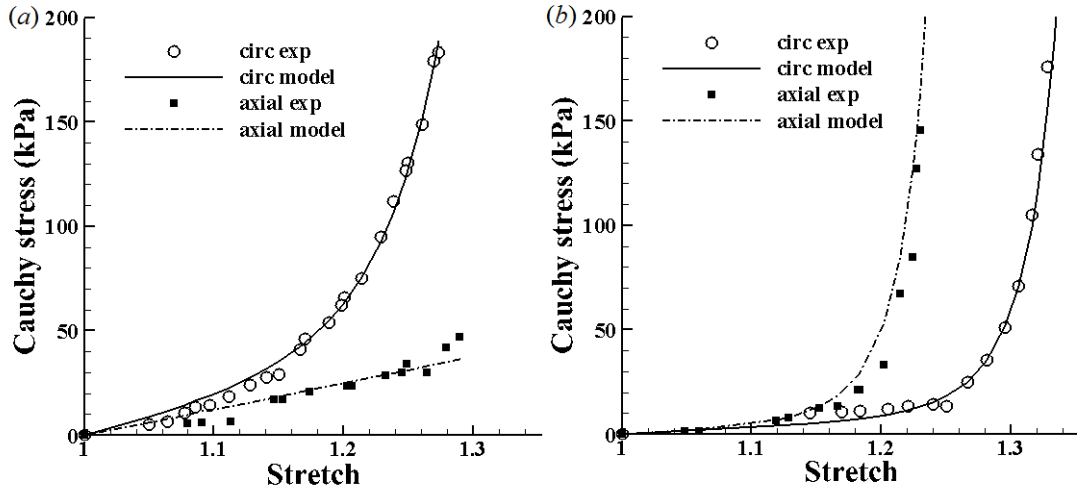


FIGURE 4.4: The circumferential and axial stress-stretch responses of (a) the medial and (b) the adventitial layers of a human iliac artery fitted to experimental data. The experimental data shown in symbols (circumferential: circle; axial: square) are from sample no. IV in [13]. The parameters used are listed in Table 4.1.

of fit', as defined in [7] and [6], is 0.09 and 0.16[†], respectively. The fitted material and structural parameters of a representative human iliac artery are given in Table 4.1, with the azimuthal angles β^j , $j = M, A$ determined from biaxial experiments [6].

TABLE 4.1: *Layer-specific material and structural parameters for a human CIA based on the κ model.*

	c [kPa]	k_1 [kPa]	k_2	κ [6]	β^j , $j = M, A$ [deg] [6]
Media	20.99	29.34	19.33	0.20	0
Adventitia	8.74	55.09	328.27	0.26	53.8

4.2.3 Finite element simulation

The finite element simulations were performed using the commercially available finite element package Abaqus 6.13 (SIMULIA, Providence, RI). For a typical simulation we use a total of 54,096 hexahedral elements for a bifurcation model, with 19,152 elements for the aorta, and 17,472 for each branch of the CIA. The grid size is chosen following a grid independence test[‡]. Each branch of the bifurcation is subjected to an *in vivo* axial pre-stretch of $\lambda_z = 1.07$ [7], defined as the ratio of *in situ* length to *ex situ* length [7, 90],

[†]As the value tends to zero, the fit becomes better.

[‡]Simulations were run for increasingly refined grids until the results converged; this is also called 'mesh convergence study'.

and a transmural physiological mean pressure of 100 mmHg [1, 7, 91]. The circumferential displacements of the inlet and outlets are fixed by setting these to zero in the locally cylindrical coordinate systems.

The simulation was run with different alignments of the fibres in the media of the descending iliac artery from $\beta^M = 0^\circ$ to 50° . The upper limit of 50° is used as it is widely accepted that the medial layer tends to support more circumferential than axial stresses, in the sense that the fibre orientation is closer to the circumferential direction than the axial direction [6]. When $\beta^M = 0^\circ$, the two families of fibres merge into a single family aligned along the circumferential direction. Except in the energy optimisation method discussed below, in all other simulation, the fibre angle β^A of the adventitia is fixed at 53.8° , following measurements documented in [6].

4.3 Criteria to determine the optimal angle

In order to determine the optimal fibre angle, we consider three different hypotheses. These are based on uniformity factor of the transmural stress distribution, stress-driven remodelling, and energy arguments.

4.3.1 Hypothesis I: uniformity factor

This approach assumes that the fibres are aligned so that under the peak blood pressure and an axial pre-stretch, the transmural gradient of the maximum principal Cauchy stress σ_θ is minimised. To start with, we assume that the unloaded configuration is stress-free, but this assumption is discarded later in Section 4.3.1.2. In accordance with [92], the distributions of these stresses are considered across the deformed wall thickness (including the medial and the adventitial layers). To quantify the uniformity of the circumferential stress throughout the arterial wall, we adopt the definition of the standard deviation as the uniformity factor (UF) [93], i.e.

$$\text{UF} = \left(\frac{1}{N-1} \sum_{n=1}^N (\sigma_{\theta n} - \bar{\sigma}_\theta)^2 \right)^{\frac{1}{2}},$$

where σ_{θ_n} is the circumferential Cauchy stress of the n -th sampling point through the iliac arterial wall (the daughter branches) and $\bar{\sigma}_\theta$ is the mean value of σ_{θ_n} across the wall. The number of sampling points N herein is 7, corresponding to the centre points of the finite elements across the wall. The transmural stress distributions at the pre-

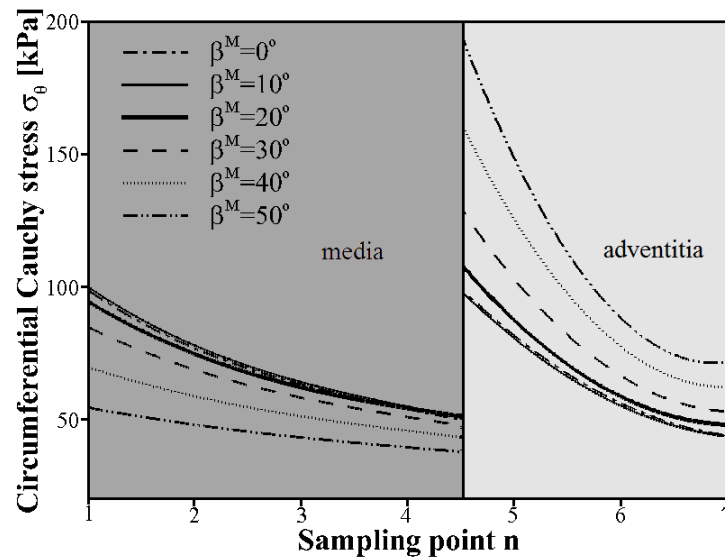


FIGURE 4.5: Transmural stress distribution σ_θ at different medial fibre angle alignments. The x-axis shows the sampling point n from the inner to the outer radius. The curves of the circumferential stress σ_θ are interpolated from the centre points of the finite elements. The thick solid curve at $\beta = 20^\circ$ is shown to be more uniform than all other angles since its UF value is the smallest, as listed at the bottom.

stretch of 1.07 are plotted in Fig. 4.5, indicating a distinct jump between the medial and adventitial layers. This agrees with published works [92, 94, 95], and is caused by the fact that different material parameters are used for the medial and adventitial layers. Another explanation of this piecewise pattern of the stress gap against the fibre angle $\beta^j, j = M, A$ is due to the fact that the collagen fibre constituent is the main contributor to the anisotropic behaviour. Under a constant β^A , the larger of β^M , the more effort it will contribute to support the axial forces and less to the circumferential ones. This then results in relieving the circumferential burden on medial layer while aggravating the one

on the adventitial layer. Therefore, there should exist a proper angle which makes the best balance of the stresses in those two layers, in other words, gives the smallest UF value.

Fig. 4.5 reveals that the transmural stress distribution becomes more uniform for both layers, for $\beta^M \leq 20^\circ$. Indeed, the UF value is quantitatively smallest when the fibre angle is set to be 20° , though the difference is small compared with that for $\beta^M = 0^\circ$.

4.3.1.1 Comparison between the bifurcation and the tube structure

To distinguish the effect of the pre-stretch from the bifurcation geometry, the simulations were run for several selective axial pre-stretches in addition to the physiological value of $\lambda_z = 1.07$, for both the bifurcation and the straight tube structure. All other parameters and loading conditions are kept the same as for the tube model. The optimal fibre angles from the UF criterion are listed in Table 4.2.

TABLE 4.2: *Optimal fibre angles with different pre-stretches for the bifurcation and the tube structure.*

λ_z	1.05	1.07	1.08	1.09	1.10	1.12	1.20
Bifurcation structure	30°	20°	10°	0°	0°	0°	0°
Tube structure	30°	20°	10°	0°	0°	0°	$0^\circ - 10^\circ$

Interestingly, Table 4.2 shows that the optimal fibre angles of the bifurcation and the tube structure are very similar. In other words, the effect of the pre-stretch seems to be much more important than the geometrical effects since, for a given pre-stretch, the optimal fibre angle is basically the same in either the bifurcation or the tube model under this hypothesis. This important observation suggests that we may now focus on the effects of the pre-stretch using the tube model for which the analytical solutions can be easily derived.

4.3.1.2 Effect of the circumferential residual stress

Since Table 4.2 shows that the optimal fibre angle is 20° , and not 0° , it suggests that our UF model has not captured all the important factors. One possibility is due to the fact

that the unloaded configuration is not stress free as we have assumed in our previous calculations. Several studies have shown that the circumferential residual stress can change the stress distribution through the thickness [93, 96–99].

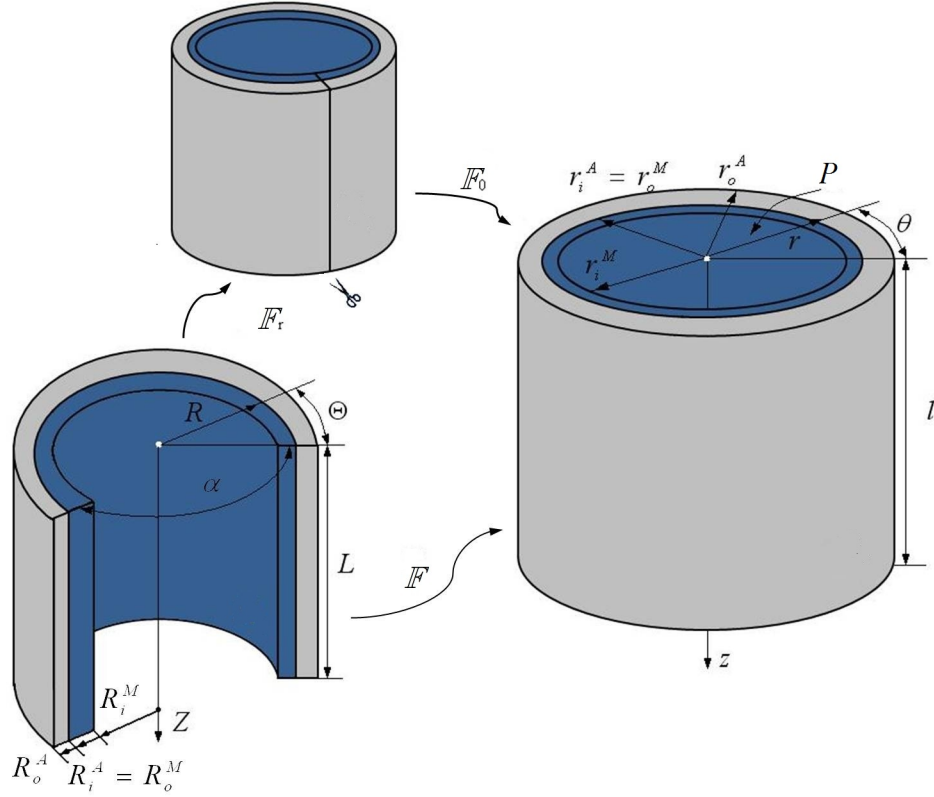


FIGURE 4.6: Cylindrical arterial wall in the stress-free configuration Ω_r , the unloaded configuration Ω_0 , and the current configuration Ω_t , replotted following [14].

To address this issue we introduce a circumferential residual stress based on the opening angle method [96]. Let α denote the opening angle in the reference configuration, as depicted in Fig. 4.6. Then, in terms of cylindrical polar coordinates (R, Θ, Z) , the reference geometry of the tube is defined by

$$R_i^M \leq R \leq R_o^A, \quad 0 \leq \Theta \leq 2\pi - \alpha, \quad 0 \leq Z \leq L, \quad (4.3)$$

where R_i^M and R_o^A denote the inner radius of the medial layer and the outer radius of the adventitial layer, respectively, while L is the length of the undeformed sector. For continuity, we also have $R_o^M = R_i^A$. Note that the opening angle identified in Fig. 4.6 differs from the definition used in [100, 101].

In terms of coordinates (r, θ, z) , the geometry of the current configuration is given by

$$r_i^M \leq r \leq r_o^A, \quad 0 \leq \theta \leq 2\pi, \quad 0 \leq z \leq l, \quad (4.4)$$

where r_i^M , r_o^A and l denote the inner and the outer radius and the length of the deformed tube, respectively, with $r_o^M = r_i^A$.

The deformation gradient \mathbb{F} is then the composition of the deformation gradient \mathbb{F}_0 relative to the unloaded configuration, and \mathbb{F}_r relative to the stress-free configuration, as indicated in Fig. 4.6. Thus,

$$\mathbb{F} = \mathbb{F}_0 \mathbb{F}_r. \quad (4.5)$$

Using the cylindrical coordinates we have $\mathbf{x} = r\mathbf{e}_r + z\mathbf{e}_z$, where $(\mathbf{e}_r, \mathbf{e}_\theta, \mathbf{e}_z)$ are the unit basis vectors in the current configuration. For our problem

$$r = \sqrt{\frac{R^2 - (R_i^M)^2}{k\lambda_z} + (r_i^M)^2}, \quad \theta = k\Theta, \quad z = \lambda_z Z, \quad (4.6)$$

where λ_z is the (constant) axial pre-stretch stretch, and $k = 2\pi/(2\pi - \alpha)$.

By incompressibility, $\lambda_r \lambda_\theta \lambda_z = 1$. Hence, we have

$$\lambda_r(R) = \frac{R}{rk\lambda_z}, \quad \lambda_\theta(R) = (\lambda_r \lambda_z)^{-1} = \frac{rk}{R}. \quad (4.7)$$

The deformation gradient is then

$$\mathbb{F} = \lambda_r \mathbf{e}_r \otimes \mathbf{E}_R + \lambda_\theta \mathbf{e}_\theta \otimes \mathbf{E}_\Theta + \lambda_z \mathbf{e}_z \otimes \mathbf{E}_Z, \quad (4.8)$$

with λ_m , $m = r, \theta, z$ being the principal stretches in the radial, circumferential and axial directions, respectively, and \mathbf{E}_m , $m = R, \Theta, Z$, are the unit basis vectors in the reference configuration. In the absence of body forces and by assuming no external pressure, the internal pressure P is

$$P = \int_{r_i^M}^{r_o^A} (\sigma_\theta - \sigma_r) \frac{dr}{r}, \quad (4.9)$$

where σ_θ and σ_r are the principal Cauchy stresses in the circumferential and the radial directions, respectively.

We need to make one assumption on the kinematics in order to make progress. To be specific, we assume that the wall thickness does not change between the initial and the stress-free configuration, following the studies of [93] and [1], and by making use of the incompressibility condition, we obtain

$$k(R_o^2 - R_i^2) = r_o^2 - r_i^2, \quad (4.10)$$

where $R_o = R_i + H$ and $r_o = r_i + H$, and H is the wall thickness. This allows us to solve Eq. (4.9) numerically using a Gaussian integration scheme [1]. The geometrical parameters used in the simulation are summarised in Table 4.3.

TABLE 4.3: *Geometrical parameters used for the iliac artery, chosen from [6–8]. As no measured opening angle is available for human iliac arteries, the corresponding opening angle of rat is used [1, 17] for both the medial and the adventitial layers.*

Parameter	Description	Value	
		Media	Adventitia
R_i [mm]	Inner referential radius	8.9	9.7
R_o [mm]	Outer referential radius	9.7	10.3
H [mm]	Wall thickness	0.8	0.6
r_i [mm]	Inner current radius	4.7	5.5
r_o [mm]	Outer current radius	5.5	6.1
α [deg]	Opening angle	160	160

The minimum values of UF versus the medial fibre angle β^M are illustrated in Fig. 4.7, which shows that when including the circumferential stress, the optimal fibre angle is around 0° . This now agrees with the experiments.

TABLE 4.4: *Minimum value of UF and corresponding β^M obtained for different values of pre-stretch λ_z , when including the opening angle ($\alpha = 160^\circ$).*

λ_z	1.00	1.05	1.07	1.10	1.14	1.15	1.17	1.20
β^M	0°	0°	0°	0°	0°	30°	41°	57°
UF _{min}	12.84	38.00	48.48	59.75	69.95	71.80	72.98	73.13

The minimum value of UF at different values of λ_z is shown in Table 4.4, which indicates a strong dependence of optimal β_M on λ_z . It seems that the medial fibres tend to be aligned in the circumferential direction when the pre-stretch is below 1.14. However, β^M increases sharply ($> 30^\circ$) for $\lambda_z > 1.15$, and the transmural stress distribution becomes more uneven. This is probably the reason why in human samples the corresponding angular deviation of the mean fibre angle in the media of iliac artery is close to 0° [6].

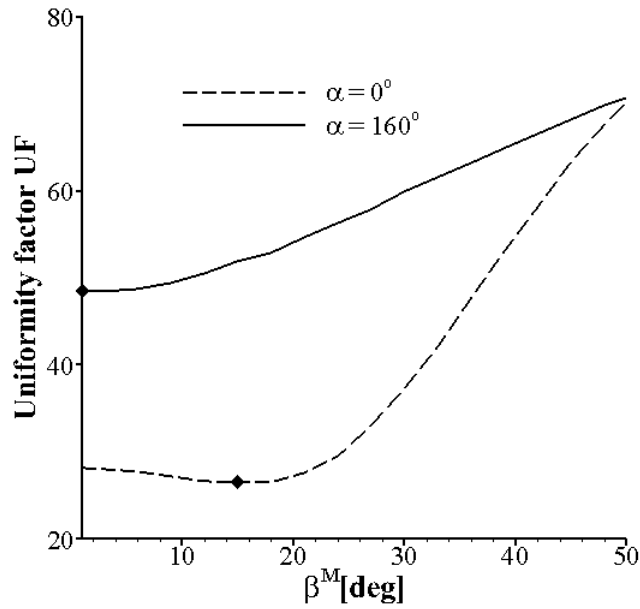


FIGURE 4.7: UF plotted against the fibre angle β^M for the opening angles $\alpha = 0^\circ$ (dashed curve) and $\alpha = 160^\circ$ (solid curve). The optimal fibre angle (solid diamond symbol) shifts from 16° to 0° when the circumferential residual stress is included in the model. Results are obtained for a pre-stretch value of $\lambda_z = 1.07$.

4.3.2 Hypothesis II: stress-driven remodelling

This hypothesis assumes that the fibres adapt during the remodelling process so that the artery layers have optimal load-bearing capability. Here we adopt a simple stress-driven remodelling model proposed by Hariton et al. [102], which assumes that the two families of collagen fibres are along a direction between the principal stretch directions as dictated by the ratio of the two largest principal stresses σ_θ and σ_z [102, 103]. In the present study, only the collagen fibre orientation in the medial layer is adjusted due to the remodelling process. Since remodelling requires the solution of an inverse problem, an iterative procedure is developed, as shown in Fig. 4.8.

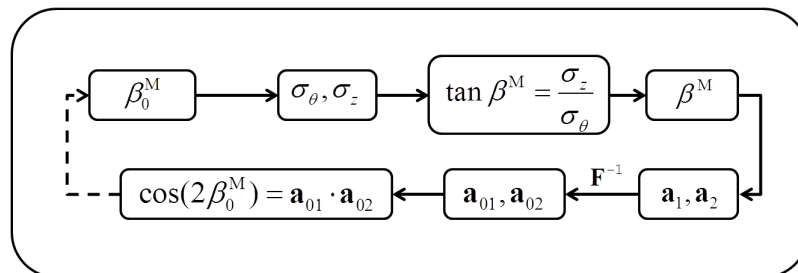


FIGURE 4.8: Inverse procedure for determining the fibre orientation using the stress-driven criterion.

The Cauchy stress is given by

$$\boldsymbol{\sigma} = \sigma_\theta \mathbf{e}_\theta \otimes \mathbf{e}_\theta + \sigma_z \mathbf{e}_z \otimes \mathbf{e}_z + \sigma_r \mathbf{e}_r \otimes \mathbf{e}_r,$$

where σ_m ($m = r, \theta, z$) are the principal Cauchy stresses, and \mathbf{e}_m ($m = r, \theta, z$) are the principal directions. Following [103] and [102], we assume that the angle β^M of fibre alignment between the fibre directions obeys

$$\tan \beta^M = \frac{\sigma_z}{\sigma_\theta}, \quad (4.11)$$

whereby the fibres are assumed to be in the plane spanned by the vectors aligned with the two largest principal stresses, and the collagen fibres are symmetrically aligned relative to \mathbf{e}_θ , the direction of the maximal principal stress. The two maximal principal stresses are obtained from the tube model. The unit vectors along the two families of collagen fibres are, in the current configuration,

$$\mathbf{a}_i = \cos \beta^M \mathbf{e}_\theta \pm \sin \beta^M \mathbf{e}_z,$$

and in the reference configuration,

$$\mathbf{a}_{0i} = \frac{\mathbf{F}^{-1} \mathbf{a}_i}{|\mathbf{F}^{-1} \mathbf{a}_i|}, \quad i = 1, 2.$$

The updated fibre alignment in the reference configuration is then calculated from

$$\cos(2\beta_0^M) = \mathbf{a}_{01} \cdot \mathbf{a}_{02}.$$

The remodelling procedure terminates when the maximal absolute variance of the mean fibre orientation between the current and last steps is below a set tolerance. For each step, we assume that the artery is in a quasi-static condition. To check that the convergence problem is unbiased of the initial value, we initialize the iterative procedure with three different mean fibre orientations (0° , 30° and 50°); Fig. 4.9 shows that all those three independent iterations converge to an identical result.

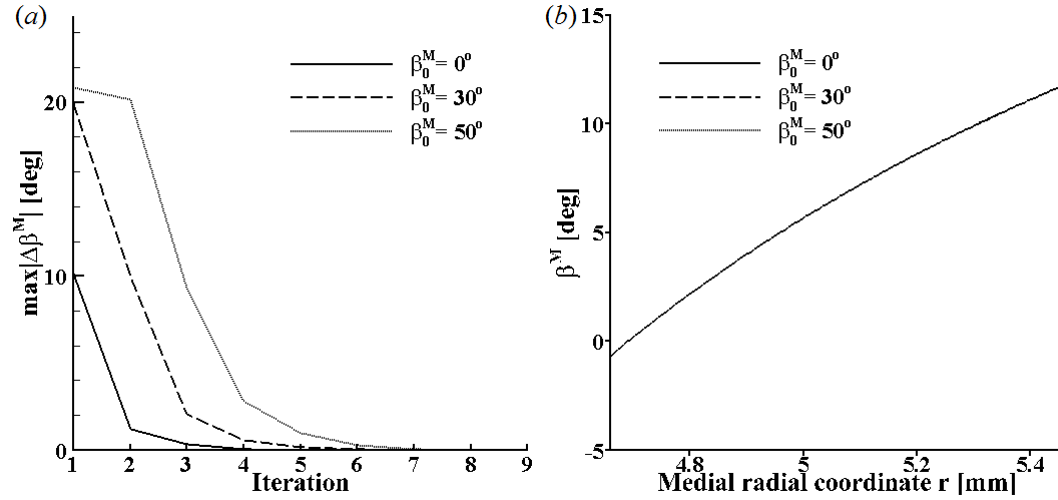


FIGURE 4.9: (a) The maximal medial fibre angle difference between two successive iterations and (b) the remodelled fibre orientation against the medial layer of the arterial wall at the pre-stretch 1.07. On one hand, all three simulations converge since the angle differences reach to zeros eventually and on the other hand, these convergent results are indistinguishable, in other words, they converge to the same results.

Figure 4.10 provides the results of the remodelling process with the circumferential residual stress under different pre-stretches. The mean fibre orientation across the arterial wall of the medial layer is 6.3° at a pre-stretch of $\lambda_z = 1.07$ as in Fig. 4.9. The result is reasonably close to zero degree, and suggests that the fibres are mostly circumferentially oriented. The influence of the axial pre-stretch is also shown in Fig. 4.10. On the whole, the values of the fibre angle increase with λ_z , while the range of β^M becomes wider when λ_z becomes larger. Note that if λ_z is assigned an even larger number (for example, > 1.13), the iterative system loses its stability, and it becomes divergent. The negative fibre angles proximal to the inner radius are due to the flip-over of the two fibre directions. Though uniformly stretched, the inner wall in the axial direction is under compression; in other words, the medial principal stresses $\sigma_z < 0$, and consequently, the β^M derived through Eq. (4.11) change their sign. The marginal differences in the optimal angles compared with the UF criterion may be due to the oversimplified criterion of the remodelling model used.

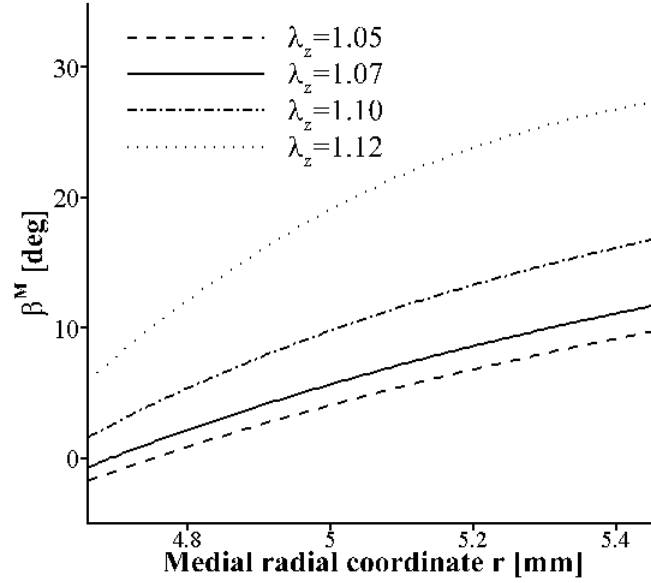


FIGURE 4.10: Dependence of the remodelled fibre orientation (characterized by β^M) on the medial radial coordinate r as a function of the axial pre-stretch given as 1.05 (dashed), 1.07 (solid), 1.10 (dash-dotted) and 1.12 (dotted). Residual strains are included through the opening angle of $\alpha = 160^\circ$.

4.3.3 Hypothesis III: energy-minimisation

We now determine the optimal fibre orientation based on the energy arguments recently proposed by Waffenschmidt and Menzel [14], which assumes that the fibres are aligned so that the minimum of total potential energy Π is maximised with respect to β^M and β^A . For a hyperelastic material, Π is the sum of the elastic strain energy Π_{int} stored in the deformed body and the potential energy Π_{ext} of the applied forces, expressed as $\Pi = \Pi_{\text{int}} + \Pi_{\text{ext}} + \text{const.}$ The main objective is to access information on the preferred material, structural and loading parameters that are associated with the extremal states of the total energy, and to use these to identify the favourable configurations for the design and adaptation of arterial walls. Specifically, the total energy for a tube model can then be expressed as

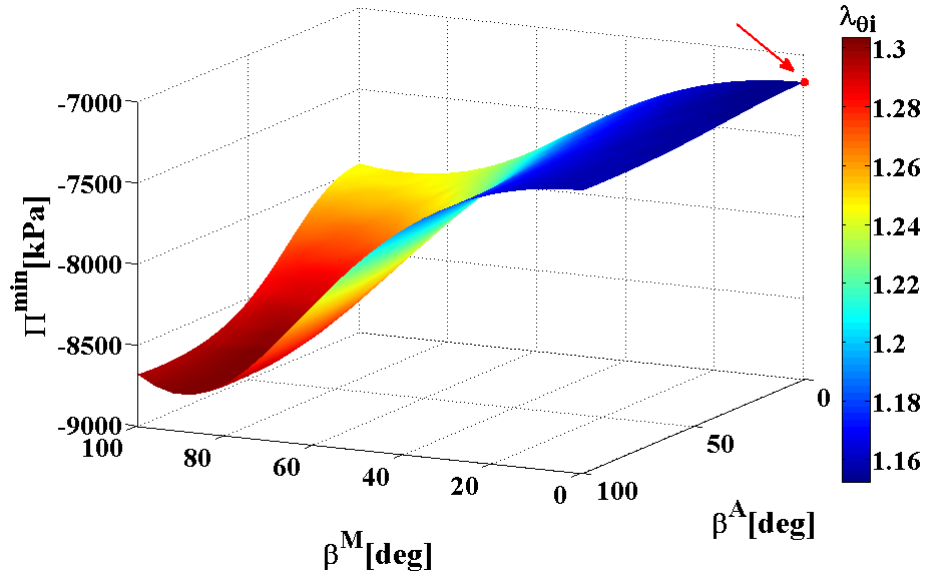
$$\Pi = 2\pi l \int_{r=r_i^M}^{r_o^A} \Psi(\lambda_r, \lambda_\theta, \lambda_z) r dr - P\pi(r_i^M)^2 l + \text{const.} \quad (4.12)$$

Note that λ_z is prescribed, and with the incompressibility condition $\lambda_r \lambda_\theta \lambda_z = 1$, the strain energy Ψ is a function of β^M , β^A , $\lambda_{\theta i}$ and α , where $\lambda_{\theta i}$ is the inner circumferential stretch.

Since the equilibrium of the system also requires the minimisation of the total strain energy in terms of displacements, the optimisation of the total energy is the result of maximising all the permissible minimised total energies. The solution of the underlying boundary-value problem is obtained by the optimisation of Π . The deformation variables $(\lambda_{\theta i}, \alpha)$ firstly minimise the total energy, which results in the triplet $(\lambda_{\theta i}^{\min}, \alpha^{\min}, \Pi^{\min})$. Subsequently, a set of values of Π^{\min} corresponding to the states of equilibrium for which Π^{\min} is maximised to render the optimal material parameters $(\beta_{\text{opt}}^M, \beta_{\text{opt}}^A)$, i.e.

$$\{\beta_{\text{opt}}^M, \beta_{\text{opt}}^A\} = \arg \max_{\beta^M, \beta^A} \{ \min_{\lambda_{\theta i}, \alpha} \Pi(\lambda_{\theta i}, \alpha, \beta^M, \beta^A) \}. \quad (4.13)$$

The reader is referred to [14] for the detailed algorithm that determines the functional



β^M [deg]	β^A [deg]	$\lambda_{\theta i}$ [-]	α [deg]
0	0	1.20	75

FIGURE 4.11: Values of Π^{\min} plotted against β^A and β^M , with the optimum values of the other parameters listed in the table. The red dot indicates the maximum value of Π^{\min} .

Π in Eq. (4.12). The physical interpretation of Eq. (4.13) suggests that in an arterial tissue, the fibres adapt to be aligned so that the tissue's loading capacity is maximised.

Thus, the internal energy is maximised among the minimised values of Π , in the case of Dirichlet boundary conditions.

Figure 4.11 shows the variation of the total potential energy Π in the parameter space of β^M and β^A . It is evaluated numerically at the physiological pressure of 13.33 kPa and the axial stretch of 1.07. In Fig. 4.11 the maximum value of Π^{\min} is indicated by a red dot, which occurs at $\beta^M = 0^\circ$. This is consistent with the results from the previous two hypotheses. The value of β^A is discussed in the next section.

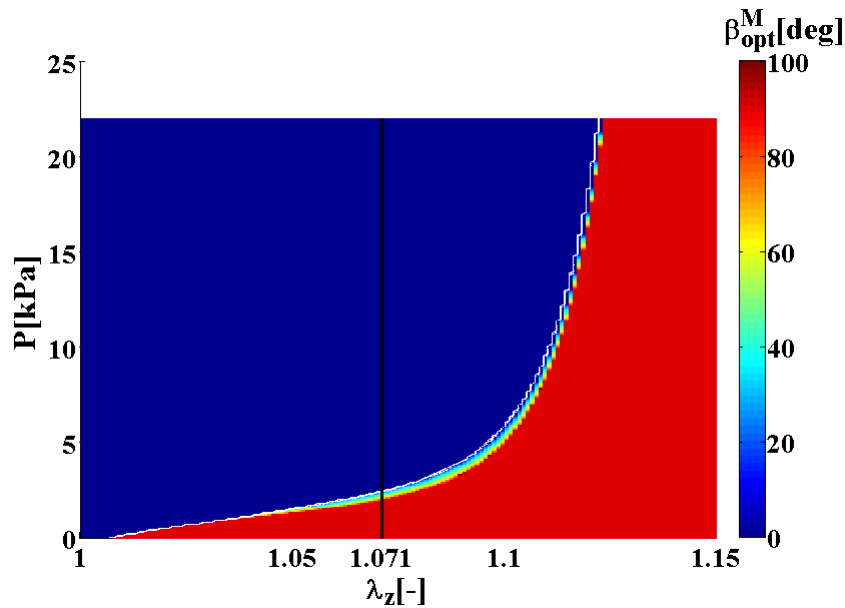


FIGURE 4.12: Relation between the axial stretch λ_z , internal pressure P , and optimal medial fibre angle β_{opt}^M , as indicated by the colour bar. The black solid line highlights the variation of β_{opt}^M with P at $\lambda_z = 1.07$; for a wide range of pressure ($\beta_{\text{opt}}^M = 0$).

Following [14], we also plot the relation between the axial stretch λ_z , the internal pressure P and the optimal medial fibre angle β_{opt}^M in Fig. 4.12, with the colour bar referring to the optimal value of β_{opt}^M . It is clear that in a wide range of physiological pressure, the optimal fibre angle is oriented towards the circumferential direction, i.e. $\beta_{\text{opt}}^M = 0^\circ$. However, if λ_z is > 1.12 , then there is a sudden change of fibre alignment from the circumferential to the axial direction, i.e. $\beta_{\text{opt}}^M = 90^\circ$, irrespective of the pressure magnitude. If we assign $\beta^A = 53.8^\circ$ [6], then the results are similar to those shown in Fig. 4.13(a). In particular, we have $\beta_{\text{opt}}^M = 0^\circ$, $\lambda_{\theta_i} = 1.23$, and $\alpha = 45^\circ$.

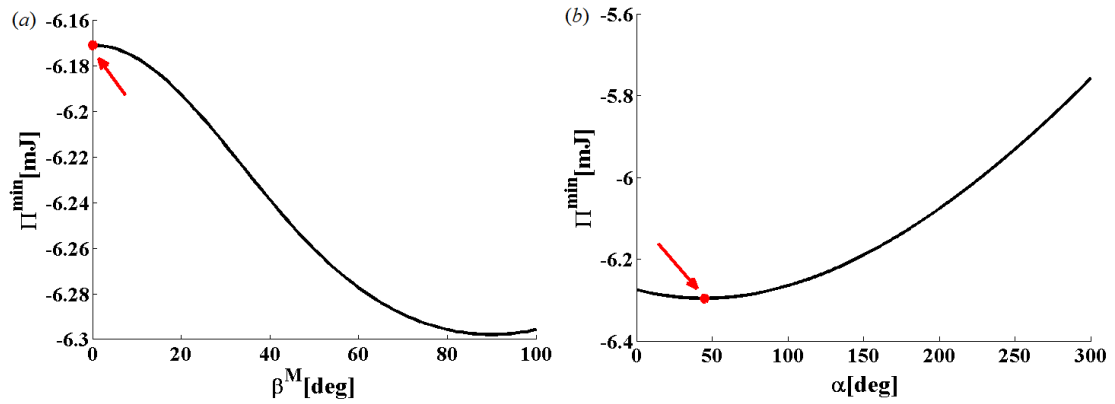


FIGURE 4.13: (a) Π^{\min} vs. β^M , with the red dot denoting $\beta_{\text{opt}}^M = 0^\circ$ when Π^{\min} reaches its maximum; (b) Π^{\min} vs. α , with the red dot denoting the optimal position at $\alpha = 45^\circ$ when Π is minimised.

4.4 Discussion

The main result of this chapter is to show that by using each of the three different hypotheses there seems to be an optimal mean fibre angle in the media of the human iliac artery in the circumferential direction, as observed in recent experiments of Schriefl et al. [6]. Since we only perform a static analysis, the agreement with experiments seems to suggest that the fibre alignments are dominantly influenced by the static peak physiological loading. In order to accurately estimate the fibre angle we need to include the residual stress effect in the UF approach since the arteries do not recover to the zero-stress configuration when unloaded.

In the first two approaches the fibre orientation of the adventitia is fixed. However, with the energy optimisation method, all parameters can be estimated including the opening angle α and the adventitial mean fibre orientation β^A . In all simulations, the importance of the pre-stretch in the determination of the fibre orientation is found to be paramount. This and several other issues are discussed in more detail in the following.

4.4.1 Role of pre-stretch

Our simulations suggest that the iliac artery has only one family of fibres in the media with preferred circumferential direction. Hence, it is useful to ask what is so special about the iliac artery when compared to the aorta where two families of fibres are

always present in each layer? The main explanation, as suggested by our results, comes from the significance of the pre-stretch. In particular, the typical pre-stretch in an iliac artery is around 1.07, yet in most of the large arteries such as the aorta and the carotid artery the pre-stretch is normally larger than 1.1 [1, 90, 92, 104–106].

Indeed, when we apply the UF criterion to rabbit carotid arteries using the data from [1], with the physiological value of pre-stretch 1.6, we find an optimal medial fibre angle of 31° (see UFs in the Table 4.5), which is close to the average experimental results of 29° [1]. Incidentally, the optimal fibre angles of the rabbit carotid artery would also be oriented towards the circumferential direction if the pre-stretches are below 1.45. Additionally, as suggested by the energy optimisation criterion, $\beta_{\text{opt}}^{\text{M}}$ is equal to 0° for an axial stretch below 1.55.

TABLE 4.5: *Optimal medial fibre angle β^{M} and corresponding UF_{min} at various values of pre-stretches λ_z for a rabbit carotid artery.*

λ_z	1.10	1.40	1.45	1.50	1.55	1.60	1.65	1.70
β^{M}	0°	0°	0°	2°	13°	31°	42°	50°
UF_{min}	49.79	71.86	75.62	79.29	82.65	83.82	81.52	74.92

We speculate that the reason for the lower value of the pre-stretch of the iliac artery is partially due to the branching structure, though not all bifurcating arteries have sufficiently low pre-stretch to develop a single fibre family. The spatial variation of the pre-stretch along the arterial tree must have been developed optimally through a complex remodelling process under the overall loading conditions, including dynamic pressure, gravity and fluid-structure interaction, with the interplay of local artery geometries and material properties. For example, in a human carotid bifurcation, the pre-stretch of the layer specific parent branch is very similar to that of the two daughter branches [107]. It will be interesting to see more experimental data which may establish a clearer relationship between the pre-stretch and the fibre orientation.

4.4.2 Opening angle in the human iliac artery

The energy optimisation method suggests that the optimal opening angle α is around 45° for a human iliac artery, as shown in Fig. 4.13(b). This is considerably lower than

the published opening angle of 160° found in a rat iliac artery [1, 17]. Since we have no experimental data available to validate this finding, we measured the opening angle in porcine iliac arteries of two healthy adult swines, following the procedure described by [108] and [109]. This measurement showed that the opening angle in the swine iliac artery is around 80° . As the swine anatomy bears some similarity to that of the human anatomy, this seems to support our modelling prediction of a smaller human opening angle of 45° . Using the opening angle 45° in the UF approach, we obtained a similar medial fibre angle to that of using 160° (rat), as shown in Table 4.6. Indeed, we have used a number of different opening angles and found that as the results are unchanged once the opening angle α is larger than 20° . This suggests that although the fibre orientation determined by the UF method requires the residual stress to be included, the final result is not sensitive to the changes of the opening angle as long as the opening angle is larger than a certain value. Indeed, the zero fibre angle in the medial layer holds true for a wide range of opening angles, which makes sense since the *in vivo* physiological residual stress must fluctuate due to the complex remodelling processes.

TABLE 4.6: *Optimal medial fibre angle β^M at various values of pre-stretches λ_z for human iliac arteries when the opening angle is set to 45° .*

λ_z	1.07	1.10	1.16	1.17	1.18	1.19	1.20
β^M	0°	0°	0°	30°	42°	50°	55°
UF _{min}	18.30	34.89	60.41	62.23	62.73	62.81	62.89

4.4.3 Adventitia fibre orientation β^A

In most of the simulations we have fixed the fibre angle β^A in the adventitial layer. However, with the energy optimisation hypothesis, the estimated β^A is 0° , which disagrees with the experimental measurement of 53.8° . In fact, Fig. 4.11 shows that the maximum value of Π^{\min} is insensitive to the variation of β^A ; the curve of Π^{\min} at $\beta^M = 0$ is rather flat for the whole range of β^A . This finding is consistent with the results on carotid arteries [14], and suggests that the energy optimisation method alone is not sufficient to determine β^A . Besides, the minor influence of β^A on the determination of the optimal fibre orientation in the medial layer is further confirmed via the sensitivity test under the other two hypotheses.

At this point, it is worth noting that Spencer et al. [110] considered a circular cylindrical tube of incompressible ideal fibre-reinforced material in which the reinforcement throughout its thickness is directed along two families of helices making angles of $\pm\beta^A$. Of particular importance, they argued that the relation of $\tan \beta^A = \sqrt{2}$, so that $\beta^A = 54.7^\circ$, holds in order to avoid the narrow bands of stress concentration near the surfaces of inner and outer radii. This value is surprisingly similar to the adventitial fibre angle measured in experiments [1, 6]. However, this should be viewed with caution since the fibres are assumed to be inappropriate to compare with the inextensible case in [110], and hence the agreement on the value of β^A could be a coincidence.

4.4.4 Limitations

We identified that the κ model is able to capture the mechanical response of the iliac artery, as, for example, documented in [13]. To this end, the parameters of the constitutive model, especially the structural parameter κ as introduced in [75], are obtained by means of the Levenberg-Marquardt algorithm. With the development of advanced experimental techniques, this particular parameter can be directly estimated from the measured fibre distribution density by, for example, a π -periodic *von Mises* distribution [75, 86]. However, such estimates are often different from the fitted values for the human iliac arteries [6]. An improved description of the mechanics of arterial walls at the microscopic level which can incorporate fibre-fibre interactions, fibre recruitment and viscoelasticity [111–113] will be required in the future in order to make full use of the experimental data.

Other limitations include the fact that we have only performed a static analysis. Moreover, with respect to the residual stresses, we have used the same constant parameters for the two layers of the arterial wall. The stress-free configuration changes over time so that the opening angles for the medial and adventitial layers and an intact artery ring vary significantly [76, 100, 114]. Although the present study reveals the potential link between the fibre orientation and the pre-stretch, we are yet unable to explain the reason for requiring different values of the pre-stretch in different sections of arteries.

Therefore, enhanced systematic studies including dynamic loading, fluid-structure interaction, and possibly tissue remodelling at the cellular level as well as measurements of fibre angles and pre-stretches for other arteries are required.

4.5 Conclusion

From a mechanical point of view we have suggested an explanation for the rather unusual fibre distribution in the medial layer of the human CIA. Three approaches have been used, namely a uniform distribution of the transmural stress, fibre stress remodelling, and optimisation of the total energy. All three approaches suggest that the optimal fibre angle in the medial layer of human iliac arteries is zero relative to the circumferential direction, as documented in [6]. In particular, we have found that the axial pre-stretch is key for explaining the optimal fibre distribution, and the particularly low value in the iliac artery is directly associated with the single fibre family. Moreover, we have shown the necessary involvement of the residual stress when utilising the UF approach, and we speculate that the opening angle in human iliac artery is around 45° . Finally, it is likely the case that the optimal fibre angle in the adventitia is determined by a different optimisation principle to that of the medial layer such as dynamic loading and fluid-structure interaction, which is a topic for future studies.

Chapter 5

The immersed boundary/finite element method

5.1 Models for blood and valve interaction

In this section, we address a number of different approaches to capture the interaction between blood and valve. Valve structure, as a typically thin structure, is different to model in the sense that the valve motion usually induces problems related to mesh quality. Other than accuracy, performance such as convergence and robustness of the method plays an even more important role in fluid-structure interaction (FSI) modelling [115].

In the FSI framework, the fluid domain is most conveniently described in Eulerian formulation, while the solid domain is more likely to be in Lagrangian description. The non-overlapping methods use two sets of different meshes and variables for fluid and solid, and consider the interface conditions as physical boundary conditions. The computational grid is fitted to and deforms with the moving boundary. The movement of the grid is taken into account by using the arbitrary Lagrangian Eulerian (ALE) formulation of the governing equations [116]. This ALE formulation has been previously applied to simulate the flow through mechanical heart valves [117–119]. It has proven to be an easy and accurate treatment of fluid-structure interfaces and permits significant

fluid sloshing and swirling to occur without producing excessive distortions of the computational mesh [120]. However, owing to the consistently large-deformed boundary of the thin valvular structure, some form of remeshing is generally needed as the process advances. This has, however, been known to not only introduce artificial diffusivity, but also to be challenging and time-consuming to perform with sufficient robustness and accuracy. This is particularly true for three-dimensional heart valves which are geometrically complex and involve large structural displacements [121].

To resolve this problem, overlapping methods are proposed. They have become increasingly popular in recent years, and have also been applied to simulate heart valve problems. These methods, in contrast to the non-overlapping methods, treat the boundary location and the related interface conditions as constraints imposed on the model equations so that the background fluid grid overlaps with the structural mesh. As a result, the fluid and/or the solid equations can be conveniently solved independently or use the no-slip conditions to update the structure mesh. In either case, re-meshing is not necessary. Since the grid used to discretize the fluid domain does not have to move with the immersed boundary, such methods are inherently applicable to moving boundary problems involving arbitrarily large structural displacements such as heart valves.

The fictitious domain (FD) method [122], one of the most popular overlapping methods, couples the two domains together at the solid/fluid interface through a Lagrangian multiplier so that the presence of a no-slip boundary at the location of the solid/fluid interface can be detected by the surrounding flow. The FD method has been applied to simulate flow in two-dimensional and three-dimensional trileaflet heart valves [123–125]. Van Loon et al. pointed out that one issue of the FD method is that it cannot yield accurate results for the viscous shear stresses on the solid boundary, and thus proposed a combination of the FD method with adaptive mesh refinement [126, 127].

On the other hand, the immersed boundary (IB) method is the earliest work to apply an overlapping method to simulate heart valves [128]. The effect of a moving immersed body on the fluid is accounted for by adding a body force to the governing equations of fluid motion [120]. Note that unlike in FD method where the momentum equations of both solid and fluid domains are solved, the fluid momentum is the only global governing

formulation in the IB framework. To improve the accuracy for high Reynolds number flows, second-order and/or adaptive IB methods were introduced [129–131]. IB methods have been widely used to simulate the dynamics of the heart and its valves [15, 131–136]. However, one major obstacle of the conventional IB method is that it uses the discrete collections of a fibre-like immersed elastic structure to represent the real valve. This assumption restrains realistic modelling of structures that may require complicated constitutive laws as well as an accurate representation of the finite volume they occupy within the fluid domain. Moreover, it is challenging to connect such description to experimental data. Recent extensions in the IB method are able to incorporate finite strain elasticity models for the solid region [137–141]. In the next several sections, we will present a detailed derivation and a numerical implementation of a method that merges the finite element description of the structure to the conventional IB method. It is called the immersed boundary finite element (IB/FE) method, proposed by Griffith and Luo [142].

5.2 The IB/FE formulations

The IB method is a mathematical formulation and numerical approach to FSI problem in which an elastic structure is immersed in a viscous incompressible fluid. This method was initiated by Peskin [143] in the 1970s. In particular, the IB/FE method expresses the stress using a FE Lagrangian description of the displacement of the immersed material along with a finite difference Eulerian description of the velocity and pressure of the coupled fluid [139]. In this method the presence of the immersed deformable solid boundary on the surrounding fluid grid nodes is accounted for by adding a body force in the Navier-Stokes equations. The body force is distributed over several fluid grid nodes in the vicinity of the boundary via a discrete delta function that has the effect of spreading the solid boundary.

In reference to Fig. 5.1, we first let $\Omega \subset \mathbb{R}^{3\dagger}$ denote the physical domain occupied by the fluid-structure system, and suppose that $U \subset \mathbb{R}^3$ identifies the structure in the

[†]We can define the physical domain on any dimensions as \mathbb{R}^d , however, d is normally taken as 2 or 3 for two- or three-dimensional regions.

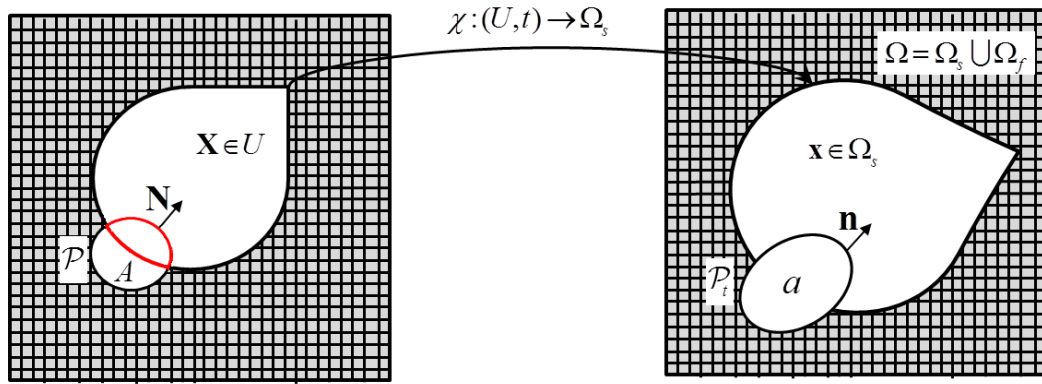


FIGURE 5.1: Evolution of a continuum material in IB method. If not specified, capital letters refer to the Lagrangian variables, and small letters refer to the Eulerian ones.

reference coordinate system. Let $\mathbf{x} = (x_1, x_2, x_3) \in \Omega$ denote the material particles, and $\mathbf{X} = (X_1, X_2, X_3) \in U$ denote the fluid particles. The mapping between the two frameworks is given by $\chi : (U, t) \mapsto \Omega_s$ representing the physical trajectory of material point \mathbf{X} at time t , so that $\mathbf{x} = \chi(\mathbf{X}, t) \in \Omega_s$ is the physical region occupied by the structure, and the physical region occupied by the fluid at time t is $\Omega_f = \Omega \setminus \Omega_s$.

We define the velocity of position \mathbf{x} at time t to be

$$\mathbf{u}(\mathbf{x}, t) = \frac{\partial \chi}{\partial t}(\mathbf{X}, t) = \frac{\partial \mathbf{x}}{\partial t}(\mathbf{X}, t),$$

and the acceleration by its material derivative as

$$\frac{D\mathbf{u}}{Dt}(\mathbf{x}, t) = \frac{\partial^2 \chi}{\partial t^2}(\mathbf{X}, t) = \frac{\partial \mathbf{u}}{\partial t} + \frac{\partial \mathbf{x}}{\partial t} \cdot \frac{\partial \mathbf{u}}{\partial \mathbf{x}} = \frac{\partial \mathbf{u}}{\partial t} + \mathbf{u} \cdot \nabla \mathbf{u}. \quad (5.1)$$

We assume there is no body force, and we consider an arbitrary smooth portion \mathcal{P} [†] evolving as $\mathcal{P}_t = \chi(\mathcal{P}, t)$, and let $\mathbf{N}(\mathbf{X})$ denote the exterior unit normal to $\mathbf{X} \in \partial\mathcal{P}$ in the Lagrangian configuration and $\mathbf{n}(\mathbf{x})$ be the exterior unit normal to $\mathbf{x} \in \partial\mathcal{P}_t$ in the Eulerian configuration. $dA(\mathbf{X})$ and $da(\mathbf{x})$ are the corresponding unit surface areas (as shown in Fig. 5.1). Hence, the conservations of the linear and angular momenta in an

[†]The portion \mathcal{P} can contain either solid or fluid material particles or both.

arbitrary portion \mathcal{P}_t in continuum mechanics can be expressed as

$$\int_{\mathcal{P}_t} \rho \frac{D\mathbf{u}}{Dt}(\mathbf{x}, t) d\mathbf{x} = \int_{\partial\mathcal{P}_t} \mathbf{t}(\mathbf{x}, \mathbf{n}, t) da, \quad (5.2)$$

$$\int_{\mathcal{P}_t} \mathbf{x} \times \rho \frac{D\mathbf{u}}{Dt}(\mathbf{x}, t) d\mathbf{x} = \int_{\partial\mathcal{P}_t} \mathbf{x} \times \mathbf{t}(\mathbf{x}, \mathbf{n}, t) da, \quad (5.3)$$

where \mathbf{t} is the surface force density (also known as the traction vector) and ρ is the Eulerian mass density.

From here, we obtain the strong formulation of the equation of motion

$$\rho \frac{D\mathbf{u}}{Dt}(\mathbf{x}, t) = \text{div} \boldsymbol{\sigma} \quad (5.4)$$

by

$$\int_{\partial\mathcal{P}_t} \mathbf{t} da = \int_{\partial\mathcal{P}_t} \boldsymbol{\sigma}^T \mathbf{n} da = \int_{\mathcal{P}_t} \text{div} \boldsymbol{\sigma} d\mathbf{x}, \quad (5.5)$$

in which we use the divergence theorem.

For any virtual displacement $\mathbf{v}(\mathbf{x})$, we have the principle of virtual work

$$\rho \int_{\mathcal{P}_t} \frac{D\mathbf{u}}{Dt} \cdot \mathbf{v} d\mathbf{x} = \int_{\mathcal{P}_t} \text{div} \boldsymbol{\sigma} \cdot \mathbf{v} d\mathbf{x}. \quad (5.6)$$

For notational convenience, we shall omit the dependent variables if they can be clearly demonstrated.

Again, using the divergence theorem, we have

$$\int_{\mathcal{P}_t} \nabla \cdot (\boldsymbol{\sigma} \cdot \mathbf{v}) d\mathbf{x} = \int_{\mathcal{P}_t} (\text{div} \boldsymbol{\sigma} \cdot \mathbf{v} + \boldsymbol{\sigma} : \nabla \mathbf{v}) d\mathbf{x} \quad (5.7)$$

$$= \int_{\partial\mathcal{P}_t} \boldsymbol{\sigma} \mathbf{n} \cdot \mathbf{v} da, \quad (5.8)$$

where the symbol ‘:’ is used (for example, in [1]) as a *tensor product contraction*, where $\boldsymbol{\sigma} : \nabla \mathbf{v} = \text{tr}(\boldsymbol{\sigma} \nabla \mathbf{v}) = \sigma_{\alpha\beta} \frac{\partial v_\alpha}{\partial x_\beta}$ in index notation. Then Eq. (5.6) becomes

$$\rho \int_{\mathcal{P}_t} \frac{D\mathbf{u}}{Dt} \cdot \mathbf{v} d\mathbf{x} + \int_{\mathcal{P}_t} \boldsymbol{\sigma} : \nabla \mathbf{v} d\mathbf{x} = \int_{\partial\mathcal{P}_t} \boldsymbol{\sigma} \mathbf{n} \cdot \mathbf{v} da \quad (5.9)$$

Specifically the total Cauchy stress $\boldsymbol{\sigma}$ in the coupled fluid-structure system reads

$$\boldsymbol{\sigma}(\mathbf{x}, t) = \begin{cases} \boldsymbol{\sigma}_f(\mathbf{x}, t) + \boldsymbol{\sigma}_e(\mathbf{x}, t), & \text{for } \mathbf{x} \in \Omega_s, \\ \boldsymbol{\sigma}_f(\mathbf{x}, t), & \text{otherwise,} \end{cases} \quad (5.10)$$

where $\boldsymbol{\sigma}_f$ is an incompressible Newtonian fluid-like stress tensor defined as

$$\boldsymbol{\sigma}_f(\mathbf{x}, t) = -p(\mathbf{x}, t)\mathbb{I} + \mu[\nabla\mathbf{u} + (\nabla\mathbf{u})^T], \quad (5.11)$$

in which μ is the viscosity and $p(\mathbf{x}, t)$ is the hydrostatic pressure. We can also regard p as the *Lagrange multiplier* associated with the incompressible constraints in terms of the Eulerian velocity field $\nabla \cdot \mathbf{u} = 0$. The term $\boldsymbol{\sigma}_e$ is the elastic structure stress satisfying $\int_{\partial\mathcal{P}} \mathbb{P}_e(\mathbf{X}, t) \mathbf{N} dA(\mathbf{X}) = \int_{\partial\mathcal{P}_t} \boldsymbol{\sigma}_e(\mathbf{x}, t) \mathbf{n} da(\mathbf{x})$ using Nanson's formula. We recall from Section 2.2 that $\mathbb{P}_e = J\boldsymbol{\sigma}\mathbb{F}^{-T}$, where \mathbb{F} is the deformation gradient and $F_{ij} = \frac{\partial x_i}{\partial X_j}$ and $J = \det\mathbb{F}$.

In the IB/FE method, the stress generated by the immersed structure \mathbb{P}_e is determined from the passive hyperelastic property by a strain energy functional Ψ as described in Section 2.4.

Therefore, with the separation in Eq. (5.10), Eq. (5.9) can be rewritten as

$$\rho \int_{\mathcal{P}_t} \frac{D\mathbf{u}}{Dt} \cdot \mathbf{v} d\mathbf{x} + \int_{\mathcal{P}_t} \boldsymbol{\sigma}_f : \nabla \mathbf{v} d\mathbf{x} + \int_{\mathcal{P}_t \cap \Omega_s} \boldsymbol{\sigma}_e : \nabla \mathbf{v} d\mathbf{x} = \int_{\partial\mathcal{P}_t} \boldsymbol{\sigma}_f \mathbf{n} \cdot \mathbf{v} da + \int_{\partial\mathcal{P}_t \cap \Omega_s} \boldsymbol{\sigma}_e \mathbf{n} \cdot \mathbf{v} da. \quad (5.12)$$

We treat the elastic part of the stress in terms of the first PK stress, which gives

$$\rho \int_{\mathcal{P}_t} \frac{D\mathbf{u}}{Dt} \cdot \mathbf{v} d\mathbf{x} + \int_{\mathcal{P}_t} \boldsymbol{\sigma}_f : \nabla \mathbf{v} d\mathbf{x} + \int_{\mathcal{P} \cap U} \mathbb{P}_e : \nabla \mathbf{V} d\mathbf{X} = \int_{\partial\mathcal{P}_t} \boldsymbol{\sigma}_f \mathbf{n} \cdot \mathbf{v} da + \int_{\partial\mathcal{P} \cap U} \mathbb{P}_e \mathbf{N} \cdot \mathbf{V} dA(\mathbf{X}), \quad (5.13)$$

where we defined $\mathbf{v}(\mathbf{x})$ evolving as $\mathbf{v}(\mathbf{x}) = \mathbf{V}(\mathbf{X}, t)$ so that $\mathbf{V}(\mathbf{X}, t)$ is an arbitrary Lagrangian test function that is not assumed to vanish on ∂U .

Using the same scheme as in Eq. (5.8), we have the identities

$$\begin{aligned} \int_{\mathcal{P}_t} (\nabla \cdot \boldsymbol{\sigma}_f) \cdot \mathbf{v} d\mathbf{x} &= \int_{\mathcal{P}_t} \operatorname{div} \boldsymbol{\sigma}_f \cdot \mathbf{v} d\mathbf{x} = - \int_{\mathcal{P}_t} \boldsymbol{\sigma}_f : \nabla \mathbf{v} d\mathbf{x} + \int_{\partial \mathcal{P}_t} \boldsymbol{\sigma}_f \mathbf{n} \cdot \mathbf{v} da, \\ \int_{\mathcal{P} \cap U} (\nabla_e \cdot \mathbb{P}_e) \cdot \mathbf{V} d\mathbf{X} &= \int_{\mathcal{P} \cap U} \operatorname{Div} \mathbb{P}_e \cdot \mathbf{V} d\mathbf{X} = - \int_{\mathcal{P} \cap U} \mathbb{P}_e : \nabla \mathbf{V} d\mathbf{X} + \int_{\partial(\mathcal{P} \cap U)} \mathbb{P}_e \mathbf{N} \cdot \mathbf{V} dA(\mathbf{X}), \end{aligned}$$

where $\mathcal{P} \cap \partial U = (\partial(\mathcal{P} \cap U)) \setminus (\partial \mathcal{P} \cap U)$ (highlighted in red in Fig. 5.1), so that Eq. (5.13) can then be expressed as

$$\begin{aligned} \int_{\mathcal{P}_t} \left(\rho \frac{D\mathbf{u}}{Dt} - \nabla \cdot \boldsymbol{\sigma}_f \right) \cdot \mathbf{v} d\mathbf{x} &= - \int_{\mathcal{P} \cap U} \mathbb{P}_e : \nabla \mathbf{V} d\mathbf{X} + \int_{\partial \mathcal{P} \cap U} \mathbb{P}_e \mathbf{N} \cdot dA(\mathbf{X}) \\ &= - \left(\int_{\partial(\mathcal{P} \cap U)} \mathbb{P}_e \mathbf{N} \cdot \mathbf{V} dA(\mathbf{X}) - \int_{\mathcal{P} \cap U} (\nabla_e \cdot \mathbb{P}_e) \cdot \mathbf{V} d\mathbf{X} \right) \\ &\quad + \int_{\partial \mathcal{P} \cap U} \mathbb{P}_e \mathbf{N} \cdot dA(\mathbf{X}) \\ &= \int_{\mathcal{P} \cap U} (\nabla_e \cdot \mathbb{P}_e) \cdot \mathbf{V} d\mathbf{X} - \int_{\mathcal{P} \cap \partial U} \mathbb{P}_e \mathbf{N} \cdot \mathbf{V} dA(\mathbf{X}). \quad (5.14) \end{aligned}$$

In continuum mechanics, the response of an elastic material to deformations is described through the deformation gradient \mathbb{F} ; however, in an Eulerian framework, there is no directly available scheme to achieve this [139]. We follow the method introduced in [144] to express the elastic stress in its natural Lagrangian coordinates. Instead of explicitly changing variables, we use the Dirac delta function $\boldsymbol{\delta}(\mathbf{x}) = \delta(x_1)\delta(x_2)\delta(x_3)$. We evaluate any function at a point by multiplying it by an appropriately shifted delta function and integrating over the entire space. For example,

$$\mathbf{V}(\mathbf{X}, t) = \mathbf{v}(\mathbf{x}) = \mathbf{v}(\boldsymbol{\chi}(\mathbf{X}, t)) = \int_{\mathcal{P}_t} \mathbf{v}(\mathbf{x}) \boldsymbol{\delta}(\mathbf{x} - \boldsymbol{\chi}(\mathbf{X}, t)) d\mathbf{x}. \quad (5.15)$$

We treat the interior force generated by the body and the transmission force density at the interface separately. Hence, $\mathbf{g}(\mathbf{x}, t)$ and $\mathbf{G}(\mathbf{X}, t)$ are defined as the Eulerian and Lagrangian internal elastic force densities, and $\mathbf{t}(\mathbf{x}, t)$ and $\mathbf{T}(\mathbf{X}, t)$ are the Eulerian and

Lagrangian transmission elastic force densities such that

$$\begin{aligned}\mathbf{G}(\mathbf{X}, t) &= \nabla_e \cdot \mathbb{P}_e(\mathbf{X}, t), \\ \mathbf{T}(\mathbf{X}, t) &= -\mathbb{P}_e(\mathbf{X}, t)\mathbf{N}(\mathbf{X})\end{aligned}$$

and

$$\begin{aligned}\mathbf{g}(\mathbf{x}, t) &= \int_U \mathbf{G}(\mathbf{X}, t) \delta(\mathbf{x} - \chi(\mathbf{X}, t)) d\mathbf{X}, \\ \mathbf{t}(\mathbf{X}, t) &= \int_U \mathbf{T}(\mathbf{X}, t) \delta(\mathbf{x} - \chi(\mathbf{X}, t)) d\mathbf{X}.\end{aligned}$$

The variational form of \mathbf{G} and \mathbf{T} are derived as

$$\begin{aligned}\int_{\mathcal{P} \cap U} (\nabla_e \cdot \mathbb{P}_e(\mathbf{X}, t)) \cdot \mathbf{V}(\mathbf{X}, t) d\mathbf{X} &= \int_{\mathcal{P} \cap U} \mathbf{G}(\mathbf{X}, t) \cdot \mathbf{V}(\mathbf{X}, t) d\mathbf{X} \\ &= \int_{\mathcal{P} \cap U} \mathbf{G}(\mathbf{X}, t) \cdot \int_{\mathcal{P}_t} \mathbf{v}(\mathbf{x}) \delta(\mathbf{x} - \chi(\mathbf{X}, t)) d\mathbf{x} d\mathbf{X} \\ &= \int_{\mathcal{P}_t} \int_{\mathcal{P} \cap U} \mathbf{G}(\mathbf{X}, t) \delta(\mathbf{x} - \chi(\mathbf{X}, t)) d\mathbf{X} \cdot \mathbf{v}(\mathbf{x}) d\mathbf{x} \\ &= \int_{\mathcal{P}_t} \int_U \mathbf{G}(\mathbf{X}, t) \delta(\mathbf{x} - \chi(\mathbf{X}, t)) d\mathbf{X} \cdot \mathbf{v}(\mathbf{x}) d\mathbf{x} \\ &= \int_{\mathcal{P}_t} \mathbf{g}(\mathbf{x}, t) \cdot \mathbf{v}(\mathbf{x}) d\mathbf{x},\end{aligned}$$

and similarly

$$-\int_{\mathcal{P} \cap \partial U} \mathbb{P}_e(\mathbf{X}, t) \mathbf{N}(\mathbf{X}) \cdot \mathbf{V}(\mathbf{X}, t) dA(\mathbf{X}) = \int_{\mathcal{P}_t} \mathbf{t}(\mathbf{x}, t) \cdot \mathbf{v}(\mathbf{x}) d\mathbf{x}.$$

Finally, taking into account of the incompressible assumption, we have

$$\nabla \cdot (\mu(\nabla \mathbf{u} + (\nabla \mathbf{u})^T)) = \mu \nabla^2 \mathbf{u}$$

and using Eqs. (5.1), (5.11), (5.14), we can summarize the strong form of the equations of motion for the FSI system as:

$$\rho \left(\frac{\partial \mathbf{u}}{\partial t}(\mathbf{x}, t) + \mathbf{u}(\mathbf{x}, t) \cdot \nabla \mathbf{u}(\mathbf{x}, t) \right) = -\nabla p(\mathbf{x}, t) + \mu \nabla^2 \mathbf{u}(\mathbf{x}, t) + \mathbf{f}(\mathbf{x}, t), \quad (5.16)$$

$$\mathbf{f}(\mathbf{x}, t) = \mathbf{g}(\mathbf{x}, t) + \mathbf{t}(\mathbf{x}, t), \quad (5.17)$$

$$\nabla \cdot \mathbf{u}(\mathbf{x}, t) = 0, \quad (5.18)$$

$$\frac{\partial \boldsymbol{\chi}}{\partial t}(\mathbf{X}, t) = \int_{\Omega} \mathbf{u}(\mathbf{x}, t) \boldsymbol{\delta}(\mathbf{x} - \boldsymbol{\chi}(\mathbf{X}, t)) d\mathbf{x}, \quad (5.19)$$

$$\mathbf{g}(\mathbf{x}, t) = \int_U \nabla_e \cdot \mathbb{P}_e(\mathbf{X}, t) \boldsymbol{\delta}(\mathbf{x} - \boldsymbol{\chi}(\mathbf{X}, t)) d\mathbf{X}, \quad (5.20)$$

$$\mathbf{t}(\mathbf{x}, t) = - \int_{\partial U} \mathbb{P}_e(\mathbf{X}, t) \mathbf{N}(\mathbf{X}) \boldsymbol{\delta}(\mathbf{x} - \boldsymbol{\chi}(\mathbf{X}, t)) dA(\mathbf{X}). \quad (5.21)$$

Although we refer to $\boldsymbol{\sigma}_e$ and \mathbb{P}_e as the structural stresses, we remark that they are not the total stresses of the immersed structure, but only account for the stresses associated with the hyperelastic material response. The total stress of the immersed structure is $\boldsymbol{\sigma} = \boldsymbol{\sigma}_f + \boldsymbol{\sigma}_e$; see in Eq. (5.10). The integral transform in Eq. (5.19) specifies that the velocity of the immersed structure is derived from the Eulerian velocity field $\mathbf{u}(\mathbf{x}, t)$. Eq. (5.19) is referred to as the *velocity interpolation*. Similarly, Eqs. (5.20), (5.21) are the *force spreading*. We note that Eq. (5.19) is equivalent to $\frac{\partial \boldsymbol{\chi}}{\partial t}(\mathbf{X}, t) = \mathbf{u}(\boldsymbol{\chi}(\mathbf{X}, t))$ due to the definition of $\boldsymbol{\delta}(\mathbf{x})$, which can be interpreted as non-slip condition or non-penetration condition. It further implies that if Eq. (5.18) holds, then $\partial J / \partial t = J \nabla \cdot \mathbf{u} = 0$. Consequently, if $J = 1$ at any time point, then $J = 1$ for all time.

There are two possible weak forms. The force formulations referred as the *unified weak form* are

$$\begin{aligned} \mathbf{f}(\mathbf{x}, t) &= \int_U \mathbf{F}(\mathbf{X}, t) \boldsymbol{\delta}(\mathbf{x} - \boldsymbol{\chi}(\mathbf{X}, t)) d\mathbf{X} \\ \int_U \mathbf{F}(\mathbf{X}, t) \cdot \mathbf{V}(\mathbf{X}) d\mathbf{X} &= - \int_U \mathbb{P}_e(\mathbf{X}, t) : \nabla_{\mathbf{X}} \mathbf{V}(\mathbf{X}) d\mathbf{X} \\ &= \int_U (\nabla_e \cdot \mathbb{P}_e(\mathbf{X}, t)) \cdot \mathbf{V}(\mathbf{X}, t) d\mathbf{X} - \int_{\partial U} \mathbb{P}_e(\mathbf{X}, t) \mathbf{N}(\mathbf{X}) \cdot \mathbf{V}(\mathbf{X}, t) dA(\mathbf{X}). \end{aligned} \quad (5.22)$$

in which $\mathbf{F}(\mathbf{X}, t)$ is the total Lagrangian elastic force density.

Another weak formulation for the definition of \mathbf{f} is to only do variational transformation on \mathbf{G} only. This is referred to as the *partitioned weak form* and is introduced as

$$\begin{aligned} \mathbf{g}(\mathbf{x}, t) &= \int_U \mathbf{G}(\mathbf{X}, t) \delta(\mathbf{x} - \boldsymbol{\chi}(\mathbf{X}, t)) d\mathbf{X}, \\ \int_U \mathbf{G}(\mathbf{X}, t) \cdot \mathbf{V}(\mathbf{X}) d\mathbf{X} &= - \int_U \mathbb{P}_e(\mathbf{X}, t) : \nabla_{\mathbf{X}} \mathbf{V}(\mathbf{X}) d\mathbf{X} + \int_{\partial U} \mathbb{P}_e(\mathbf{X}, t) \mathbf{N}(\mathbf{X}) \cdot \mathbf{V}(\mathbf{X}, t) dA(\mathbf{X}). \end{aligned} \quad (5.23)$$

Though these two weak forms are equivalent in the continuous setting, they lead to different numerical schemes [142].

5.3 The IB/FE numerical scheme

In the numerical implementation, the Eulerian equations of motion are discretized by a finite difference method on an adaptive, staggered grid, and the Lagrangian equations are discretized using a finite element mesh.

5.3.1 Spatial discretizations

The discretization of the incompressible Navier-Stokes equations in space is the same as in IB method [145, 146], where we employ a locally refined staggered-grid Eulerian spatial discretization.

Briefly stated, the components of the Eulerian velocity field \mathbf{u} and body force \mathbf{f} are approximated at the edge centres of the Cartesian grid cells; however, the pressure p is approximated at the cell centres. Let $\nabla_h \cdot$, ∇_h and ∇_h^2 denote the standard staggered-grid finite difference approximations to the divergence, gradient and Laplace operators, respectively. Note that, $\nabla_h \cdot \nabla_h = \nabla_h^2$ [146]. Accordingly, $\nabla_h \cdot \mathbf{u}$ is defined at the cell centres, while $\nabla_h p$ and $\nabla_h^2 \mathbf{u}$ are defined at the cell edges. More details are given in [135].

Herein, we would like to draw more attention to the Lagrangian finite element scheme, which is one of the major features in the IB/FE framework. Let \mathcal{T}_h be a subdivision of U into elements U^e and denote by $\{\mathbf{X}_l\}_{l=1}^M$ the nodal variables of the mesh, and by

$\{\phi_l(\mathbf{X})\}_{l=1}^M$ the Lagrangian basis function. We can thus define an approximation to $\chi(\mathbf{X}, t)$ by

$$\chi_h(\mathbf{X}, t) = \sum_{l=1}^M \mathbf{X}_l(t) \phi_l(\mathbf{X}). \quad (5.24)$$

Hence, the discretized Lagrangian force densities $\mathbf{F}(\mathbf{X}, t)$ and $\mathbf{G}(\mathbf{X}, t)$ are

$$\mathbf{F}_h(\mathbf{X}, t) = \sum_{l=1}^M \mathbf{F}_l(t) \phi_l(\mathbf{X})$$

and

$$\mathbf{G}_h(\mathbf{X}, t) = \sum_{l=1}^M \mathbf{G}_l(t) \phi_l(\mathbf{X}).$$

The nodal values of $\{\mathbf{F}_l\}_{l=1}^M$ and $\{\mathbf{G}_l\}_{l=1}^M$ are determined from approximations to the first PK stress tensor using Eq. (5.24). By restricting the test functions \mathbf{V} to be linear combinations of the interpolatory Lagrangian basis functions as in the traditional Galerkin finite element method [147], we can rewrite Eqs.(5.22) and (5.23)

$$\sum_{l=1}^M \left(\int_{U^e} \phi_l(\mathbf{X}) \phi_m(\mathbf{X}) d\mathbf{X} \right) \mathbf{F}_l(t) = - \int_{U^e} \{\mathbb{P}_e\}_h(\mathbf{X}, t) \nabla_{\mathbf{X}} \phi_m(\mathbf{X}) d\mathbf{X}, \quad (5.25)$$

$$\begin{aligned} \sum_{l=1}^M \left(\int_{U^e} \phi_l(\mathbf{X}) \phi_m(\mathbf{X}) d\mathbf{X} \right) \mathbf{G}_l(t) &= - \int_{U^e} \{\mathbb{P}_e\}_h(\mathbf{X}, t) \nabla_{\mathbf{X}} \phi_m(\mathbf{X}) d\mathbf{X} \\ &+ \int_{\partial U^e} \{\mathbb{P}_e\}_h(\mathbf{X}, t) \mathbf{N}(\mathbf{X}) \phi_m(\mathbf{X}) dA(\mathbf{X}) \end{aligned} \quad (5.26)$$

for $m = 1, \dots, M$.

Now let $[\mathbf{F}]$ denote the vector of nodal coefficients of \mathbf{F}_h . We rewrite Eq.(5.25) as

$$[\mathcal{M}][\mathbf{F}] = [\mathcal{B}], \quad (5.27)$$

in which the mass matrix $[\mathcal{M}]$ has index form $M_{ml} = \int_{U^e} \phi_l \phi_m d\mathbf{X}$, and $[\mathcal{B}]$ is a vector with components $B_m = - \int_{U^e} \{\mathbb{P}_e\}_h(\mathbf{X}, t) \nabla_{\mathbf{X}} \phi_m d\mathbf{X}$.

5.3.2 Lagrangian-Eulerian interactions

To compute the *force spreading* from the Lagrangian force density to Eulerian force density on the Cartesian grid, we construct for each element $\mathbf{U}^e \in \mathcal{T}_h$ a Gaussian quadrature rule. We use the shorthand

$$\mathbf{f} = \mathcal{S}\mathbf{F}, \quad (5.28)$$

where $\mathcal{S}(\boldsymbol{\chi})$ is the force-prolongation operator.

Correspondingly, a velocity-restriction operator $\mathcal{R}(\boldsymbol{\chi})$ is determined via

$$\frac{d\boldsymbol{\chi}}{dt} = \mathcal{R}\mathbf{u}. \quad (5.29)$$

The operator \mathcal{R} defined here is the adjoint expression of \mathcal{S} , so $\mathcal{R} = \mathcal{S}^*$ and we do not need to compute it explicitly [142]. Because the same kernel $\boldsymbol{\delta}_h$ is used in the spreading and interpolation steps, the mass, force and torque are conserved during Lagrangian-Eulerian interaction [144].

For the staggered-grid discretization and the locally-refined, adaptive grid construction, one can refer to [135] and [145, 146], respectively.

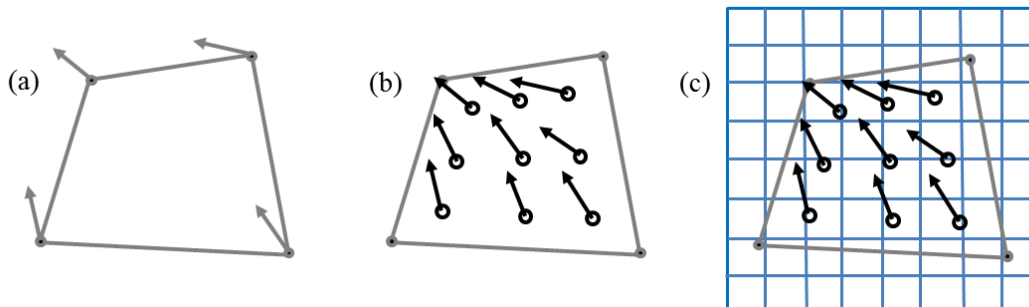


FIGURE 5.2: The procedure of prolonging the elastic force density from (a) the Lagrangian nodes onto (b) Gaussian quadrature points and then onto (c) the Cartesian grid.

In this context, we emphasize the implementation of the force prolongation. As indicated in Fig. 5.2, we start with an approximation to the force density at the nodes of the Lagrangian mesh, we use the FE basis functions to approximate the force density at

quadrature points in the element interior, and then spread the interpolated forces from the quadrature points to the background Eulerian grid using the smoothed delta function $\delta_h(\mathbf{x})$. This approach permits the Lagrangian mesh to be significantly coarser than the Eulerian grid as long as the net or submesh of quadrature points is sufficiently dense. Denser nets of quadrature points can be obtained by increasing the order of the numerical quadrature scheme.

5.3.3 Temporal discretizations

The IB/FE method has the same temporal discretization as the IB method where we employ a simple unsplit second-order scheme to discretize the equations in time [142, 146]. We take the *unified weak form* as an example, and let $\boldsymbol{\chi}^n$, \mathbf{u}^n denote the approximations to the values of $\boldsymbol{\chi}$ and \mathbf{u} at time t^n , and $p^{n-\frac{1}{2}}$ to the value of p at time $t^{n-\frac{1}{2}}$, respectively. To advance $\boldsymbol{\chi}$, \mathbf{u} and p forward in time, we first evaluate the intermediate structure configuration by

$$\boldsymbol{\chi}^{n+\frac{1}{2}} = \frac{\tilde{\boldsymbol{\chi}}^{n+1} + \boldsymbol{\chi}^n}{2}$$

where $\tilde{\boldsymbol{\chi}}^{n+1}$ is computed by

$$\frac{\tilde{\boldsymbol{\chi}}^{n+1} - \boldsymbol{\chi}^n}{\Delta t} = \mathcal{S}^*(\boldsymbol{\chi}^n)\mathbf{u}^n.$$

Then the corresponding intermediate Eulerian force density follows

$$\mathbf{f}^{n+\frac{1}{2}} = \mathcal{S}(\boldsymbol{\chi}^{n+\frac{1}{2}})\mathbf{F}^{n+\frac{1}{2}}.$$

We then solve the momentum equation as

$$\rho \left(\frac{\mathbf{u}^{n+1} - \mathbf{u}^n}{\Delta t} + \tilde{\mathbf{A}}^{n+\frac{1}{2}} \right) = -\nabla_h p^{n+\frac{1}{2}} + \mu \nabla_h^2 \frac{\mathbf{u}^{n+1} + \mathbf{u}^n}{2} + \mathbf{f}^{n+\frac{1}{2}}, \quad (5.30)$$

$$\nabla_h \cdot \mathbf{u}^{n+1} = 0, \quad (5.31)$$

where the nonlinear advection term $\tilde{\mathbf{A}}^{n+\frac{1}{2}}$ is determined by a second-order Adams-Bashforth scheme, so that $\tilde{\mathbf{A}}^{n+\frac{1}{2}} = \frac{3}{2}\mathbf{A}^n - \frac{1}{2}\mathbf{A}^{n-1}$ with $\mathbf{A}^n = \mathbf{u}^n \cdot \nabla_h \mathbf{u}^n$. It also requires a Crank-Nicolson-type discretization for the viscous term [145].

For computing χ^{n+1} , we utilize again the intermediate structure configuration such that

$$\frac{\chi^{n+1} - \chi^n}{\Delta t} = \mathcal{S}^*(\chi^{n+\frac{1}{2}}) \frac{\mathbf{u}^{n+1} + \mathbf{u}^n}{2}.$$

To initialize, due to the timestep-lagged treatment, we instead use a two-step predictor-corrector method. We firstly predict the values of χ , \mathbf{u} and p at time t^{n+1} (symbolised as $\tilde{\chi}^{n+1}$, $\tilde{\mathbf{u}}^{n+1}$ and \tilde{p}^{n+1}) by their values at t^n and assign $p^{n+\frac{1}{2}} = 0$. Then these values are corrected by setting $\chi^{n+\frac{1}{2}} = \frac{\tilde{\chi}^{n+1} + \chi^n}{2}$ as in the main loop. The only difference is that we use $\tilde{\mathbf{A}}^{n+\frac{1}{2}} = \mathbf{u}^{n+\frac{1}{2}} \cdot \nabla_h \mathbf{u}^{n+\frac{1}{2}}$, in which $\mathbf{u}^{n+\frac{1}{2}} = \frac{1}{2}\tilde{\mathbf{u}}^{n+1} + \mathbf{u}^n$.

5.4 Summary

The conventional IB scheme is only first order accurate [128], but the IB/FE method described above is a formally second-order accurate scheme and combines adaptive mesh refinement and staggered-grid scheme to increase resolution in the vicinity of immersed boundaries. Apart from this, one other significant advantage is that the standard IB method uses regularized delta functions to apply nodal forces directly to the Cartesian grid and to interpolate Cartesian grid velocities directly to the Lagrangian nodes [144]. This requires the Lagrangian mesh to be finer than the Cartesian grid to avoid leaks; the ratio between the Eulerian and Lagrangian mesh sizes is advised to be at least 2:1 [144]. This requirement will induce the time steps to be sufficiently small to satisfy the CFL condition. However, in the IB/FE method, as illustrated in Fig. 5.2, the Lagrangian structure is watertight as long as the net of quadrature points is sufficiently dense by controlling the order of the quadrature rule. Another key advance is the introduction of the FE description of the structure. This enables us to include linear and nonlinear constitutive laws to represent real biological tissues.

To implement this IB/FE method, the numerical simulations in the following chapters employ an open-source IB adaptive mesh refinement (AMR) software framework (<http://ibamr.googlecode.com>), which provides an adaptive and distributed-memory parallel implementation of the IB/FE method. Support for distributed-memory parallelism is via the Message Passing Interface. IBAMR leverages functionality provided by SAMRAI, the Structured Adaptive Mesh Refinement Application Infrastructure, who supports for spatial adaptivity (<https://computation.llnl.gov/casc/SAMRAI>) and other freely available software libraries, including PETSc (<http://www.mcs.anl.gov/petsc>), *hypre* (<http://www.llnl.gov/CASC/hypre>) and HDF5 (<http://www.hdfgroup.org/HDF5/>).

Chapter 6

A fluid-structure interaction model of a nonlinear human mitral valve

In this chapter, a simulated human mitral valve (MV) model interacting with blood flow under a physiological pressure loading is developed using the hybrid IB/FE method described in Chapter 5. Most of the contents in this chapter has been published in *International Journal for Numerical Methods in Biomedical Engineering* [148].

6.1 Introduction

Dysfunction of the MV causes significant morbidity and premature mortality, and remains a major medical problem worldwide. Understanding biomechanics of human MV can lead to the development of new therapies and treatment strategies. Dynamic modelling of the MV is particularly difficult due to the large deformation of the non-symmetric leaflets, the anisotropic nonlinear elastic behaviour of the valvular tissue, the fluid-structure interaction, and the pulsatile haemodynamic loading during the cardiac cycles.

Ex-vivo biaxial testing of the anterior and posterior leaflets [28, 149] has revealed that both leaflets exhibit large deformations and behave as anisotropic materials, being stiffer along the circumferential direction, with the collagen fibres oriented predominantly parallel to the annulus. Other mechanical tests on porcine and human mitral apparatus by Prot et al. [150–153], and Wang et al. [27] also suggest that the MV leaflets are highly nonlinear and anisotropic. The *in vivo* mechanical properties of the human MV are not readily attainable, although limited data has been obtained from animal tests with minimum invasiveness and via inverse FE analyses. For example, Krishnamurthy et al. [154] estimated the mechanical response of the anterior mitral leaflets based on radiopaque markers sewn to sheep MVs, albeit with a linear isotropic material model. Lee et al. [155] inversely estimated the *in vivo* material properties of ovine MV anterior leaflets with various nonlinear anisotropic hyperelastic constitutive laws, and found that the transversely isotropic law produced the most accurate results.

Computational MV models have been investigated by a number of groups, mostly focusing on the MV structure without the interaction with blood. Kunzelman and co-workers were the first to use a three-dimensional finite element (FE) model to simulate normal MV [156], the mechanical analysis with valvular disease [157, 158], and surgical interventions [158, 159]. Later on, Prot et al. [150–152] reported their work on MV simulations in a series of studies using a transversely isotropic strain-energy function in their nonlinear FE simulations. Their model was later extended to predict the stress distributions on a healthy MV and a diseased MV in a hypertrophic obstructive cardiomyopathic heart [153]. Active muscle contraction of MV was also studied [160], which is considered to reduce the leaflet bulging. The effects of the annular contraction on MV stress were modelled by Stevanella et al. [161, 162]. One limitation in most of the aforementioned studies is that the valve geometries were typically assumed to be symmetric about the mid-line of the two leaflets. However, asymmetric stress patterns of an ovine MV have been reported by Lim et al. [163]. Wenk et al. [164] developed a FE model consisting of the left ventricle, mitral apparatus, and chordae tendineae from magnetic resonance (MR) images from a sheep. Recently, Wang et al. [27] presented a patient-specific FE model of a healthy human MV reconstructed from multi-slice computed tomography scans with detailed mitral leaflet thickness, chordal information and mitral

annulus dynamic motion. Surgical procedures were also investigated using structural FE models [165–168].

Although these structural models are very useful for simulating static configurations at the fully opened or fully closed states, fluid-structure interaction (FSI) needs to be accounted for to describe the dynamics of the MV due to its strong interaction to the blood flow [169]. Kunzelman, Einstein and co-workers started to use a fluid-coupled three-dimensional computational model to simulate normal and pathological mitral function [2, 170, 171]. In [2], valve closure was characterised by positioning the valve in a tubular fluid domain. Lau et al. [172] investigated the edge-to-edge repair technique with FSI, and found that after the repair, the stress is twice greater than in the normal case, and there is almost half reduction in the peak flow rate. The above studies all used the commercial package LS-DYNA (Livermore Software Technology Corporation, Livermore, CA) to implement FSI. Additionally, Ravoooh et al. [127] addressed two-dimensional computations of a MV motion in a pulsatile blood flow, using FSI method combined with solid-rigid contact, where the FSI was realized via a fictitious domain method extended with a local mesh adaptation.

Over the last few years, the Glasgow group has used the open source IB method to model three-dimensional FSI models of a polyurethane prosthetic MV and a MR imaged-derived human MV [15, 144, 173, 174]. We discovered that, despite being very thin, the bending rigidity of the MV leaflets is highly relevant to the effective MV closing [136]. The bending effect of the MV is also confirmed by a recent study of human MV [15] reconstructed from *in vivo* MR images showing that patient-specific MV geometry has a significant influence on the simulation results. One major limitation of these studies is that the MV is modelled with assumed discrete isotropic ‘elastic fibres’, which is not suitable to model the realistic, anisotropic mechanical behaviour of the MV leaflets [151, 175].

The aim of this chapter is to overcome the structural simplification of the previous MV models by developing a MV model using the recent IB/FE method. It has been carefully verified against the commercial package Abaqus 6.13 (SIMULIA, Providence, RI) [176], and the results showed that the IB/FE model is capable of predicting quantitatively

accurate stress/strain distributions of the left ventricle. Our MV model is again constructed from a set of human MR images, and the IB/FE approach enables us to model the MV tissue behaviour using a transversely isotropic model, together with the fully dynamic three-dimensional FSI. This is a major step forward from the previous work by Ma et al. [15].

6.2 Methodology

6.2.1 MV geometrical model

An MR imaging study was performed on a healthy 28-year-old male volunteer using a 3-Tesla MR image system (Verio, Siemens, Germany). The study was approved by the local NHS Research Ethics Committee, and an informed consent was signed before the scan. Twelve planes along the left ventricular outflow tract (LVOT) view were obtained to cover the entire MV. Typical parameters are slice thickness: 3 mm with 0 mm gap; matrix size: 432×572 ; in-plane pixel size: $0.7 \times 0.7 \text{ mm}^2$; frame rate: 25 per cardiac cycle. Typical SA, 4C and 2C views of the ventricle were also acquired to provide additional geometrical information, such as the positions of papillary muscle cap points.

The MV was segmented in middle diastole when it is opened by using an in-house MATLAB (The MathWorks Inc., Natick, USA) code. The segmentation method is detailed in the work [15]. Briefly stated, the profiles of the anterior and posterior leaflets are manually segmented from the images in LVOT view (Fig. 6.1(a)). Two papillary attachment points were identified from the LVOT and SA cine images, as shown in Fig. 6.1(b). A uniform leaflet thickness of 1 mm was assumed and the physical position location that connects the MV leaflets and the ventricular wall was identified as the annulus ring, see in Fig. 6.1(c). We used the B-spline surface fitting in SolidWorks (Dassault Systèmes SolidWorks Corp., Waltham, MA, USA) for the three-dimensional reconstruction as shown in Fig. 6.1(d). In Fig. 6.1(e), a total of 16 evenly distributed primary chordae tendinae were assumed based on anatomical descriptions, with 10 associated with the posterior leaflet and 6 with the anterior leaflet. We assume that the chordae are attached to the free margin of the leaflets and run through from the leaflet tip to

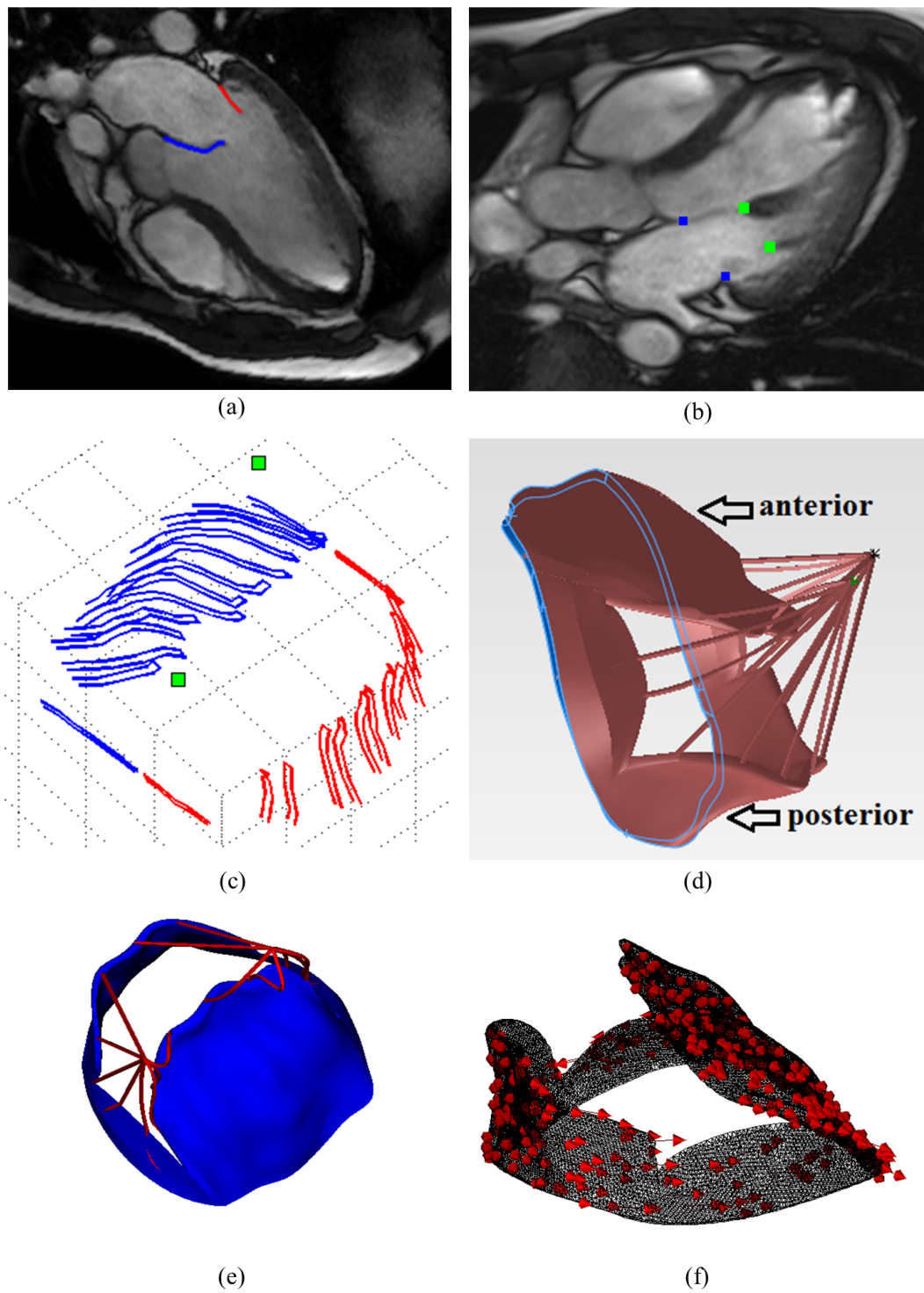


FIGURE 6.1: Procedure to reconstruct the MV geometry from MR images including (a) capture of anterior (blue) and posterior (red) profiles from LVOT images, (b) identification of papillary muscle cap points denoted by two green points, (c) assembly of the segmented curves to get the leaflet surface, reconstruction of the three-dimensional MV model with (d) a spatial annulus ring and (e) the ideal chordal architecture and (f) definition of the fibre structure for the anterior and posterior leaflets.

the annulus ring. This assumption is due to the lack of information from the MR images. For the same reason, we do not distinguish the marginal, strut and basal chordae. Each of the chordae is connected to one of the two papillary muscle heads, and each is assumed to have a uniform cross-sectional area of 0.16 mm^2 . The papillary heads are allowed to move towards the MV side during systole with displacements measured from the cine MR images. The embedded collagen fibres are defined along the circumferential direction (parallel to the annulus ring) for both the anterior and the posterior leaflets, as shown in Fig. 6.1(f).

6.2.2 Material models

The leaflets of the MV are modelled as an incompressible hyperelastic fibre-reinforced material, in which the SEF takes the form

$$\Psi_{\text{leaflet}} = c(I_1 - 3) + \frac{k_1}{2k_2} (\exp [k_2(I_4 - 1)^2] - 1) \quad (6.1)$$

where $I_4 = \mathbf{f} \cdot (\mathbb{C}\mathbf{f})$ is the square of stretch in the fibre direction and is only included in the SEF when $I_4 > 1$, and \mathbf{f} denotes the unit tangent to the fibre direction in the reference state.

The material parameters c , k_1 and k_2 are fitted to equal-biaxial *in vitro* tests on a healthy human MV carried out by [27] and are listed in Table 6.1.

TABLE 6.1: *Material parameter values for Ψ_{leaflet}*

	c (dyne/cm ²)	k_1 (dyne/cm ²)	k_2
Anterior leaflet	1.74×10^5	3.13×10^5	55.93
Posterior leaflet	1.02×10^5	5.00×10^5	63.48

Following our previous study in [176], we found that it is useful to employ a modified structural stress tensor \mathbb{P}_e defined as

$$\mathbb{P}_e = \left(\frac{\partial \Psi_{\text{leaflet}}}{\partial \mathbb{F}} \right)^{\text{T}} - 2c\mathbb{F}^{-\text{T}} + \beta_s \log(I_3)\mathbb{F}^{-\text{T}} \quad (6.2)$$

in which $\beta_s = 5.0 \times 10^6 \text{ dyne/cm}^2$. The pressure-like term $2c\mathbb{F}^{-\text{T}}$ ensures that when $\mathbb{F} = \mathbb{I}$, $\mathbb{P}_e = 0$. This reduces the pressure discontinuity in the Eulerian pressure field

and thereby reduces the magnitude of spurious volume loss at the fluid-solid interface. The term $\beta_s \log(I_3) \mathbb{F}^{-T}$ is a penalty term to reinforce the incompressibility constraint in the Lagrangian form, even though incompressibility is enforced globally in the Eulerian equations, the numerical interpolation of the Eulerian velocity to the solid region may not always yield a divergence-free discrete Lagrangian velocity field. This has been shown to yield more accurate stresses [176].

Although linear tetrahedral elements will yield volumetric locking for sufficiently large value of β_s , comparisons to the same MV model with $\beta_s = 0$ verified that for the value of β_s used here, we do not experience volumetric locking since the two models have comparable deformation under the same static loading.

The chordae are assumed to be isotropic and modelled as a Neo-Hookean material. In Eq. (2.7), c_1 takes the value of 1.8×10^8 dyne/cm² in systole, and 1.08×10^7 dyne/cm² in diastole. These values are based on the measurements of human MV chordae [177]. Similarly, the stress tensor \mathbb{P}_e for the chordae tendineae is defined as

$$\mathbb{P}_e = \left(\frac{\partial \Psi_{\text{chordae}}}{\partial \mathbb{F}} \right)^T - c_1 \mathbb{F}^{-T} + \beta_s \log(I_3) \mathbb{F}^{-T}. \quad (6.3)$$

6.2.3 Boundary conditions and numerical implementations

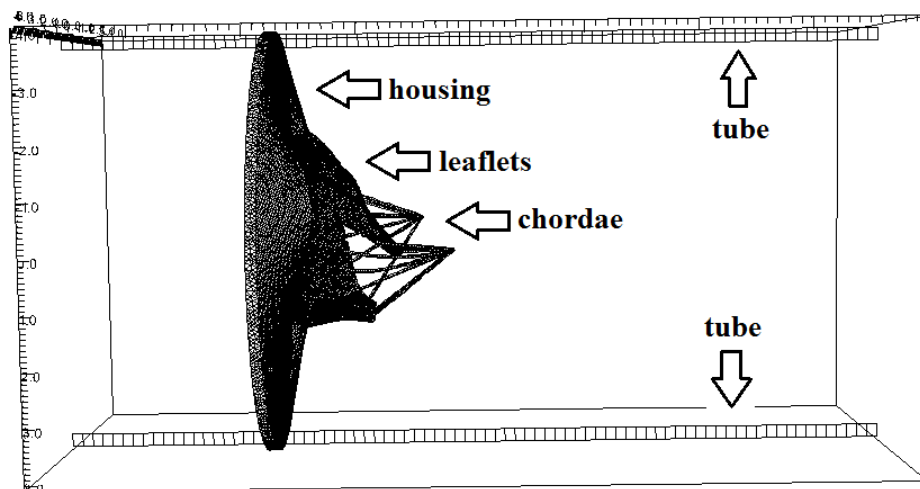


FIGURE 6.2: The saddle shaped mitral annulus is fixed to a non-planar rigid housing disc mounted to a semi-rigid circular tube of length 16 cm (not shown). The chordae are anchored to two papillary attachment points. These structures are all immersed in a cubic fluid box.

In the following simulations, we let $\rho = 1.0$ g/ml and $\mu = 4$ cP, and fix the MV annulus to a housing disc that is mounted in a semi-rigid circular tube immersed in a 10 cm×10 cm×16 cm fluid box (Fig. 6.2). The fluid box is discretized with spacings 0.125 cm×0.125 cm×0.1 cm, corresponding to a regular 80×80×160 Cartesian grid. In the numerical scheme, we use a standard four-point regularized version of the delta function in the Lagrangian-Eulerian interaction [144]. A time step size of 2.5×10^{-5} s is chosen in the explicit time-stepping scheme.

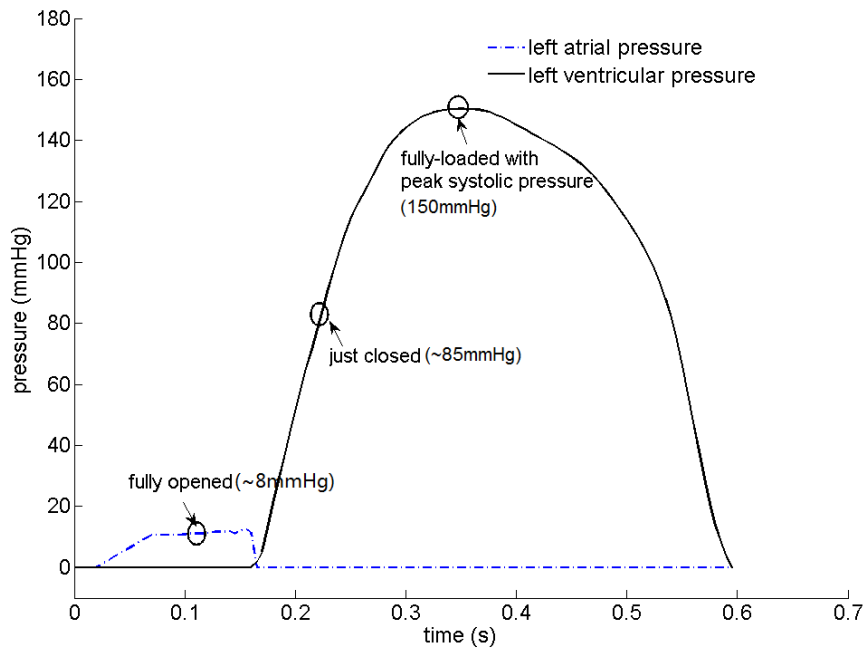


FIGURE 6.3: A typical human pressure profile, scaled to the subject-specific peak systolic pressure, as used in our simulations. Note that only the rapid diastolic filling and the systolic phases are modelled; see text for further discussion.

We specify the pressure difference between the inlet and outlet of the tube. Because subject-specific transvalvular pressure data are not available, we instead use a typical human physiological pressure profile rescaled to the subject’s cuff pressure, so that the peak systolic pressure is 150 mmHg[†], see Fig. 6.3. We do not model the LV here, so only the rapid filling phase of the diastole and the systolic phase can be modelled properly. This is because during the slow diastolic filling and atrial contraction, the transvalvular flow mostly results from the passive deformation of the LV. Without proper boundary conditions provided by the LV, these processes are hard to model. This is different

[†]Note that this subject’s blood pressure is slightly higher than the average.

from rapid filling, in which the transvalvular flow is due to the suction caused by the LV relaxation. In systole, the boundary conditions can also be easily approximated with the systolic pressure and the papillary muscle movement, as modelled in other studies [136]. The period of diastolic filling lasts around 0.2 s, during which 80% of transvalvular flow occurs [178]. Zero-pressure boundary conditions are applied along the remainder of the domain boundaries.

A grid independence study is performed with Cartesian grids of $80 \times 80 \times 160$, $96 \times 96 \times 198$, and $112 \times 112 \times 224$. The differences in structural maximum and average displacements of fully opened and fully loaded valves are all less than 5% for these three cases. For computational efficiency, we use the $80 \times 80 \times 160$ grid for all subsequent simulations.

6.3 Results

The fluid pressure fields from the IB/FE MV model are shown in Fig. 6.4 at three time instants indicated in Fig. 6.3; when the valve is fully opened ($t=0.1$ s), just closed ($t=0.22$ s), and fully loaded at the peak pressure of 150 mmHg ($t=0.35$ s). The valve opens at a driving pressure gradient of around 8 mmHg and withstands a significant physiological transvalvular pressure gradient when closed. The complete closure of the leaflets occurs at a transvalvular pressure gradient of around 85 mmHg, then undergoes minor further deformation before reaching the peak transvalvular pressure difference of 150 mmHg. Notice that our MV model has small gaps near the commissure area even in the fully closed state, and no flow leakage appears in the simulation.

The corresponding velocity fields are shown in Fig. 6.5, and indicate a strong jet flow towards the outlet (the LV side) when the MV opens. As the MV closes, there is a closing regurgitation across the MV, as shown in Fig. 6.5(b), which is responsible for the first heart sound. Figure 6.5(c) shows the velocity pattern when the pressure difference reaches its peak. An interesting view provided by the streamlines when the MV is fully opened is shown in Fig. 6.6. We can see that the flow is channelled by the two leaflets first, then the chordae act as the second orifice [179], and split the jet flow into three,

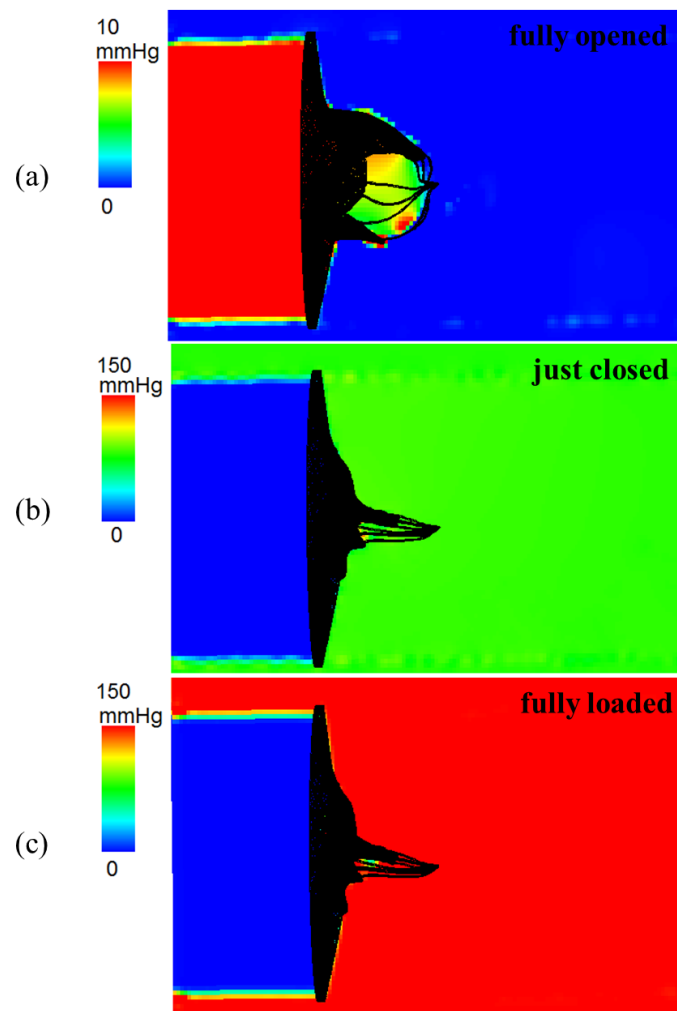


FIGURE 6.4: The in-plane view of the fluid pressure fields perpendicular to z -axis, when the MV is (a) fully opened, (b) just closed, and (c) fully loaded at the peak pressure.

with the main stream moving towards the LV apex, and side streams flowing towards the tube walls.

Fig. 6.7 gives the comparison of the deformed MV leaflets and the corresponding MR images in LVOT view. Qualitatively, the opening and closing configurations of the simulated MV show good agreement with the MR measurements. However, there is evidence of some discrepancy, particularly in the anterior leaflet when fully closed: the modelled MV is bulged into the left atrium, in contrast to that of the corresponding MR image (Fig. 6.7(c)). This is presumably due to the simplified assumption of the chordae structure, or the lack of strut chordae.

The flow rate through the valve orifice is shown in Fig. 6.8, along with the measured flow

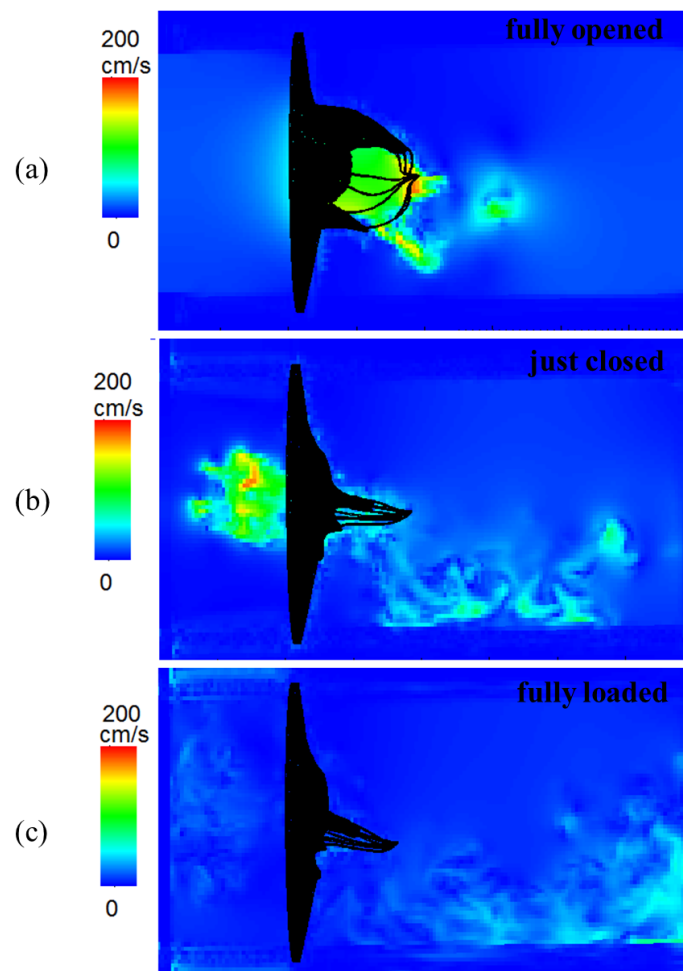


FIGURE 6.5: The fluid velocity fields at the three time instants, corresponding to the ones in Fig. 6.4.

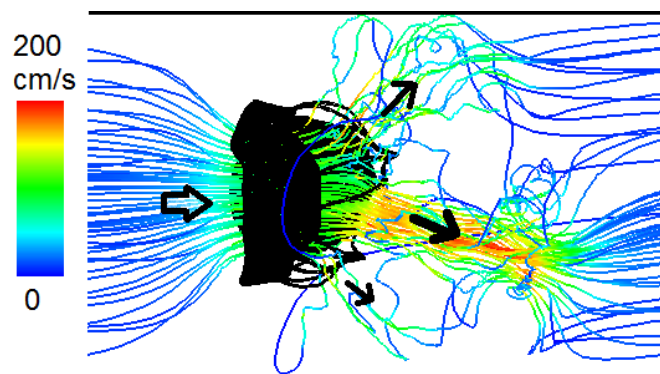


FIGURE 6.6: Instantaneous streamlines when the MV is fully opened.

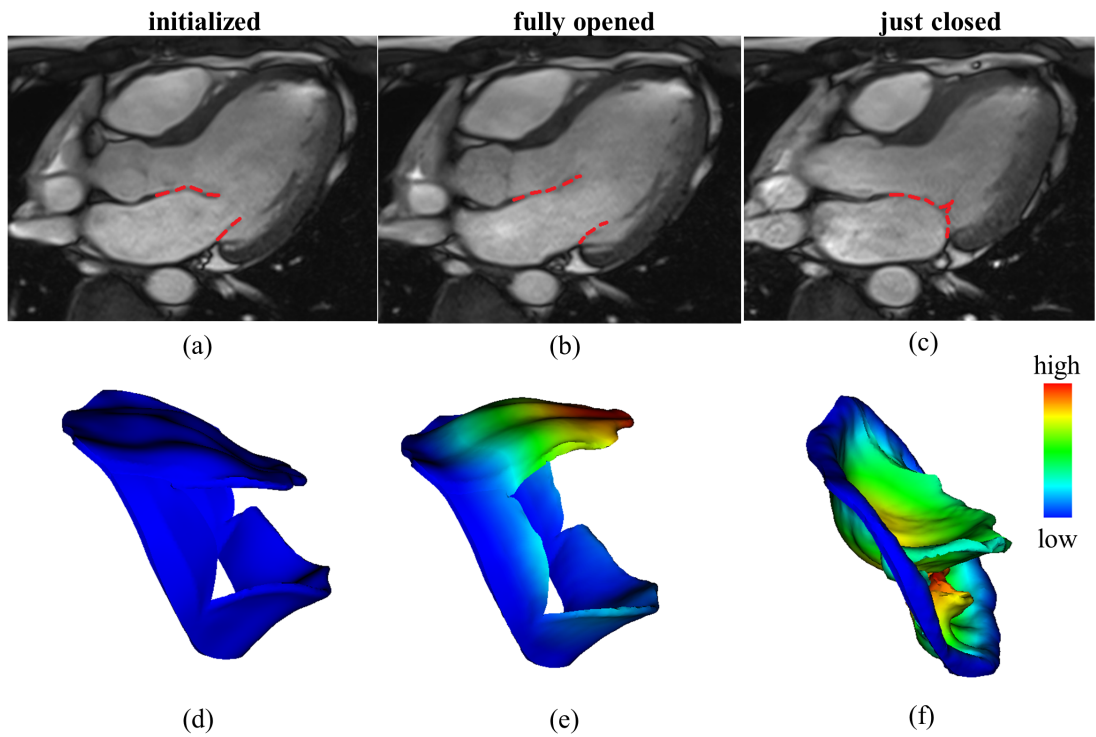


FIGURE 6.7: Cine MR images showing the MV shapes (a) at the beginning of the simulation (middle diastole), (b) when fully opened, and (c) just closed. The corresponding MV model predictions are shown in (d, e, f), coloured by displacement.

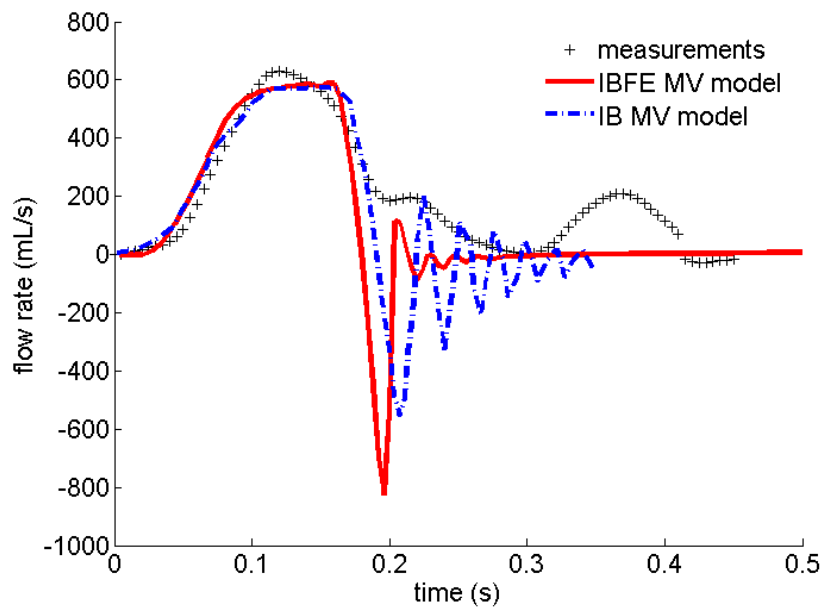


FIGURE 6.8: Flow rate comparison among the predictions of the IB/FE model, the previous IB model [15], and the measurements obtained from the cine MR scan. Note again that only the time period in rapid filling of diastole lasting for 0.2 s can be properly modelled.

rate obtained from phase contrast MR measurements, as well as the one from the IB fibre-networked MV model [15]. When the MV is opened, the flow rates from both the IB and IB/FE MV models are comparable to the measured data, with slightly lower peak value. However, the IB/FE model seems to predict a slightly higher regurgitation closing flow (10.8 mL vs 9.4 mL), followed by much smaller oscillations compared with the IB model. Furthermore, we plot the stress and strain distributions along the fibre direction

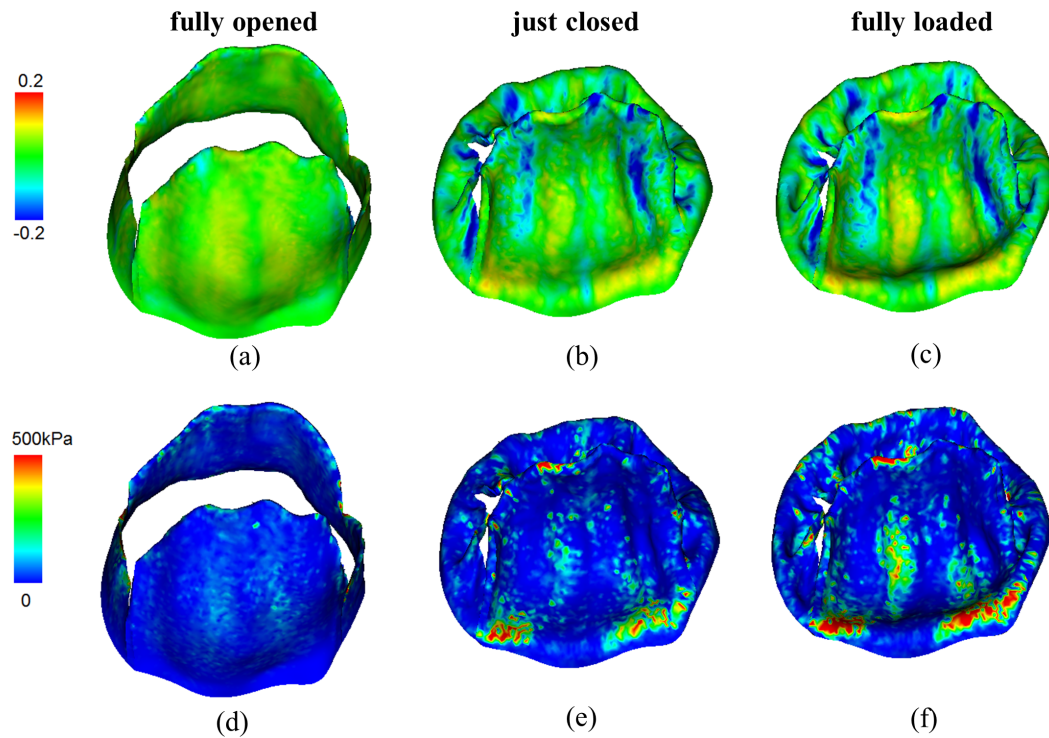


FIGURE 6.9: The fibre strain when the MV is (a) fully opened, (b) just closed, and (c) fully loaded. The corresponding fibre stress distributions are shown in (d-f), respectively, the stress values are capped at a peak stress of 500 kPa to avoid unrealistic high stress concentrations at the chordal insertion areas.

in Fig. 6.9. When the MV is fully opened, majority of the leaflet belly is stretched along the fibre direction, and the stress level is low. Immediately after the MV is closed, high stress concentration occurs in the two fibrous trigones of the anterior leaflet as well as along the valvular ring. Towards the commissures, there exist compressive stresses, particularly in the neighbourhood of the wrinkles. When approaching the highest systolic pressure (fully loaded state), the strain and stress patterns are similar to the ones when the MV is just closed, but the high stress area increases, which is most visible in the belly and along the annular ring.

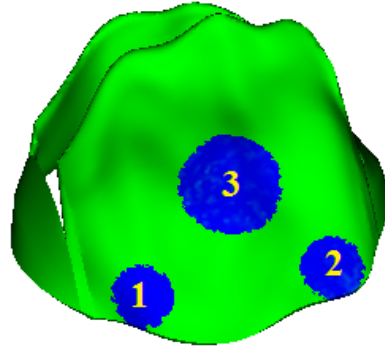


FIGURE 6.10: Three local regions in the anterior leaflet are selected for quantitative stress analysis.

We select three local regions in the anterior leaflet for quantitative stress and strain analysis. These include two trigones and one belly region illuminated in Fig. 6.10. The average stress and strain of these regions are summarized in Table 6.2. We can see that when the MV is fully opened, the fibres of the belly region are stretched as indicated by the positive strain, and the stress is higher compared to the trigone regions. Immediately after the MV has closed, the stresses increase in all regions; however, at this point, the two trigones experience higher stress levels compared to the belly region. This pattern remains the same when the MV experiences the peak systolic pressure load, though the stresses are nearly doubled.

Regions number	Stress along fibre directions (kPa)			Strain along fibre directions		
	Fully opened	Just closed	Fully loaded	Fully opened	Just closed	Fully loaded
1	-2.9	92	193	-0.004	0.04	0.04
2	-0.8	72	144	-0.004	0.02	0.02
3	17	79	142	0.04	0.02	0.02

TABLE 6.2: Average regional stresses and strains along the fibre direction on the three local regions defined in Fig. 6.10, again when the MV is fully opened, just closed, and fully loaded.

The effect of the chordae tendineae structure is demonstrated in Fig. 6.11. When the MV is fully opened, the orifice of the model without chordae is larger than the one with chordae. This gives rise to a maximum inflow rates of 871 mL/s (without chordae) and 588 mL/s (with chordae). The no chordae MV begins to close and at some point in systole, the simulation fails due to excessive distortions. The deformed MV structure

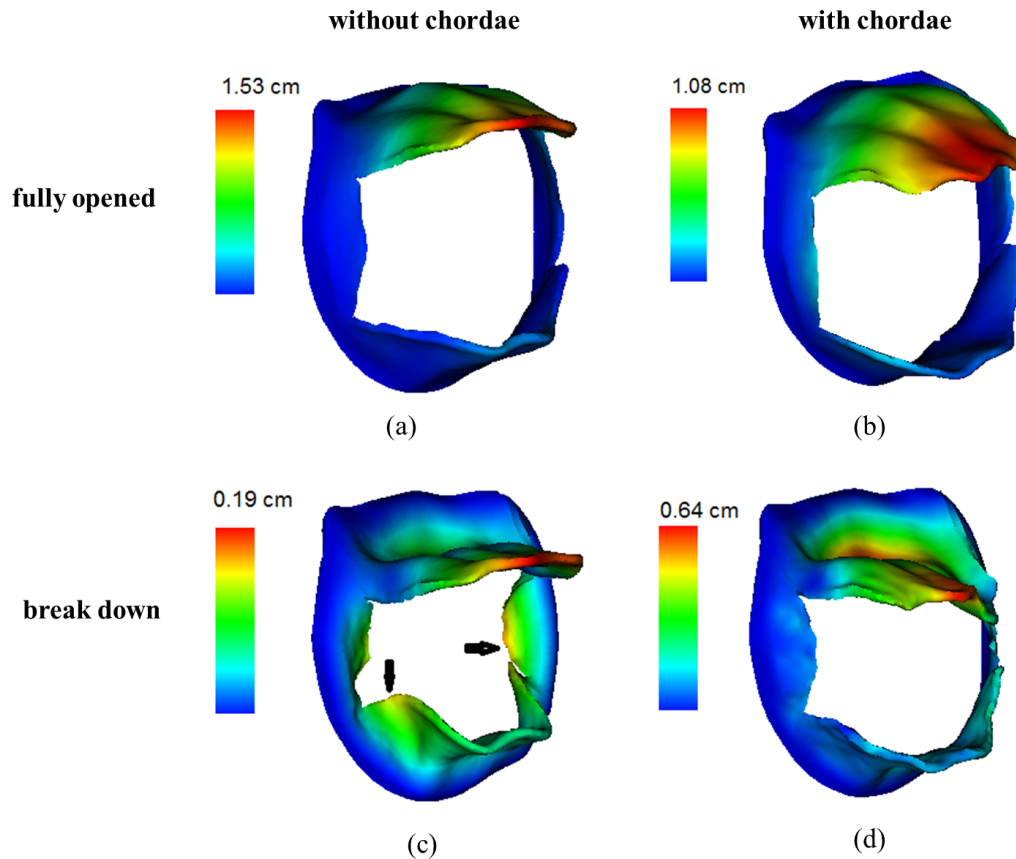


FIGURE 6.11: Deformed MV models (a) without chordae, and (b) with chordae at the time when the MVs are fully opened. The corresponding deformations right before the models (c) without chordae, and (d) with chordae break down, respectively. The black arrows in (c) indicate the prolapse regions.

right before abortion is presented in Fig. 6.11(c). The corresponding MV configuration with chordal structure is given in Fig. 6.11(d). Clearly, the chordal structure plays an important role in the MV dynamics: it serves as a secondary orifice in diastole, and helps the thin leaflets from over prolapse in systole. We also investigate the average chordae tendineae tension when the MV is fully loaded at the maximum systolic pressure of 150 mmHg. The average force for the 6 chordae associated with the anterior leaflet is 0.68 ± 0.31 N, which is substantially higher than that for the 10 chordae with the posterior leaflet valued 0.23 ± 0.15 N. The tensions in the two papillary muscle groups are 3.0 N and 3.34 N, respectively. These tensions experienced by the chordae and the papillary muscles are comparable with values from other studies [180, 181].

6.4 Discussion

In this chapter, we develop an IB/FE model of a human MV using *in vivo* MR image-based anatomy and fibre-reinforced hyperelastic laws. This approach allows us to analyse the stress and strain patterns in the MV leaflets with experimentally determined constitutive parameters. This is not possible in the previous IB model [15]. The model is validated by comparing the computed opening and closing configurations, as well as the flow rate, to the subject-specific clinical measurements.

Compared to the previous work [15], significant improvements are incorporated in the current IB/FE MV model, namely, (1) the MV leaflets are described with a continuum mechanics framework; (2) transversely isotropic constitutive laws are used for the MV leaflets, instead of a fibre-like characterization; (3) the annulus ring is reconstructed from clinical images, not an assumed planar elliptic shape; (4) detailed finite stress/strain fields are presented, which are not available in the previous IB model.

Using the cine images, MV leaflet delineation is most clearly defined in diastole when the transvalvular pressure difference is minimal because the influence from blood flow is small [182], and the MV is in an opening state. By sewing miniature markers onto the MV leaflets of 57 sheep, Rausch et al. [183] calculated the *in vivo* strain in these anterior leaflets; using different reference states they found that the strain as well as strain rate, however, is nearly insensitive to the choice of the reference configuration. With this in mind, we reconstruct the MV structure in middle diastole. And because the transvalvular pressure difference is minimal, this is also close to the zero loading state. In addition, we keep the mitral annulus fixed in space, but allow the papillary muscles to move towards the leaflets during systole with a maximum displacement measured from cine images. By doing this, the leaflets are allowed to close when subjected to a physiological pressure load, as discovered before [174, 184].

From Fig. 6.9, it is clear that the strains along the fibre direction are tensile for most of the regions in the anterior leaflet throughout the cardiac cycle, but there are still some regions that are compressed during closing. Similar results have been reported in [2, 185]. Our model prediction of the fibre strain seems to agree well with the *in vivo*

measurements, for example, Rausch et al. [183] measured the peak *in vivo* circumferential strain in the belly region of the anterior leaflet, which is $3.5 \pm 3.6\%$. By defining a circular region with 0.5 cm radius in the belly region of the anterior leaflets, the average strain along fibre direction from our IB/FE model is $3.6 \pm 4.0\%$, which is comparable to Rausch's results, and lies close to the range reported by Sacks et al. [186] from *in vivo* studies (2.5-3.3%).

On the other hand, mitral leaflet strain estimated from some *in vitro* measurements seem to be higher than our predictions. Jimenez et al. [187] measured the strain in the centre of a porcine anterior leaflet using a left heart simulator, and they found that their peak circumferential strain is $11 \pm 4.9\%$ in the normal annular configuration. Similar peak circumferential strain (10%) in the centre of the leaflet was also reported in *in vitro* studies by Sacks et al. [188] and He et al. [181, 189], although the range of the peak circumferential strain can be as low as 2%[†]. The difference in strain between the *in vivo* and *in vitro* measurements was also noted by Rausch et al. [183]. It is not clear if the difference is due to the species difference among the porcine (in the *in vitro* studies), ovine (in the *in vivo* studies), and human valves (in our study), or by the incapability of *in vitro* models to accurately reproduce the mechanical and hemodynamic environment of the MV in terms of the material property, boundary condition and the initial geometry. We also note again that the peak systolic pressure of 150 mmHg used in the simulation is higher than a typical value of 100-140 mmHg.

The peak average stress along the fibre direction in the belly region is 142 kPa, and 193 kPa, 144 kPa for the two fibrous trigons (see Table 6.2). These predicted stress levels are of similar order to results of other published MV models [2, 29]. Jimenez et al. [190] also measured different types of chordal systolic tension and the forces experienced by the papillary muscles in their *in vitro* experiments. They reported the peak systolic tension of 0.95 ± 0.35 N in the anterior strut chordae and of 0.35 ± 0.16 N in the anterior marginal chordae. The average tension in the anterior chordae in our model is 0.68 ± 0.31 N, which is comparable with the range being reported [175, 190]. The maximum papillary muscle

[†]within one standard deviation

forces are found to be 4.3 N and 4.6 N again from [190], and 4.51 N and 5.17 N from Wang's model [175]. These are also comparable with our predictions of 3.0 N and 3.34 N.

Although our results are in good agreement with the cine image observation and the measured flow rate, several model limitations are worth mentioning. For example, the simulated anterior leaflet appears to bulge into the left atrium, in contrast to that of the cine MR image. Also, there are small gaps in the commissure areas when the valve is fully closed. This is due to the difficulty of reconstructing the subvalvular apparatus accurately from the images, especially for the commissure areas and chordae tendineae. We have to build these relying on anatomical descriptions widely adopted in other studies [15, 152, 153, 169, 191]. More accurate geometry reconstruction may be possible using CT images. For example, Wang and Sun [175] reconstructed the MV models with chordal origins, insertion points by using multi-slices CT images. However, as pointed out in Section 1.3, CT scans may not be applicable to the healthy volunteer due to the radiation risk. Real time three-dimensional echocardiography could be another promising way to obtain detailed MV structure either non-invasively or with limited invasiveness [191], though the reproducibility is not as good as CT and MR techniques. Current *in vivo* MR images are not able to quantify the fibre directions in the dynamic MV leaflets, therefore their distributions are usually modelled using 'rule-based' methods [2, 15, 151, 169, 191], following experimental observations [149]. Recently, Lee et al. [192] developed a micro-anatomical MV models from *in vitro* experimental measurements by mapping the measured collagen fibre architecture using small light scattering techniques to the MV models from the same ovine MV leaflets. Non-invasive methods are needed to quantify the *in vivo* fibre architecture.

Moreover, instead of separating the marginal, basal and strut chordae which have various mechanical responses, we have now only used simplified primary chordae inserting into the leaflets from the free edge, following previous works [15, 173, 174]. This may be partially responsible for the MV bulging towards the left atrium. We further model the chordae simply as isotropic *neo-Hookean* materials having higher stiffness in systole and becoming much softer in diastole. This is because in diastole when the MV opens, the chordae are usually compressed and act as an isotropic material as the collagen fibres

are deactivated. On the contrary, in systole, the collagen fibres embedded are mostly being stretched, so a higher chordal stiffness is presented. However, chordae are actually bundles of collagen fibres, and an anisotropic hyperelastic constitutive law should be more accurate to describe their elasticity [151, 175]. Overall, this is a simplified model of the chordal structure that has reproduced the measured *in vivo* dynamics of MV. With new developments in clinical imaging it may be possible to model more detailed patient-specific chordal structures and their effects on the MV behaviour in the near future.

Finally, our initial configuration is half opened, and it is generally very difficult to fully close an opened complex MV configuration that is not initially driven from a fully closed state. Inaccurate geometric details in the commissure areas may also be responsible. It is a possible reason that the flows around the MV are not completely physiologically realistic due to the absence of the left ventricle.

6.5 Conclusion

We have developed a new human MV model using a hybrid IB/FE approach, which combines FSI simulations with cine MR image-derived geometry reconstruction and a transversely isotropic, hyperelastic constitutive model. This model is a significant enhancement from our previous work, because it provides dynamic stress distributions, which are found to be concentrated in the annulus trigones and the belly of the anterior leaflet. The results agree well with the opening and closing leaflet configurations and with the flow rate, estimated from the MR measurements. Although there are still some discrepancies between the model predictions and *in vivo* observation, with improved imaging technique and further work, it is possible to develop more realistic MV models that could be applied to study MV diseases.

Chapter 7

Fluid-structure interaction model of human mitral valve within left ventricle

In this chapter, we will present an integrated model of mitral valve (MV) coupled with the left ventricle (LV) so that the MV-LV interaction can be taken into account. This model is compared with a corresponding MV-tube model described in Chapter 6, and differences in the results are discussed. The majority of this work is included in the series of *Functional Imaging and Modeling of the Heart* [16].

7.1 Introduction

Moderate or severe MV dysfunction remains a major medical problem and is usually caused by leaflet prolapse or is secondary to left ventricular disease [193]. It is believed that computational studies of the MV mechanics as well as its coupled functioning with LV have the potential to enhance our understanding of the valvular-ventricular interaction, which will lead to successful MV repair and replacement.

Research on developing biomechanical MV models dates back to the 1990s [194], employing finite strain deformational kinematics, including realistic anatomical geometries and

hyperelastic constitutive models [175, 195, 196]. However, a purely structural analysis is usually applied to a statically or dynamically pressurized closed valve in an isolated situation [197]. We know that the major function of the MV is to guide the blood to flow only from the left atrium to the LV; additionally, the structure of the MV is closely tied to the LV through the chordal connection. In this sense, to understand the full MV mechanism, it is very important to simulate the dynamics of MV with inclusion of the LV dynamics, as well as the FSI among the MV, LV and the blood.

FSI model simulating native mitral function was initiated by Kunzelman et al. [2, 170, 171]. More recently, there have been a number of FSI valvular models [15, 135, 148, 174], for example, the model presented in Chapter 6 using IB methods. However, the effect of LV dynamics is not included in these studies, and thus the flow field is not physiologically realistic. Indeed, Lau et al. [198] compared the MV dynamics in a straight tube and a ventricular-shaped fluid domain, and they found that when the MV is mounted into a LV, the transvalvular velocity is slower, associated with increased fluid vorticity compared to the one estimated in a tubular geometry. Yin et al. [184] investigated a chordaed MV inside a LV and identified fluid vortices associated with the LV motion. They found that a dynamic LV has a large impact on the fluid flow and valve tissue deformations. However, their LV motion is modelled as a set of prescribed moving boundary, and the MV model is simply constructed using a network of linear elastic fibres. Using a simplified two-dimensional rigid MV model together with the left atrium and ventricle, Dahl et al. [199] studied the MV behaviour during the diastolic filling, and concluded that the asymmetric leaflet geometry is important for accurately predicting the MV flow pattern, though the imposed LV wall movement was obtained from ultrasound recordings. Chandran and Kim [200] recently reported prototype FSI MV dynamics in a simplified LV chamber model using an immersed interface-like approach. To date, there has been no work reported that properly includes both the three-dimensional MV-LV interaction and FSI.

In this chapter, we have developed a preliminary fully integrated MV-LV model, which is image-derived and simulated using again the IB/FE method. We will also compare the differences of the MV dynamics when the MV is mounted in a LV and a tube .

7.2 Model settings

7.2.1 Geometry models of MV and LV

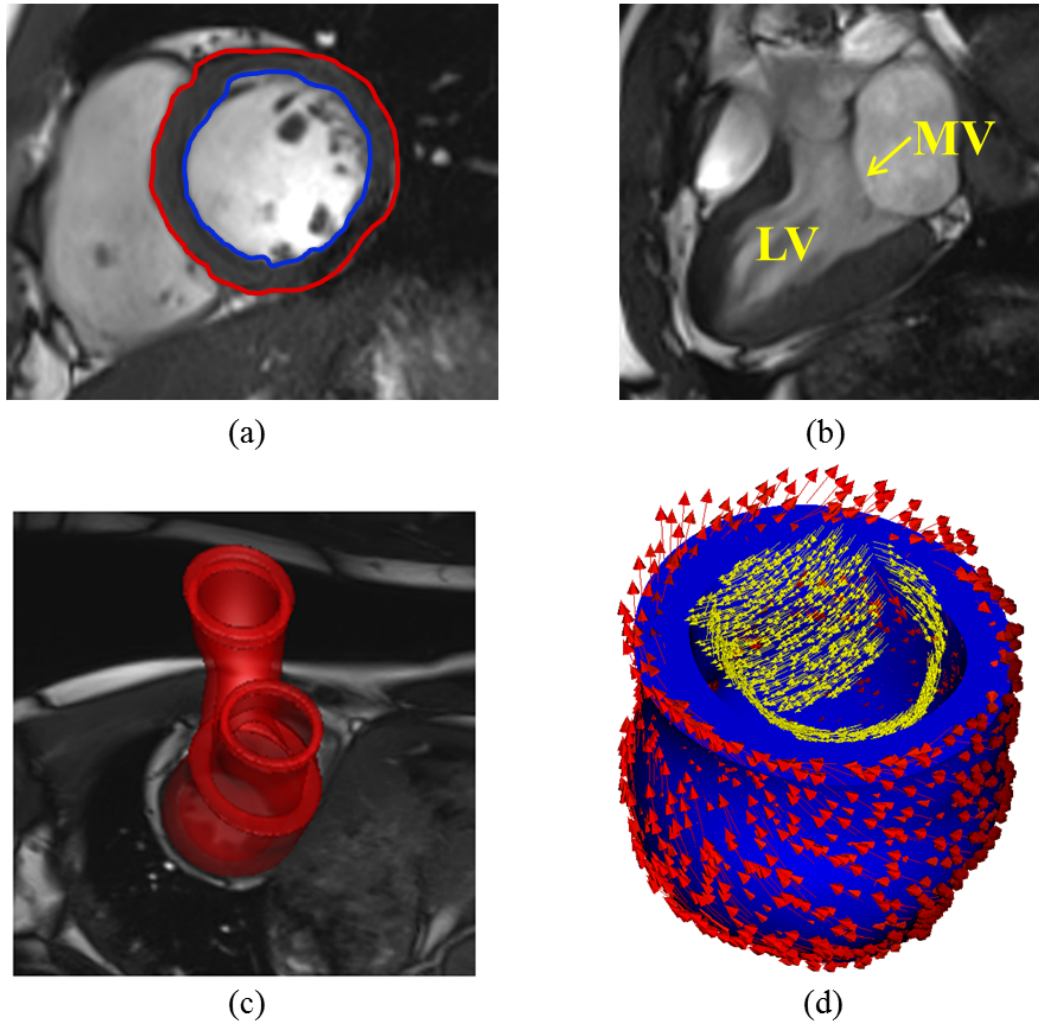


FIGURE 7.1: (a) The short-axis view gives one extraction of LV wall boundary; (b) the long-axis view provides the positional information of MV and LV; (c) the rebuilt LV geometry superimposed on one MR image and (d) the fibre architecture of MV and LV are depicted.

We adopt the same subject-specific MV geometry, following the procedure described in Section 6.2.1. The LV geometry is reconstructed from the cine MR images performed on the same volunteer, details can be found in [201, 202]. Summarized in Fig. 7.1, we extract the contours from 7 slices in SA views in early diastole (immediately before the MV opens when the LV pressure is lowest [202]), which record the information of ventricular wall boundary from the LV base to the apex. Two artificial inflow and outflow tracts are

extended at the top of the LV chamber to apply flow boundary conditions. The fibre construction of myocardium follows the rule-based method detailed in [203], defined as from the endocardium to the epicardium, the fibre direction linearly rotates from -60° to $+60^\circ$ and the sheet direction from -45° to $+45^\circ$, with respect to the throughwall direction.

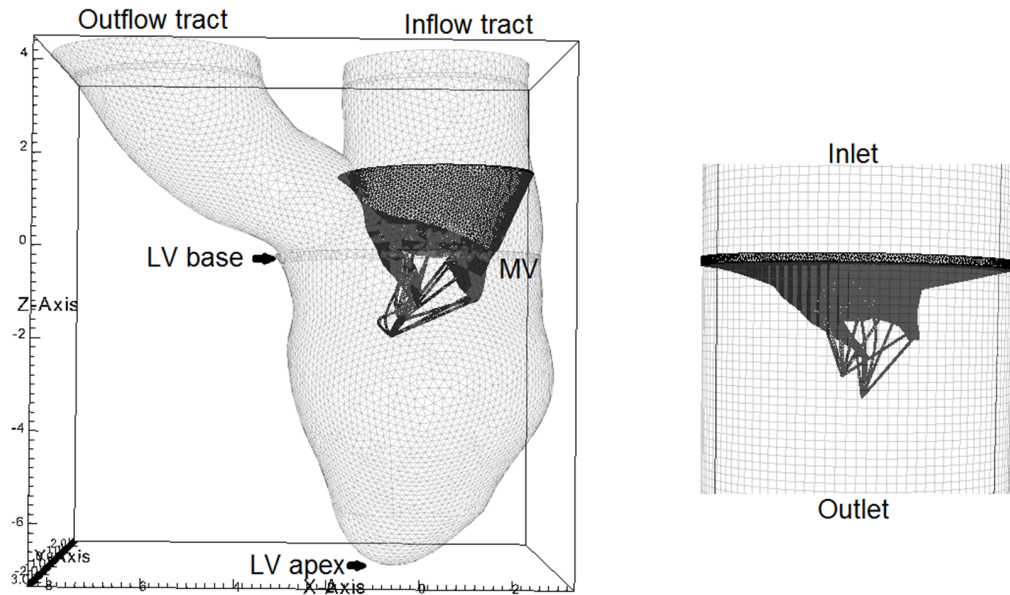


FIGURE 7.2: The sketches of (a) the MRI-derived MV-LV model, and (b) the MV-tube model, adopted from [16].

The MV is mounted to the inflow tract of the elastic LV based on the relative positions derived from the MR images. This forms the integrated MV-LV model. To conduct the comparison, the MV is also fixed to a housing disc and mounted to a outer tube, following the work in Chapter 6; this forms the MV-tube model. Both model settings are plotted in Fig. 7.2. The chordae are not directly attached to the LV wall, but modelled similarly as in Chapter 6.

7.2.2 Material models of MV and LV

We again adopt the MV material model in Section 6.2.2. However, due to the self-excited mechanism of the LV wall, the passive and active contributions are both considered for myocardium, as in [202]. The myocardium is considered to be incompressible, hence the

first PK stress in the LV is

$$\mathbb{P}_e = \mathbb{P}_p + \mathbb{P}_a,$$

where \mathbb{P}_p corresponds to the passive stress and is derived similarly from Eq. (6.2). The fibre-reinforced SEF for myocardial response is introduced by [45] via

$$\begin{aligned} \Psi_{\text{myocardium}} = & \frac{a}{2b} \exp[b(I_1 - 3 - 2\log(J))] \\ & + \sum_{i=4,6} \frac{a_i}{2b_i} \{ \exp[b_i(I_i - 1)^2] - 1 \} + \frac{a_{fs}}{2b_{fs}} \{ \exp[b_{fs}(I_8)^2] - 1 \}. \end{aligned} \quad (7.1)$$

I_4 , I_6 and I_8 are the invariants accounting for the passive fibre, sheet and the shear properties. Analogous to Eq. (6.1), I_4 and I_6 terms are only presented when the fibres are in states of extension.

The exclusive active stress tensor \mathbb{P}_a for myocardium is defined by

$$\mathbb{P}_a = JFT^s T \mathbf{f} \otimes \mathbf{f},$$

where \mathbf{f} is the fibre direction in the deformed configuration. T is a function determined from the work done by Niederer et al. [204]. The constant scalar T^s enables us to produce real systolic dynamics.

7.2.3 Loading conditions

Simulations of the MV-LV and MV-tube models are conducted using the open-source IBAMR software framework. The MV-tube model is identical to the one built in Chapter 6. In the MV-LV model, the structure below LV base is contractile, the regions above the LV, including the MV and its apparatus, are assumed to only bear the passive load. The LV base is allowed to have radial expansion, but to be fixed in the axial and circumferential directions. During diastole, zero flow boundary condition is imposed in the outflow tract. The pressure, linearly ramped to the end-diastolic pressure (assumed to be 8 mmHg), is applied in the inflow tract at 0.8 s. After the end of the diastole, the LV region simultaneously contracts, triggered by a spatially homogeneous intracellular calcium transient [201].

The increased LV pressure closes the MV and opens the aortic valve when the LV pressure exceeds the diastolic aortic pressure, which is assumed to be the measured diastolic cuff pressure of 85 mmHg from the healthy volunteer. Because the aortic valve is not included in the MV-LV model, the aortic tract is either completely open or completely closed, determined by the pressure difference between the aorta and inside LV. During the systolic ejection, a three-element Windkessel model [135] is connected to the outflow tract to provide a physiological pressure-flow boundary condition; the systolic phase ends when the LV no longer pumps blood out. The end-diastolic pressure of 8 mmHg is maintained in the inflow tract till the end of the systole.

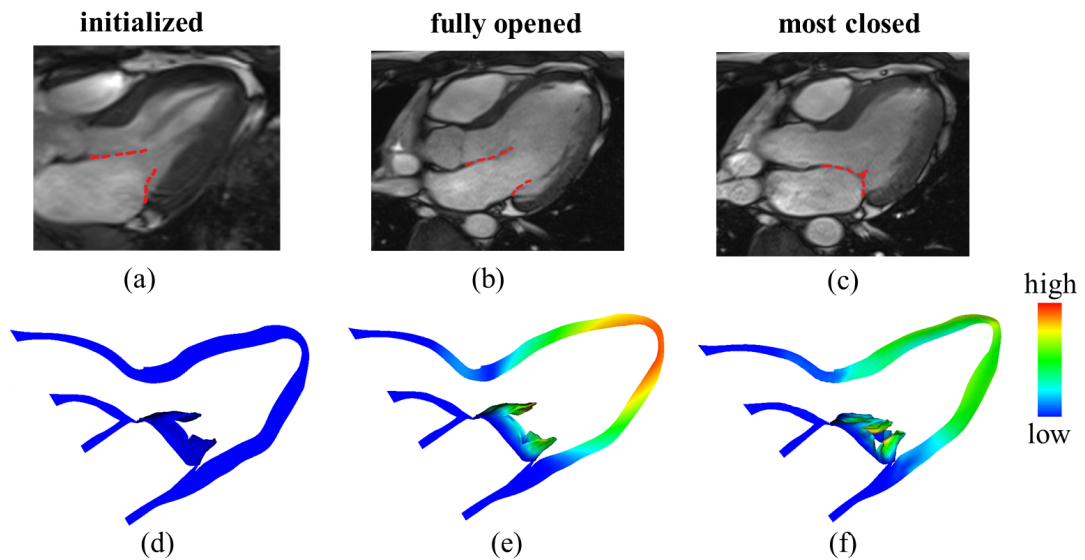


FIGURE 7.3: Cine MR images showing the MV and LV deformations (a) at the beginning of the simulation, (b) when MV is fully opened, and (c) most closed. The corresponding simulated results are given in (d, e, f), coloured by displacement

7.3 Results

The comparison of the deformed MV, LV configurations and the corresponding MR images in LVOT view are presented in Fig. 7.3. Generally, the opening and closing configurations of the simulated structures show an agreement with the MR measurements, though in the most closed state, there exists a clear orifice between the two MV leaflets.

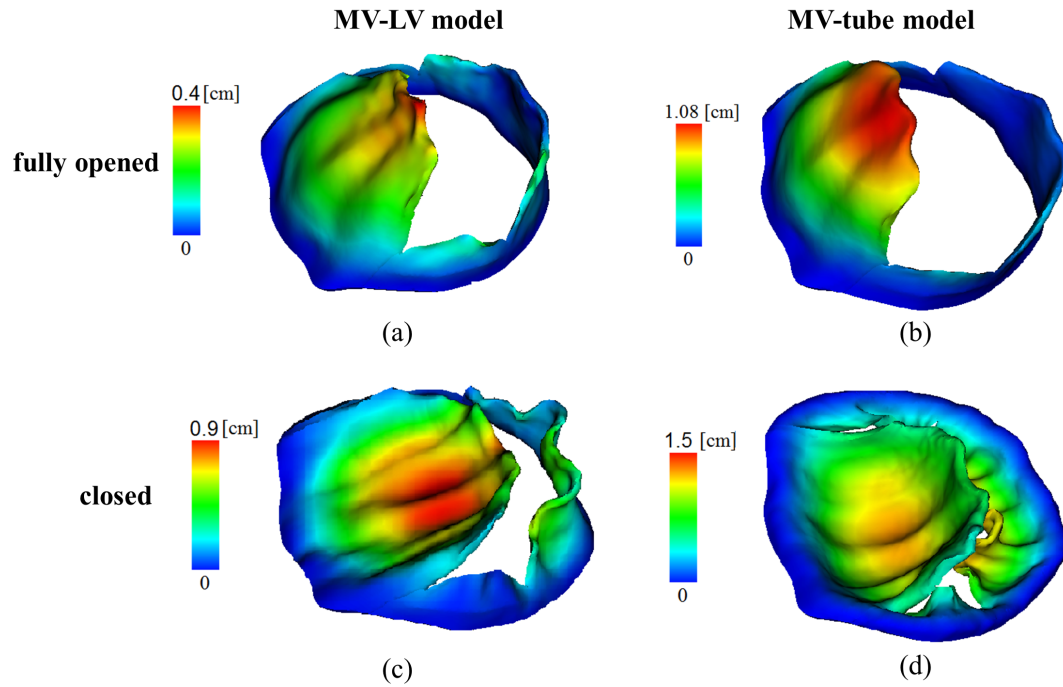


FIGURE 7.4: The fully opened MV in (a) the MV-LV model, (b) the MV-tube model (b). The most closed MV in (c) the MV-LV model, and (d) the MV-tube model. Coloured by the displacement.

To give more comprehensive comparison between the MV-LV and MV-tube models, we further obtain the MV deformations from these two models, depicted in Fig. 7.4. Because of the increased pressure in the inflow tract during diastole, the volumetric flow rate across the MV linearly increases until end of diastole, with a maximum value of 90 mL/s. The total inflow volume across the MV in diastole is 40 mL, which is less than the real cardiac output (around 80 mL). Fig. 7.4(a) and (b) show the deformed MV leaflets of the two models when the MV is fully opened. We can see that the orifice in the MV-LV model is smaller, which suggests that the LV wall provides more resistance to the blood flow that fills the LV cavity during the MV opening. This does not happen in the MV-tube model; hence for the same pressure drop, the flow rate is greater.

About 0.8 s later, the LV starts to generate active tension, and ejects the blood through the outflow tract. The closing regurgitation flow across the MV is estimated to be 7.2 mL. When the LV starts to eject blood, we notice that the MV in the MV-LV model is partially closed, compared to that of the MV-tube model, see in Fig. 7.4(c) and (d). The MV regurgitation in the MV-LV model persists in systole, which prevents the

ventricular pressure to increase efficiently. The peak pressure is 117 mmHg, which is much less than the peak value of 150 mmHg, corresponding to no leaking at the inflow tract in systole.

Fig. 7.5 shows, respectively, the streamlines in the MV-LV model during the early diastolic filling, the late diastolic filling, when the MV is closing, and when the LV is ejecting blood through the outflow tract. The corresponding streamlines of the MV-tube model are shown in Fig. 7.6. In the MV-LV model, the flow moves directly towards the LV apex in the early filling (Fig. 7.6(a)), forming large vortices in the late diastolic filling in the whole LV cavity, mixing the fresh blood from left atrium with the remaining blood from the previous heart beat (Fig. 7.6(b)). These features are nearly absent in the MV-tube model. Again, we note some leaking appearing in Fig. 7.5(d) as the MV is not closed completely.

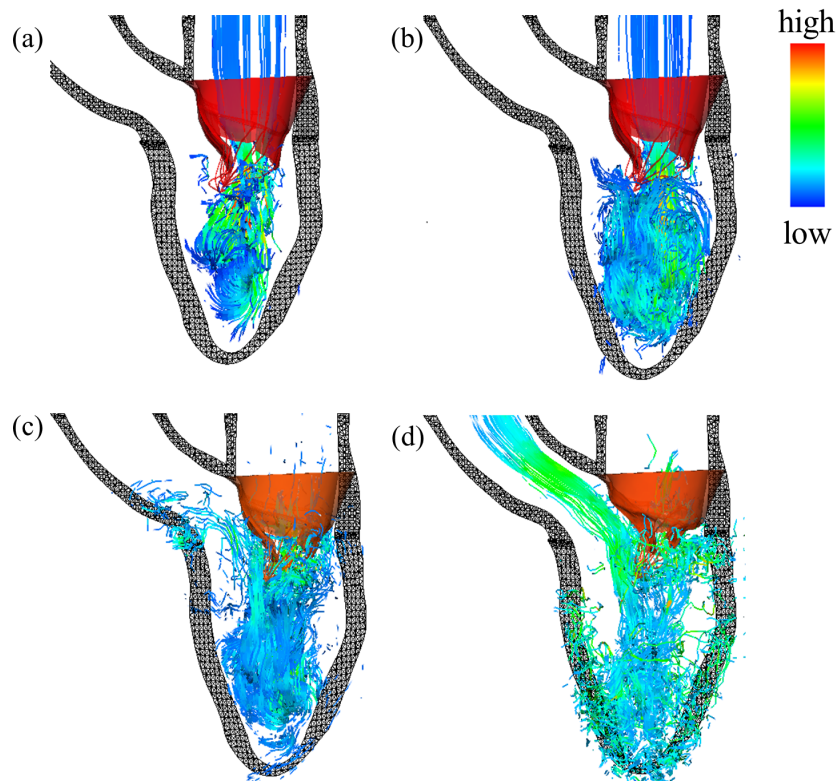


FIGURE 7.5: Streamlines in the MV-LV model (a) in the early diastolic filling, (b) in the late diastolic filling, (c) when the MV is closing and (d) at the middle of the systolic ejection. Coloured by the velocity magnitude and adapted from [16].

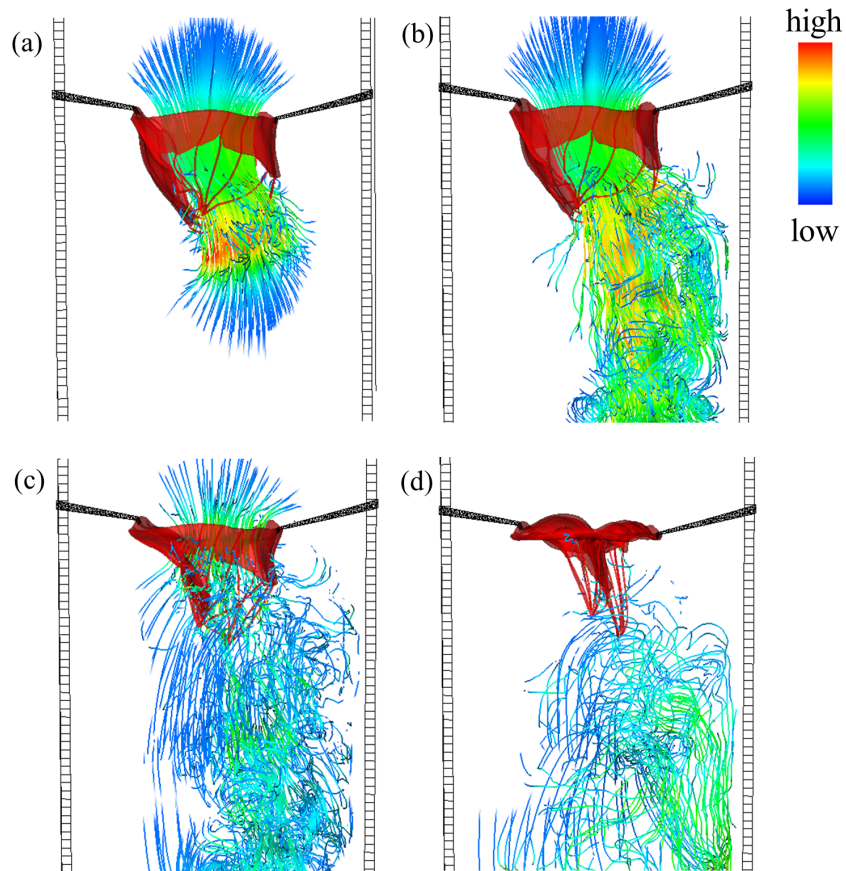


FIGURE 7.6: Streamlines in the MV-tube model (a) in the early diastolic filling, (b) at the late diastolic filling, (c) when the MV is closing and (d) when the MV is fully closed. Coloured by the velocity magnitude and adapted from [16].

The flow patterns become much more complex with inclusion of MV in LV, especially in the diastolic phase, given in Fig. 7.7. The flow jet, for example, is affected by the existence of MV leaflets and chordae, typically in the late diastole. In Fig. 7.8, the vortex dynamics is presented in the LVOT front view in the absence of MV at middle systole. However, if the MV is included, the vortex dynamics changes, with vortices appearing in different locations; instead, we can see it in the back view with the same direction of rotation.

7.4 Discussion and Conclusion

In this chapter, we have built an integrated MV-LV model based on *in vivo* cine MR images of a healthy volunteer. This model incorporates an elastic MV, a contractile LV

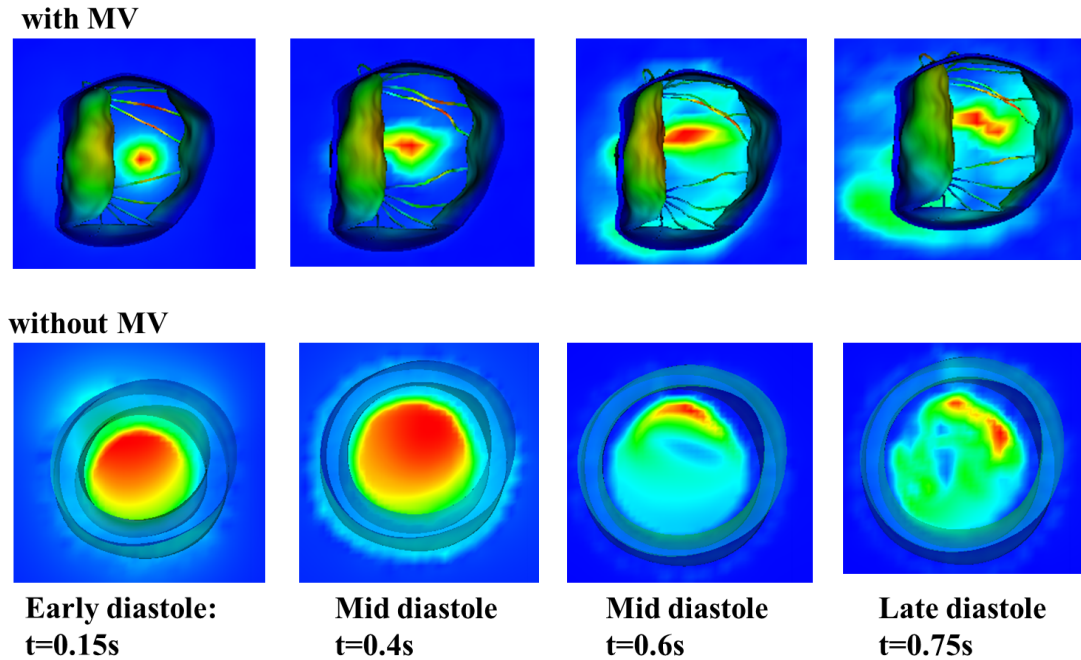


FIGURE 7.7: The comparison of the flow patterns in LV between the models with and without the MV structure at different time points in diastole. The colour shows the magnitude of velocity.

and the FSI for the first time.

Results are compared with that of a corresponding MV-tube model, and a number of differences are pointed out. First, the flow patterns are very different in the MV-LV model. When the MV is opened, the blood passes through the MV and directs to the posterior leaflet side in the MV-tube model before hitting the tubular wall. However, in the MV-LV model, the flow goes directly towards the LV apex, and then rebounds toward LV base to form large vortices.

During diastole, the MV-LV model seems to produce a smaller opening configuration compared to the corresponding MV-tube model. This is because of the extra resistance offered by the LV wall, which is absent in the MV-tube model. Consequently, the total inflow volume through the MV is reduced. We know that the diastolic phase is normally divided into three phases—the rapid filling, the slow filling and the atrial contraction. In the rapid filling, the transvalvular flow results from the relaxation of the LV (the sucking effect), and 80% transvalvular flow occurs [178]. During the slow filling and atrial contraction, the left atrium needs to generate higher pressure for further filling.

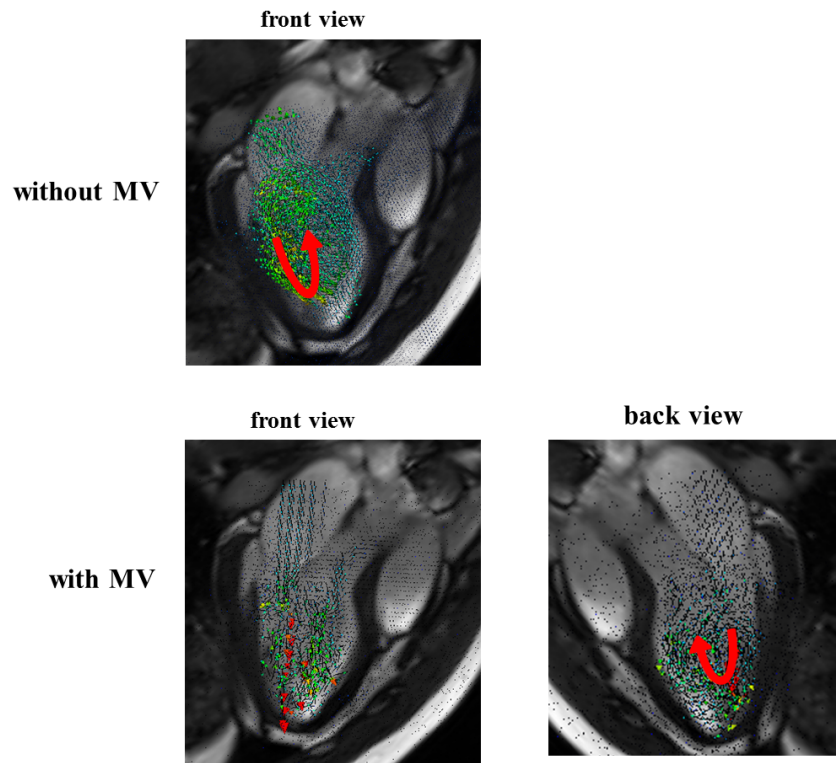


FIGURE 7.8: The vortices compared between the models with and without the MV structure.

In the MV-LV model, the ramped pressure in the inflow tract during diastole is similar to the slow filling and atrial contraction. However, the model is less accurate in simulating the rapid filling phase. This suggests that our boundary conditions need to be further improved. We also notice that during systole, the MV does not close as well as in the MV-tube model, suggesting that other factors such as the deformation of the annulus ring and the papillary muscles may have to be considered in order to produce a physiological fluid environment around the MV.

Although the MV and LV models are from the same volunteer, the complex valvular-ventricular interaction has not been fully accounted for in the current model, such as connecting the chordae tendineae to the real papillary muscles deformed along with the ventricular wall, and the changes of annulus ring shape caused by the LV contraction. Even though the MV/LV model by its own is able to simulate certain aspects of cardiac functions physiologically [148, 201], the combination of the two models requires additional treatments because the heart function is well coordinated through the

electrical-mechanical coupling, the valvular closing and opening events, etc. Furthermore, the MV structure is reconstructed when the MV opens in middle diastole, and thus there is a slight time delay for the LV model reconstructed in early diastole. When the MV just opens, the heart starts to fill, and we therefore assume that the LV geometry is similar to the shape just before the MV opens. It is worth mentioning that the different reconstruction times for the MV and LV geometry can also affect the modelling accuracy.

Other limitations include: non-realistic chordae structure, lack of the left atrium, the aortic valve and the right heart, population-based pressure boundary conditions, etc. Therefore the results from the current MV-LV model need to be interpreted with caution, and the model should be considered as a prototype model and a starting point to incorporate more factors. Currently, we are developing a completed MV-LV model which is promising for the simulation of patient-specific dynamics.

Chapter 8

Conclusion and future work

In this thesis, we have presented several mechanical models for soft tissue material characterization, including the human iris, iliac arteries and the mitral valve coupled to the left ventricle. Though these parts have very distinct geometries, there is generally a unified procedure to simulate their physiological conditions in terms of material properties.

Two clinical questions about the human iris are addressed in Chapter 3 using mathematical tools. We find that to avoid the acute angle close glaucoma, there exists a minimum size of iridotomy, which is dependent on the viscosity of the aqueous humour and the stiffness of the iris tissue. For the parameters studied, the minimum diameter of iridotomy is $300\ \mu\text{m}$ - $350\ \mu\text{m}$ in uveitic eye. We also study the buckling modes of a floppy iris during a Descemet's stripping endothelial keratoplasty, where again an orthotropic three-dimensional model is set up to implement the buckling analysis and investigate the critical intraocular pressure (IOP) required to initiate buckling. We identified a positive correlation between the critical pressure and the iris stiffness, so that the iris buckling (and hence closure) can arise in the normal IOP regime if the iris is floppy. Our model predictions highlight the key role of IOP during surgery, and this has prompted the ophthalmologists to purchase an IOP monitor for the operations.

Importantly, as the human eye is filled with aqueous humour which are composed predominantly of water and the iris is a thin membrane structure, a complex iris-aqueous interaction may be necessary to identify the roles played by the flows within the anterior

chamber. There are many other unknown issues relating to the iris. For example, the iris damage during phacoemulsification, or small incision cataract surgery, under which the floppy iris easily prolapse into the surgical incision, leading to unexpected constriction of pupil and aspiration into the phaco probe. We want to point out that the linear material model provides a first approximation to the problems and may not be proper to model the iris under large deformation. However, this avenue is not pursued now as the nonlinear material properties of iris are not yet available in the literature, and the simple linear models seem capable to capture the main factors of the problem.

In Chapter 4, We provide a plausible explanation for the exceptional phenomenon of the fibre directions present in human iliac arteries. An invariant-based fibre-reinforced nonlinear constitutive model is utilized to characterize the mechanical behaviour of arterial tissues. We use three different hypotheses to determine the ‘optimal fibre angle’ in an iliac artery model. All three hypotheses lead to the same conclusion that the optimal fibre angle in the medial layer of the iliac artery is close to the circumferential direction. The axial pre-stretch, in particular, is found to play an essential role in determining the optimal fibre angle. We note that, though this model is applicable to healthy cases, whether it is appropriate to diseased cases is an intriguing topic for further research.

In Chapter 6, a computational human mitral valve (MV) model derived from *in vivo* clinical imaging data under physiological pressure loading is developed using the immersed boundary finite element method. It incorporates experimentally-based constitutive laws in a three-dimensional fluid-structure interaction framework. A transversely isotropic material constitutive model is used to characterize the mechanical behaviour of the MV tissue based on recent mechanical tests of healthy human mitral leaflets. Our results show good agreement, in terms of the flow rate and the closing and opening configurations, with measurements from *in vivo* magnetic resonance images. The stresses in the anterior leaflet are found to be higher than those in the posterior leaflet and are concentrated around the annulus trigons and the belly of the leaflet. The results also show that the chordae play an important role in providing a secondary orifice for the flow when the valve opens. We then develop an MV model within a contractile left ventricle (LV) chamber in Chapter 7. The initial results show that the developed MV with LV model is

capable of simulating MV dynamics, LV wall deformation and ventricular flow, and has the potential to simulate the highly complex valvular-ventricular interaction. The flow patterns are rather different compared to the MV model in a tube simulator. Although there are some discrepancies to be overcome in future work, our simulations show that the developed computational model is promising in mimicking the *in vivo* MV dynamics and providing important information that are not obtainable by *in vivo* measurements.

We have addressed several issues in the MV models: 1) the complex and highly non-symmetric geometries of the MV and sub-valvular apparatus; 2) the complicated fibre architectures inside myocardium and valvular tissue; 3) the nonlinear, anisotropic material properties for different parts of the structure and 4) large deformation during the blood-structure interaction. Yet, the development of the MV modelling still faces a number of challenges. For instance, the papillary muscles contract and relax throughout cardiac cycles; the geometry of the mitral annulus is dynamically deformed; the pathological development in acute and mild time courses are still uncertain; and it is difficult to estimate personalized MV and LV material parameters from limited clinical data.

Our integrated MV and LV model may be further developed to study MV diseases and evaluate repair procedures. For instance, mitral regurgitation, in which the blood flow leaks back into the left atrium during systole, is the second most frequent valve pathology and thus imposes a considerable health burden on society [205]. In addition, an MV model with a much more detailed and realistic chordae architecture obtained from computed tomography images such as in [175] may be investigated. This is expected to largely improve the leaflet closing configuration by reducing the leak between the leaflets and developing the image-comparable valvular profile. Model development may be greatly boosted from experimental studies. For example, patient-specific material properties may be accurately obtained from e.g. diffusion tensor magnetic resonance images. Our coupled model may be extended to include the left atrium and the aortic valve. The FSI simulation for the MV model in a cardiac cycle typically takes two to three days on a local Linux workstation (8-core, 3000 MHz processors), and the coupled MV-LV model currently takes more than a week for one cardiac cycle. This means that

the computational efficiency needs to be improved in order to conduct more realistic simulations.

Lastly, regarding the material model, mathematical descriptions of multiscale behaviours spanning from the subcellular, cellular, multicellular and organ scales are of great significance, especially to fully understand the pathology development and growth mechanism.

Bibliography

- [1] G. A. Holzapfel, T. C. Gasser, and R. W. Ogden. A new constitutive framework for arterial wall mechanics and a comparative study of material models. *Journal of Elasticity*, 61(1):1–48, 2000.
- [2] K. S. Kunzelman, D. R. Einstein, and R. P. Cochran. Fluid–structure interaction models of the mitral valve: function in normal and pathological states. *Philosophical Transactions of the Royal Society B: Biological Sciences*, 362(1484):1393–1406, 2007.
- [3] U. Agrawal, N. Qi, P. Stewart, X. Y. Luo, G. Williams, A. Rotchford, and K. Ramaesh. Optimum size of iridotomy in uveitis. *Clinical & Experimental Ophthalmology*, 43(7):692–696, 2015.
- [4] D. Lockington, X. Y. Luo, H. M. Wang, N. A. Hill, and K. Ramaesh. Mathematical and computer simulation modelling of intracameral forces causing pupil block due to air bubble use in descemet’s stripping endothelial keratoplasty: the mechanics of iris buckling. *Clinical & Experimental Ophthalmology*, 40(2):182–186, 2012.
- [5] P. Maier, T. Reinhard, and C. Cursiefen. Descemet stripping endothelial keratoplasty rapid recovery of visual acuity. *Deutsches Ärzteblatt International*, 110(21):365–371, 2013.
- [6] A. J. Schriefl, G. Zeindlinger, D. M. Pierce, P. Regitnig, and G. A. Holzapfel. Determination of the layer-specific distributed collagen fibre orientations in human thoracic and abdominal aortas and common iliac arteries. *Journal of the Royal Society Interface*, 9(71):1275–1286, 2012.

-
- [7] C. A. Schulze-Bauer, C. Mörth, and G. A. Holzapfel. Passive biaxial mechanical response of aged human iliac arteries. *Journal of Biomechanical Engineering*, 125(3):395–406, 2003.
- [8] H. Kahraman, M. Ozaydin, E. Varol, S. M. Aslan, A. Dogan, A. Altinbas, M. Demir, O. Gedikli, G. Acar, and O. Ergene. The diameters of the aorta and its major branches in patients with isolated coronary artery ectasia. *Texas Heart Institute Journal*, 33(4):463–468, 2006.
- [9] N. Stergiopoulos, D. F. Young, and T. R. Rogge. Computer simulation of arterial flow with applications to arterial and aortic stenoses. *Journal of Biomechanics*, 25(12):1477–1488, 1992.
- [10] M. S. Olufsen. *Modeling the arterial system with reference to an anesthesia simulator*. PhD thesis, Roskilde University, 1998.
- [11] P. M. Shah, M. J. Tsapogas, H. A. Scarton, P. K. Jindal, and K. T. Wu. Prediction of occlusive disease for left iliac artery. *Journal of Cardiovascular Surgery*, 17(5):420–425, 1976.
- [12] Q. Long, X. Y. Xu, M. Bourne, and T. M. Griffith. Numerical study of blood flow in an anatomically realistic aorto-iliac bifurcation generated from mri data. *Magnetic Resonance in Medicine*, 43(4):565–576, 2000.
- [13] G. A. Holzapfel, G. Sommer, and P. Regitnig. Anisotropic mechanical properties of tissue components in human atherosclerotic plaques. *Journal of Biomechanical Engineering*, 126(5):657–665, 2004.
- [14] T. Waffenschmidt and A. Menzel. Extremal states of energy of a double-layered thick-walled tube—application to residually stressed arteries. *Journal of the Mechanical Behavior of Biomedical Materials*, 29:635–654, 2014.
- [15] X. S. Ma, H. Gao, B. E. Griffith, C. Berry, and X. Y. Luo. Image-based fluid–structure interaction model of the human mitral valve. *Computers & Fluids*, 71:417–425, 2013.

- [16] H. Gao, N. Qi, X. S. Ma, B. E. Griffith, C. Berry, and X. Y. Luo. Fluid-structure interaction model of human mitral valve within left ventricle. In *Functional Imaging and Modeling of the Heart*, pages 330–337. Springer, 2015.
- [17] Y. C. Fung. What are the residual stresses doing in our blood vessels? *Annals of Biomedical Engineering*, 19(3):237–249, 1991.
- [18] Y. C. Fung and P. Tong. *Classical and computational solid mechanics*, volume 1. World Scientific, 2001.
- [19] T. V. Roberts, I. C. Francis, S. Lertusumitkul, M. B. Kappagoda, and M. T. Coroneo. Primary phacoemulsification for uncontrolled angle-closure glaucoma. *Journal of Cataract & Refractive Surgery*, 26(7):1012–1016, 2000.
- [20] D. F. Chang and J. R. Campbell. Intraoperative floppy iris syndrome associated with tamsulosin. *Journal of Cataract & Refractive Surgery*, 31(4):664–673, 2005.
- [21] R. J. Powell, M. Fillinger, D. B. Walsh, R. Zwolak, and J. L. Cronenwett. Predicting outcome of angioplasty and selective stenting of multisegment iliac artery occlusive disease. *Journal of Vascular Surgery*, 32(3):564–569, 2000.
- [22] K. L. Moore, A. F. Dalley, and A. M. Agur. *Clinically oriented anatomy*. Lippincott Williams & Wilkins, 2013.
- [23] J. K. Perloff and W. C. Roberts. The mitral apparatus functional anatomy of mitral regurgitation. *Circulation*, 46(2):227–239, 1972.
- [24] A. S. Go, D. Mozaffarian, V. L. Roger, E. J. Benjamin, J. D. Berry, M. J. Blaha, S. Dai, E. S. Ford, C. S. Fox, S. Franco, et al. Heart disease and stroke statistics—2014 update: a report from the american heart association. *Circulation*, 129(3):e28–e292, 2014.
- [25] W. Bothe, J. P. Escobar Kvitting, J. C. Swanson, S. Hartnett, N. B. Ingels Jr, and D. C. Miller. Effects of different annuloplasty rings on anterior mitral leaflet dimensions. *The Journal of Thoracic and Cardiovascular Surgery*, 139(5):1114–1122, 2010.

- [26] W. Bothe, J. E. Kvitting, J. C. Swanson, S. Göktepe, K. N. Vo, N. B. Ingels, and D. C. Miller. How do annuloplasty rings affect mitral leaflet dynamic motion? *European Journal of Cardio-Thoracic Surgery*, 38(3):340–349, 2010.
- [27] Q. Wang, E. Sirois, and W. Sun. Patient-specific modeling of biomechanical interaction in transcatheter aortic valve deployment. *Journal of Biomechanics*, 45(11):1965–1971, 2012.
- [28] K. May-Newman and F. C. Yin. A constitutive law for mitral valve tissue. *Journal of Biomechanical Engineering*, 120(1):38–47, 1998.
- [29] E. Votta, T. B. Le, M. Stevanella, L. Fusini, E. G. Caiani, A. Redaelli, and F. Sotiropoulos. Toward patient-specific simulations of cardiac valves: State-of-the-art and future directions. *Journal of Biomechanics*, 46(2):217–228, 2013.
- [30] W. Sun, C. Martin, and T. Pham. Computational modeling of cardiac valve function and intervention. *Annual Review of Biomedical Engineering*, 16:53–76, 2014.
- [31] C. Catalano, M. Anzidei, and A. Napoli. *Cardiovascular CT and MR imaging: from technique to clinical interpretation*. Springer Science & Business Media, 2013.
- [32] R. J. Kim, E. L. Chen, R. M. Judd, et al. Myocardial gad-dtpa kinetics determine mri contrast enhancement and reflect the extent and severity of myocardial injury after acute reperfused infarction. *Circulation*, 94(12):3318–3326, 1996.
- [33] W. A. Helbing, H. G. Bosch, C. Maliepaard, S. A. Rebergen, R. J. van der Geest, B. Hansen, J. Ottenkamp, J. H. Reiber, and A. de Roos. Comparison of echocardiographic methods with magnetic resonance imaging for assessment of right ventricular function in children. *The American Journal of Cardiology*, 76(8):589–594, 1995.
- [34] A. Khaled, R. Scott, J. Tim, and S. Mohan. Assessment of ventricular function and mass by cardiac magnetic resonance imaging. *European Radiology*, 14(10):1813–1822, 2004.

- [35] R. A. Levine, M. D. Handschumacher, A. J. Sanfilippo, A. A. Hagege, P. Harrigan, J. E. Marshall, and A. E. Weyman. Three-dimensional echocardiographic reconstruction of the mitral valve, with implications for the diagnosis of mitral valve prolapse. *Circulation*, 80(3):589–598, 1989.
- [36] S. Chandra, I. S. Salgo, L. Sugeng, L. Weinert, S. H. Settlemier, V. Mor-Avi, and R. M. Lang. A three-dimensional insight into the complexity of flow convergence in mitral regurgitation: adjunctive benefit of anatomic regurgitant orifice area. *American Journal of Physiology-Heart and Circulatory Physiology*, 301(3):H1015–H1024, 2011.
- [37] M. Gutberlet, H. Abdul-Khaliq, M. Grothoff, J. Schröter, B. Schmitt, R. Röttgen, P. Lange, M. Vogel, and R. Felix. Evaluation of left ventricular volumes in patients with congenital heart disease and abnormal left ventricular geometry. comparison of mri and transthoracic 3-dimensional echocardiography. *RoFo: Fortschritte auf dem Gebiete der Röntgenstrahlen und der Nuklearmedizin*, 175(7):942–951, 2003.
- [38] A. L. Rosenbaum and A. P. Santiago. *Clinical strabismus management: principles and surgical techniques*. David Hunter, 1999.
- [39] R. W. Ogden. *Non-linear elastic deformations*. Courier Corporation, 1997.
- [40] C. J. Chuong and Y. C. Fung. Compressibility and constitutive equation of arterial wall in radial compression experiments. *Journal of Biomechanics*, 17(1):35–40, 1984.
- [41] J. F. Greenleaf, M. Fatemi, and M. Insana. Selected methods for imaging elastic properties of biological tissues. *Annual Review of Biomedical Engineering*, 5(1):57–78, 2003.
- [42] J. M. Gere and S. P. Timoshenko. *Theory of elastic stability*. 1961.
- [43] J. Merodio and R. W. Ogden. Mechanical response of fiber-reinforced incompressible non-linearly elastic solids. *International Journal of Non-Linear Mechanics*, 40(2):213–227, 2005.
- [44] A. J. M. Spencer. Constitutive theory for strongly anisotropic solids. In *Continuum theory of the mechanics of fibre-reinforced composites*, pages 1–32. Springer, 1984.

- [45] G. A. Holzapfel and R. W. Ogden. Constitutive modelling of passive myocardium: a structurally based framework for material characterization. *Philosophical Transactions of the Royal Society A: Mathematical, Physical and Engineering Sciences*, 367(1902):3445–3475, 2009.
- [46] P. A. Netland and N. C. Denton. Uveitic glaucoma. *Contemp Ophthalmol*, 5(17):1–8, 2006.
- [47] L. W. Schwartz, M. R. Moster, G. L. Spaeth, R. P. Wilson, and E. Poryzees. Neodymium-yag laser iridectomies in glaucoma associated with closed or occludable angles. *American Journal of Ophthalmology*, 102(1):41–44, 1986.
- [48] B. W. Fleck. How large must an iridotomy be? *British Journal of Ophthalmology*, 74(10):583–588, 1990.
- [49] N. A. Spencer, A. J. Hall, and R. J. Stawell. Nd: Yag laser iridotomy in uveitic glaucoma. *Clinical & Experimental Ophthalmology*, 29(4):217–219, 2001.
- [50] J. J. Heys and V. H. Barocas. Mechanical characterization of the bovine iris. *Journal of Biomechanics*, 32(9):999–1003, 1999.
- [51] M. A. Haidekker, A. G. Tsai, T. Brady, H. Y. Stevens, J. A. Frangos, E. Theodorakis, and M. Intaglietta. A novel approach to blood plasma viscosity measurement using fluorescent molecular rotors. *American Journal of Physiology-Heart and Circulatory Physiology*, 282(5):H1609–H1614, 2002.
- [52] J. W. Kiel, M. Hollingsworth, R. Rao, M. Chen, and H. A. Reitsamer. Ciliary blood flow and aqueous humor production. *Progress in Retinal and Eye Research*, 30(1):1–17, 2011.
- [53] J. J. Heys, V. H. Barocas, and M. J. Taravella. Modeling passive mechanical interaction between aqueous humor and iris. *Journal of Biomechanical Engineering*, 123(6):540–547, 2001.
- [54] M. O. Price and F. W. Price. Descemet’s stripping endothelial keratoplasty. *Current Opinion in Ophthalmology*, 18(4):290–294, 2007.

- [55] I. H. Fine, R. S. Hoffman, and M. Packer. Descemet's stripping endothelial keratoplasty. In *Minimally Invasive Ophthalmic Surgery*, pages 82–87. Springer, 2010.
- [56] W. W. Culbertson. Descemet stripping endothelial keratoplasty. *International Ophthalmology Clinics*, 46(3):155–168, 2006.
- [57] W. B. Lee, D. S. Jacobs, D. C. Musch, S. C. Kaufman, W. J. Reinhart, and R. M. Shtein. Descemet's stripping endothelial keratoplasty: safety and outcomes: a report by the american academy of ophthalmology. *Ophthalmology*, 116(9):1818–1830, 2009.
- [58] A. D. Fitt and G. Gonzalez. Fluid mechanics of the human eye: aqueous humour flow in the anterior chamber. *Bulletin of Mathematical Biology*, 68(1):53–71, 2006.
- [59] C. R. Canning, M. J. Greaney, J. N. Dewynne, and A. D. Fitt. Fluid flow in the anterior chamber of a human eye. *Mathematical Medicine and Biology*, 19(1):31–60, 2002.
- [60] E. C. Huang and V. H. Barocas. Active iris mechanics and pupillary block: steady-state analysis and comparison with anatomical risk factors. *Annals of Biomedical Engineering*, 32(9):1276–1285, 2004.
- [61] E. C. Huang and V. H. Barocas. Accommodative microfluctuations and iris contour. *Journal of Vision*, 6(5):10, 2006.
- [62] J. A. Goldsmith, Y. Li, M. R. Chalita, V. Westphal, C. A. Patil, A. M. Rollins, J. A. Izatt, and D. Huang. Anterior chamber width measurement by high-speed optical coherence tomography. *Ophthalmology*, 112(2):238–244, 2005.
- [63] C. K. Leung, P. M. Palmiero, R. N. Weinreb, H. Li, Z. Sbeity, S. Dorairaj, D. Leung, S. Liu, J. M. Liebmann, N. Congdon, et al. Comparisons of anterior segment biometry between chinese and caucasians using anterior segment optical coherence tomography. *British Journal of Ophthalmology*, 94(9):1184–1189, 2010.
- [64] A. Neri, R. Leaci, J. C. Zenteno, C. Casubolo, E. Delfini, and C. Macaluso. Membrane frizzled-related protein gene-related ophthalmological syndrome: 30-month follow-up of a sporadic case and review of genotype-phenotype correlation in the literature. *Molecular Vision*, 18:2623–2632, 2012.

- [65] B. S. Wang, L. M. Sakata, D. S. Friedman, Y. H. Chan, M. G. He, R. Lavanya, T. Y. Wong, and T. Aung. Quantitative iris parameters and association with narrow angles. *Ophthalmology*, 117(1):11–17, 2010.
- [66] K. J. Bathe. *Finite element procedures*. Klaus-Jurgen Bathe, 2006.
- [67] W. H. Wittrick and F. W. Williams. An algorithm for computing critical buckling loads of elastic structures. *Journal of Structural Mechanics*, 1(4):497–518, 1973.
- [68] Dassault Systèmes. *Abaqus 6.13 analysis user's guide*, 2013. URL <http://50.16.176.52/v6.13/books/usb/default.php>.
- [69] J. E. Whitcomb, V. A. Barnett, T. W. Olsen, and V. H. Barocas. Ex vivo porcine iris stiffening due to drug stimulation. *Experimental Eye Research*, 89(4):456–461, 2009.
- [70] A. Heijl, M. C. Leske, B. Bengtsson, L. Hyman, B. Bengtsson, and M. Hussein. Reduction of intraocular pressure and glaucoma progression: results from the early manifest glaucoma trial. *Archives of Ophthalmology*, 120(10):1268–1279, 2002.
- [71] H. C. Han. A biomechanical model of artery buckling. *Journal of Biomechanics*, 40(16):3672–3678, 2007.
- [72] P. R. Townsend, R. M. Rose, and E. L. Radin. Buckling studies of single human trabeculae. *Journal of Biomechanics*, 8(3):199–201, 1975.
- [73] F. Bloom and D. Coffin. *Handbook of thin plate buckling and postbuckling*. CRC Press, 2000.
- [74] N. Qi, H. Gao, R. W. Ogden, N. A. Hill, G. A. Holzapfel, H. C. Han, and X. Y. Luo. Investigation of the optimal collagen fibre orientation in human iliac arteries. *Journal of the Mechanical Behavior of Biomedical Materials*, 52:108–119, 2015.
- [75] T. C. Gasser, R. W. Ogden, and G. A. Holzapfel. Hyperelastic modelling of arterial layers with distributed collagen fibre orientations. *Journal of the Royal Society Interface*, 3(6):15–35, 2006.

- [76] G. A. Holzapfel, G. Sommer, C. T. Gasser, and P. Regitnig. Determination of layer-specific mechanical properties of human coronary arteries with nonatherosclerotic intimal thickening and related constitutive modeling. *American Journal of Physiology-Heart and Circulatory Physiology*, 289(5):H2048–H2058, 2005.
- [77] P. Mangell, T. Länne, B. Sonesson, F. Hansen, and D. Bergqvist. Regional differences in mechanical properties between major arteries an experimental study in sheep. *European Journal of Vascular and Endovascular Surgery*, 12(2):189–195, 1996.
- [78] P. M. Canham, H. M. Finlay, J. G. Dixon, D. R. Boughner, and A. Chen. Measurements from light and polarised light microscopy of human coronary arteries fixed at distending pressure. *Cardiovascular Research*, 23(11):973–982, 1989.
- [79] H. M. Finlay, L. McCullough, and P. B. Canham. Three-dimensional collagen organization of human brain arteries at different transmural pressures. *Journal of Vascular Research*, 32(5):301–312, 1995.
- [80] H. M. Finlay, P. Whittaker, and P. B. Canham. Collagen organization in the branching region of human brain arteries. *Stroke*, 29(8):1595–1601, 1998.
- [81] M. R. Roach and A. C. Burton. The reason for the shape of the distensibility curves of arteries. *Canadian Journal of Biochemistry and Physiology*, 35(8):681–690, 1957.
- [82] Y. Lanir. Constitutive equations for fibrous connective tissues. *Journal of Biomechanics*, 16(1):1–12, 1983.
- [83] G. A. Holzapfel and R. W. Ogden. On the tension–compression switch in soft fibrous solids. *European Journal of Mechanics-A/Solids*, 49:561–569, 2015.
- [84] G. A. Holzapfel, J. A. Niestrawska, R. W. Ogden, A. J. Reinisch, and A. J. Schriefl. Modelling non-symmetric collagen fibre dispersion in arterial walls. *Journal of the Royal Society Interface*, 12(106):1–14, 2015.

- [85] G. A. Holzapfel and T. C. Gasser. A viscoelastic model for fiber-reinforced composites at finite strains: Continuum basis, computational aspects and applications. *Computer Methods in Applied Mechanics and Engineering*, 190(34):4379–4403, 2001.
- [86] G. A. Holzapfel and R. W. Ogden. Constitutive modelling of arteries. *Proceedings of the Royal Society A: Mathematical, Physical and Engineering Science*, 466(2118):1551–1597, 2010.
- [87] G. A. Holzapfel and H. W. Weizsäcker. Biomechanical behavior of the arterial wall and its numerical characterization. *Computers in Biology and Medicine*, 28(4):377–392, 1998.
- [88] G. A. Holzapfel, M. Stadler, and T. C. Gasser. Changes in the mechanical environment of stenotic arteries during interaction with stents: computational assessment of parametric stent designs. *Journal of Biomechanical Engineering*, 127(1):166–180, 2005.
- [89] H. Demiray. A note on the elasticity of soft biological tissues. *Journal of Biomechanics*, 5(3):309–311, 1972.
- [90] G. A. Holzapfel, G. Sommer, M. Auer, P. Regitnig, and R. W. Ogden. Layer-specific 3D residual deformations of human aortas with non-atherosclerotic intimal thickening. *Annals of Biomedical Engineering*, 35(4):530–545, 2007.
- [91] J. Ohayon, G. Finet, F. Treyve, G. Rioufol, and O. Dubreuil. A three-dimensional finite element analysis of stress distribution in a coronary atherosclerotic plaque: In-vivo prediction of plaque rupture location. *Biomechanics Applied to Computer Assisted Surgery*, 37(2):225–241, 2005.
- [92] G. A. Holzapfel and T. C. Gasser. Computational stress-deformation analysis of arterial walls including high-pressure response. *International Journal of Cardiology*, 116(1):78–85, 2007.
- [93] A. Delfino, N. Stergiopoulos, J. E. Moore, and J. J. Meister. Residual strain effects on the stress field in a thick wall finite element model of the human carotid bifurcation. *Journal of Biomechanics*, 30(8):777–786, 1997.

- [94] G. A. Holzapfel, T. C. Gasser, and R. W. Ogden. Comparison of a multi-layer structural model for arterial walls with a fung-type model, and issues of material stability. *Journal of Biomechanical Engineering*, 126(2):264–275, 2004.
- [95] F. Gao, M. Watanabe, and T. Matsuzawa. Stress analysis in a layered aortic arch model under pulsatile blood flow. *BioMedical Engineering OnLine*, 5(25):1–11, 2006.
- [96] C. J. Chuong and Y. C. Fung. Residual stress in arteries. In G. W. Schmid-Schönbein, S. L.-Y. Woo, and publisher=Springer Zweifach, B. W. year=1986, editors, *Frontiers in Biomechanics*, pages 117–129.
- [97] K. Takamizawa and K. Hayashi. Strain energy density function and uniform strain hypothesis for arterial mechanics. *Journal of Biomechanics*, 20(1):7–17, 1987.
- [98] S. E. Greenwald, J. E. Moore, A. Rachev, T. P. C. Kane, and J. J. Meister. Experimental investigation of the distribution of residual strains in the artery wall. *Journal of Biomechanical Engineering*, 119(4):438–444, 1997.
- [99] F. Auricchio, M. Conti, and A. Ferrara. How constitutive model complexity can affect the capability to fit experimental data: a focus on human carotid arteries and extension/inflation data. *Archives of Computational Methods in Engineering*, 21(3):273–292, 2014.
- [100] Y. C. Fung and S. Q. Liu. Change of residual strains in arteries due to hypertrophy caused by aortic constriction. *Circulation Research*, 65(5):1340–1349, 1989.
- [101] M. A. Zulliger, P. Fridez, K. Hayashi, and N. Stergiopoulos. A strain energy function for arteries accounting for wall composition and structure. *Journal of Biomechanics*, 37(7):989–1000, 2004.
- [102] I. Hariton, G. Debotton, T. C. Gasser, and G. A. Holzapfel. Stress-driven collagen fiber remodeling in arterial walls. *Biomechanics and Modeling in Mechanobiology*, 6(3):163–175, 2007.
- [103] N. J. Driessen, W. Wilson, C. V. Bouten, and F. P. Baaijens. A computational model for collagen fibre remodelling in the arterial wall. *Journal of Theoretical Biology*, 226(1):53–64, 2004.

- [104] H. C. Han and Y. C. Fung. Longitudinal strain of canine and porcine aortas. *Journal of Biomechanics*, 28(5):637–641, 1995.
- [105] T. C. Gasser, C. A. Schulze-Bauer, and G. A. Holzapfel. A three-dimensional finite element model for arterial clamping. *Journal of Biomechanical Engineering*, 124(4):355–363, 2002.
- [106] L. Cardamone, A. Valentin, J. F. Eberth, and J. D. Humphrey. Origin of axial pre-stretch and residual stress in arteries. *Biomechanics and Modeling in Mechanobiology*, 8(6):431–446, 2009.
- [107] G. Sommer, P. Regitnig, L. Költringer, and G. A. Holzapfel. Biaxial mechanical properties of intact and layer-dissected human carotid arteries at physiological and suprphysiological loadings. *American Journal of Physiology-Heart and Circulatory Physiology*, 298(3):H898–H912, 2010.
- [108] H. C. Han and Y. C. Fung. Species dependence of the zero-stress state of aorta: pig versus rat. *Journal of Biomechanical Engineering*, 113(4):446–451, 1991.
- [109] H. C. Han, S. Marita, and D. N. Ku. Changes of opening angle in hypertensive and hypotensive arteries in 3-day organ culture. *Journal of Biomechanics*, 39(13):2410–2418, 2006.
- [110] A. J. M. Spencer, R. L. Moss, and T. G. Rogers. Pure bending of helically wound ideal fibre-reinforced cylinders. *Journal of Elasticity*, 5(3-4):287–296, 1975.
- [111] T. Stylianopoulos and V. H. Barocas. Multiscale, structure-based modeling for the elastic mechanical behavior of arterial walls. *Journal of Biomechanical Engineering*, 129(4):611–618, 2007.
- [112] F. Maceri, M. Marino, and G. Vairo. A unified multiscale mechanical model for soft collagenous tissues with regular fiber arrangement. *Journal of Biomechanics*, 43(2):355–363, 2010.
- [113] H. Weisbecker, M. J. Unterberger, and G. A. Holzapfel. Constitutive modelling of arteries considering fibre recruitment and three-dimensional fibre distribution. *Journal of the Royal Society Interface*, 12(105):1–10, 2015.

- [114] G. Sommer and G. A. Holzapfel. 3D constitutive modeling of the biaxial mechanical response of intact and layer-dissected human carotid arteries. *Journal of the Mechanical Behavior of Biomedical Materials*, 5(1):116–128, 2012.
- [115] R. Van Loon and F. N. Van de Vosse. Special issue: Fluid–structure interaction in biomedical applications. *International Journal for Numerical Methods in Biomedical Engineering*, 26(3-4):273–275, 2010.
- [116] J. Donea, S. Giuliani, and J. P. Halleux. An arbitrary lagrangian-eulerian finite element method for transient dynamic fluid-structure interactions. *Computer Methods in Applied Mechanics and Engineering*, 33(1):689–723, 1982.
- [117] R. Cheng, Y. G. Lai, and K. B. Chandran. Two-dimensional fluid-structure interaction simulation of bileaflet mechanical heart valve flow dynamics. *The Journal of Heart Valve Disease*, 12(6):772–780, 2003.
- [118] Y. S. Morsi, W. W. Yang, C. S. Wong, and S. Das. Transient fluid–structure coupling for simulation of a trileaflet heart valve using weak coupling. *Journal of Artificial Organs*, 10(2):96–103, 2007.
- [119] D. M. Espino, D. E. Shepherd, and D. W. Hukins. Evaluation of a transient, simultaneous, arbitrary lagrange–euler based multi-physics method for simulating the mitral heart valve. *Computer Methods in Biomechanics and Biomedical Engineering*, 17(4):450–458, 2014.
- [120] F. Sotiropoulos and I. Borazjani. A review of state-of-the-art numerical methods for simulating flow through mechanical heart valves. *Medical & Biological Engineering & Computing*, 47(3):245–256, 2009.
- [121] F. P. T. Baaijens. A fictitious domain/mortar element method for fluid-structure interaction. *International Journal for Numerical Methods in Fluids*, 35(7):743–761, 2001.
- [122] R. Glowinski, T. W. Pan, T. I. Hesla, and D. D. Joseph. A distributed lagrange multiplier/fictitious domain method for particulate flows. *International Journal of Multiphase Flow*, 25(5):755–794, 1999.

- [123] J. De Hart, G. W. Peters, P. J. Schreurs, and F. P. Baaijens. A two-dimensional fluid–structure interaction model of the aortic valve. *Journal of Biomechanics*, 33(9):1079–1088, 2000.
- [124] J. De Hart, G. W. Peters, P. J. Schreurs, and F. P. Baaijens. A three-dimensional computational analysis of fluid–structure interaction in the aortic valve. *Journal of Biomechanics*, 36(1):103–112, 2003.
- [125] J. De Hart, F. P. Baaijens, G. W. Peters, and P. J. Schreurs. A computational fluid–structure interaction analysis of a fiber-reinforced stentless aortic valve. *Journal of Biomechanics*, 36(5):699–712, 2003.
- [126] R. Van Loon, P. D. Anderson, J. De Hart, and F. P. Baaijens. A combined fictitious domain/adaptive meshing method for fluid–structure interaction in heart valves. *International Journal for Numerical Methods in Fluids*, 46(5):533–544, 2004.
- [127] R. Van Loon, P. D. Anderson, and F. N. Van de Vosse. A fluid–structure interaction method with solid-rigid contact for heart valve dynamics. *Journal of Computational Physics*, 217(2):806–823, 2006.
- [128] C. S. Peskin. Flow patterns around heart valves: a numerical method. *Journal of Computational Physics*, 10(2):252–271, 1972.
- [129] M. C. Lai and C. S. Peskin. An immersed boundary method with formal second-order accuracy and reduced numerical viscosity. *Journal of Computational Physics*, 160(2):705–719, 2000.
- [130] A. M. Roma, C. S. Peskin, and M. J. Berger. An adaptive version of the immersed boundary method. *Journal of Computational Physics*, 153(2):509–534, 1999.
- [131] B. E. Griffith, R. D. Hornung, D. M. McQueen, and C. S. Peskin. An adaptive, formally second order accurate version of the immersed boundary method. *Journal of Computational Physics*, 223(1):10–49, 2007.
- [132] C. S. Peskin. Fluid dynamics of the heart and its valves. In *APS Meeting Abstracts*, volume 1. 1997.

- [133] B. E. Griffith. *Simulating the blood-muscle-valve mechanics of the heart by an adaptive and parallel version of the immersed boundary method*. PhD thesis, New York University, 2005.
- [134] B. E. Griffith, X. Y. Luo, D. M. McQueen, and C. S. Peskin. Simulating the fluid dynamics of natural and prosthetic heart valves using the immersed boundary method. *International Journal of Applied Mechanics*, 1(1):137–177, 2009.
- [135] B. E. Griffith. Immersed boundary model of aortic heart valve dynamics with physiological driving and loading conditions. *International Journal for Numerical Methods in Biomedical Engineering*, 28(3):317–345, 2012.
- [136] X. Y. Luo, B. E. Griffith, X. S. Ma, M. Yin, T. J. Wang, C. L. Liang, P. N. Watton, and G. M. Bernacca. Effect of bending rigidity in a dynamic model of a polyurethane prosthetic mitral valve. *Biomechanics and Modeling in Mechanobiology*, 11(6):815–827, 2012.
- [137] L. Zhang, A. Gerstenberger, X. Wang, and W. K. Liu. Immersed finite element method. *Computer Methods in Applied Mechanics and Engineering*, 193(21):2051–2067, 2004.
- [138] L. T. Zhang and M. Gay. Immersed finite element method for fluid-structure interactions. *Journal of Fluids and Structures*, 23(6):839–857, 2007.
- [139] D. Boffi, L. Gastaldi, L. Heltai, and C. S. Peskin. On the hyper-elastic formulation of the immersed boundary method. *Computer Methods in Applied Mechanics and Engineering*, 197(25):2210–2231, 2008.
- [140] W. K. Liu, Y. L. Liu, D. Farrell, L. Zhang, X. S. Wang, Y. Fukui, N. Patankar, Y. Zhang, C. Bajaj, J. Lee, et al. Immersed finite element method and its applications to biological systems. *Computer Methods in Applied Mechanics and Engineering*, 195(13):1722–1749, 2006.
- [141] L. Heltai and F. Costanzo. Variational implementation of immersed finite element methods. *Computer Methods in Applied Mechanics and Engineering*, 229:110–127, 2012.

-
- [142] B. E. Griffith and X. Y. Luo. Hybrid finite difference/finite element version of the immersed boundary method. *Submitted in revised form*, 2012.
- [143] C. S. Peskin. Numerical analysis of blood flow in the heart. *Journal of Computational Physics*, 25(3):220–252, 1977.
- [144] C. S. Peskin. The immersed boundary method. *Acta Numerica*, 11(1):479–517, 2002.
- [145] B. E. Griffith. An accurate and efficient method for the incompressible navier–stokes equations using the projection method as a preconditioner. *Journal of Computational Physics*, 228(20):7565–7595, 2009.
- [146] B. E. Griffith. On the volume conservation of the immersed boundary method. *Communications in Computational Physics*, 12(2):401, 2012.
- [147] C. A. Fletcher. *Computational galerkin methods*. Springer, 1984.
- [148] H. Gao, X. S Ma, N. Qi, C. Berry, B. E. Griffith, and X. Y. Luo. A finite strain nonlinear human mitral valve model with fluid-structure interaction. *International Journal for Numerical Methods in Biomedical Engineering*, 30(12):1597–1613, 2014.
- [149] K. May-Newman and F. C. Yin. Biaxial mechanical behavior of excised porcine mitral valve leaflets. *American Journal of Physiology-Heart and Circulatory Physiology*, 269(4):H1319–H1327, 1995.
- [150] V. Prot and B. Skallerud. An improved transverse isotropic hyperelastic material model for simulation of mitral valve response. *Journal of Biomechanics*, 39:S618–S618, 2006.
- [151] V. Prot, R. Haaverstad, and B. Skallerud. Finite element analysis of the mitral apparatus: annulus shape effect and chordal force distribution. *Biomechanics and Modeling in Mechanobiology*, 8(1):43–55, 2009.
- [152] V. Prot and B. Skallerud. Nonlinear solid finite element analysis of mitral valves with heterogeneous leaflet layers. *Computational Mechanics*, 43(3):353–368, 2009.

- [153] V. Prot, B. Skallerud, G. Sommer, and G. A. Holzapfel. On modelling and analysis of healthy and pathological human mitral valves: Two case studies. *Journal of the Mechanical Behavior of Biomedical Materials*, 3(2):167–177, 2010.
- [154] G. Krishnamurthy, A. Itoh, W. Bothe, J. C. Swanson, E. Kuhl, M. Karlsson, D. Craig Miller, and N. B. Ingels Jr. Stress–strain behavior of mitral valve leaflets in the beating ovine heart. *Journal of Biomechanics*, 42(12):1909–1916, 2009.
- [155] C. H. Lee, R. Amini, R. C. Gorman, J. H. Gorman III, and M. S. Sacks. An inverse modeling approach for stress estimation in mitral valve anterior leaflet valvuloplasty for in-vivo valvular biomaterial assessment. *Journal of Biomechanics*, 47(9):2055–2063, 2014.
- [156] K. S. Kunzelman, R. P. Cochran, C. Chuong, W. S. Ring, E. D. Verrier, and R. D. Eberhart. Finite element analysis of the mitral valve. *Journal of Heart Valve Disease*, 2(3):326–340, 1993.
- [157] K. S. Kunzelman, M. S. Reimink, and R. P. Cochran. Annular dilatation increases stress in the mitral valve and delays coaptation: a finite element computer model. *Cardiovascular Surgery*, 5(4):427–434, 1997.
- [158] K. S. Kunzelman, M. S. Reimink, and R. P. Cochran. Flexible versus rigid ring annuloplasty for mitral valve annular dilatation: a finite element model. *Journal of Heart Valve Disease*, 7(1):108–116, 1998.
- [159] M. S. Reimink, K. S. Kunzelman, and R. P. Cochran. The effect of chordal replacement suture length on function and stresses in repaired mitral valves: a finite element study. *Journal of Heart Valve Disease*, 5(4):365–375, 1996.
- [160] B. Skallerud, V. Prot, and I. S. Nordrum. Modeling active muscle contraction in mitral valve leaflets during systole: a first approach. *Biomechanics and Modeling in Mechanobiology*, 10(1):1–16, 2011.
- [161] M. Stevanella, G. Krishnamurthy, E. Votta, J. C. Swanson, A. Redaelli, and N. B. Ingels Jr. Mitral leaflet modeling: Importance of in vivo shape and material properties. *Journal of Biomechanics*, 44(12):2229–2235, 2011.

- [162] M. Stevanella, F. Maffessanti, C. A. Conti, E. Votta, A. Arnoldi, M. Lombardi, O. Parodi, E. G. Caiani, and A. Redaelli. Mitral valve patient-specific finite element modeling from cardiac mri: Application to an annuloplasty procedure. *Cardiovascular Engineering and Technology*, 2(2):66–76, 2011.
- [163] K. H. Lim, J. H. Yeo, and C. M. Duran. Three-dimensional asymmetrical modeling of the mitral valve: a finite element study with dynamic boundaries. *Journal of Heart Valve Disease*, 14(3):386–392, 2005.
- [164] J. F. Wenk, Z. Zhang, G. Cheng, D. Malhotra, G. Acevedo-Bolton, M. Burger, T. Suzuki, D. A. Saloner, A. W. Wallace, J. M. Guccione, et al. First finite element model of the left ventricle with mitral valve: insights into ischemic mitral regurgitation. *The Annals of Thoracic Surgery*, 89(5):1546–1553, 2010.
- [165] F. Maisano, A. Redaelli, M. Soncini, E. Votta, L. Arcobasso, and O. Alfieri. An annular prosthesis for the treatment of functional mitral regurgitation: Finite element model analysis of a dog bone-shaped ring prosthesis. *The Annals of Thoracic Surgery*, 79(4):1268–1275, 2005.
- [166] E. Votta, F. Maisano, O. Alfieri, F. M. Montevicchi, and A. Redaelli. Finite element models of newly shaped prosthetic rings for the correction of functional mitral regurgitation. *Journal of Biomechanics*, 39:S293, 2006.
- [167] E. Votta, F. Maisano, S. F. Bolling, O. Alfieri, F. M. Montevicchi, and A. Redaelli. The geofom disease-specific annuloplasty system: A finite element study. *Annals of Thoracic Surgery*, 84(1):92–101, 2007.
- [168] S. A. Urankar. *Modeling surgical interventions in the mitral valve with the finite element method*. PhD thesis, University of Pittsburgh, 2009.
- [169] K. D. Lau, V. Diaz, P. Scambler, and G. Burriesci. Mitral valve dynamics in structural and fluid-structure interaction models. *Medical Engineering & Physics*, 32(9):1057–1064, 2010.

- [170] D. R. Einstein, P. Reinhall, M. Nicosia, R. P. Cochran, and K. Kunzelman. Dynamic finite element implementation of nonlinear, anisotropic hyperelastic biological membranes. *Computer Methods in Biomechanics and Biomedical Engineering*, 6(1):33–44, 2003.
- [171] D. R. Einstein, K. S. Kunzelman, P. G. Reinhall, M. A. Nicosia, and R. P. Cochran. Non-linear fluid-coupled computational model of the mitral valve. *Journal of Heart Valve Disease*, 14(3):376–385, 2005.
- [172] K. D. Lau, V. Díaz-Zuccarini, P. Scambler, and G. Burriesci. Fluid–structure interaction study of the edge-to-edge repair technique on the mitral valve. *Journal of Biomechanics*, 44(13):2409–2417, 2011.
- [173] P. N. Watton, X. Y. Luo, X. Wang, G. M. Bernacca, P. Molloy, and D. J. Wheatley. Dynamic modelling of prosthetic chorded mitral valves using the immersed boundary method. *Journal of Biomechanics*, 40(3):613–626, 2007.
- [174] P. N. Watton, X. Y. Luo, M. Yin, G. M. Bernacca, and D. J. Wheatley. Effect of ventricle motion on the dynamic behaviour of chorded mitral valves. *Journal of Fluids and Structures*, 24(1):58–74, 2008.
- [175] Q. Wang and W. Sun. Finite element modeling of mitral valve dynamic deformation using patient-specific multi-slices computed tomography scans. *Annals of Biomedical Engineering*, 41(1):142–153, 2013.
- [176] H. Gao, H. Wang, C. Berry, X. Y. Luo, and B. E. Griffith. Quasi-static image-based immersed boundary-finite element model of left ventricle under diastolic loading. *International Journal for Numerical Methods in Biomedical Engineering*, 30(11):1199–1222, 2014.
- [177] J. A. Casado, S. Diego, D. Ferreño, E. Ruiz, I. Carrascal, D. Méndez, J. M. Revuelta, A. Pontón, J. M. Icardo, and F. Gutiérrez-Solana. Determination of the mechanical properties of normal and calcified human mitral chordae tendineae. *Journal of the Mechanical Behavior of Biomedical Materials*, 13:1–13, 2012.

- [178] R. A. Nishimura and A. J. Tajik. Evaluation of diastolic filling of left ventricle in health and disease: Doppler echocardiography is the clinician's rosetta stone. *Journal of the American College of Cardiology*, 30(1):8–18, 1997.
- [179] F. Davachi, J. H. Moller, and J. E. Edwards. Diseases of the mitral valve in infancy an anatomic analysis of 55 cases. *Circulation*, 43(4):565–579, 1971.
- [180] V. Prot, R. Haaverstad, and B. Skallerud. Finite element analysis of the mitral apparatus: annulus shape effect and chordal force distribution. *Biomechanics and Modeling in Mechanobiology*, 8(1):43–55, 2009.
- [181] Z. He, M. S. Sacks, L. Baijens, S. Wanant, P. Shah, and A. P. Yoganathan. Effects of papillary muscle position on in-vitro dynamic strain on the porcine mitral valve. *The Journal of Heart Valve Disease*, 12(4):488–494, 2003.
- [182] P. F. Ferreira, P. D. Gatehouse, R. H. Mohiaddin, and D. N. Firmin. Cardiovascular magnetic resonance artefacts. *Journal of Cardiovascular Magnetic Resonance*, 15(1):41–79, 2013.
- [183] M. K. Rausch, W. Bothe, J. P. E. Kvitting, S. Göktepe, D. Craig Miller, and E. Kuhl. In vivo dynamic strains of the ovine anterior mitral valve leaflet. *Journal of Biomechanics*, 44(6):1149–1157, 2011.
- [184] M. Yin, X. Y. Luo, T. J. Wang, and P. N. Watton. Effects of flow vortex on a chorded mitral valve in the left ventricle. *International Journal for Numerical Methods in Biomedical Engineering*, 26(3-4):381–404, 2010.
- [185] M. Stevanella, G. Krishnamurthy, E. Votta, J. C. Swanson, A. Redaelli, and N. B. Ingels Jr. Mitral leaflet modeling: importance of in vivo shape and material properties. *Journal of Biomechanics*, 44(12):2229–2235, 2011.
- [186] M. S. Sacks, Y. Enomoto, J. R. Graybill, W. D. Merryman, A. Zeeshan, A. P. Yoganathan, R. J. Levy, R. C. Gorman, and J. H. Gorman III. In-vivo dynamic deformation of the mitral valve anterior leaflet. *The Annals of Thoracic Surgery*, 82(4):1369–1377, 2006.

- [187] J. H. Jimenez, S. W. Liou, M. Padala, Z. M. He, M. S. Sacks, R. C. Gorman, J. H. Gorman, and A. P. Yoganathan. A saddle-shaped annulus reduces systolic strain on the central region of the mitral valve anterior leaflet. *The Journal of Thoracic and Cardiovascular Surgery*, 134(6):1562–1568, 2007.
- [188] M. S. Sacks, Z. M. He, L. Baijens, S. Wanant, P. Shah, H. Sugimoto, and A. P. Yoganathan. Surface strains in the anterior leaflet of the functioning mitral valve. *Annals of Biomedical Engineering*, 30(10):1281–1290, 2002.
- [189] Z. M. He, J. Ritchie, J. S. Grashow, M. S. Sacks, and A. P. Yoganathan. In vitro dynamic strain behavior of the mitral valve posterior leaflet. *Journal of Biomechanical Engineering*, 127(3):504–511, 2005.
- [190] J. H. Jimenez, D. D. Soerensen, Z. M. He, S. Q. He, and A. P. Yoganathan. Effects of a saddle shaped annulus on mitral valve function and chordal force distribution: an in vitro study. *Annals of Biomedical Engineering*, 31(10):1171–1181, 2003.
- [191] T. Mansi, I. Voigt, B. Georgescu, X. Zheng, E. A. Mengue, M. Hackl, R. I. Ionasec, T. Noack, J. Seeburger, and D. Comaniciu. An integrated framework for finite-element modeling of mitral valve biomechanics from medical images: Application to mitralclip intervention planning. *Medical Image Analysis*, 16(7):1330–1346, 2012.
- [192] C. H. Lee, P. J. A. Oomen, J. P. Rabbah, A. Yoganathan, R. C. Gorman, J. H. Gorman III, R. Amini, and M. S. Sacks. A high-fidelity and micro-anatomically accurate 3d finite element model for simulations of functional mitral valve. In *Functional Imaging and Modeling of the Heart*, pages 416–424. Springer, 2013.
- [193] R. Ray and J. Chambers. Mitral valve disease. *International Journal of Clinical Practice*, 68(10):1216–1220, 2014.
- [194] K. S. Kunzelman and R. Cochran. Stress/strain characteristics of porcine mitral valve tissue: parallel versus perpendicular collagen orientation. *Journal of Cardiac Surgery*, 7(1):71–78, 1992.
- [195] C. A. Conti, M. Stevanella, F. Maffessanti, S. Trunfio, E. Votta, A. Roghi, O. Parodi, E. G. Caiani, and A. Redaelli. Mitral valve modelling in ischemic patients:

- Finite element analysis from cardiac magnetic resonance imaging. In *Computing in Cardiology*, pages 1059–1062. IEEE, 2010.
- [196] W. Sun, A. Abad, and M. S. Sacks. Simulated bioprosthetic heart valve deformation under quasi-static loading. *Journal of Biomechanical Engineering*, 127(6):905–914, 2005.
- [197] D. Kamensky, M. C. Hsu, D. Schillinger, J. A. Evans, A. Aggarwal, Y. Bazilevs, M. S. Sacks, and T. J. Hughes. An immersogeometric variational framework for fluid–structure interaction: Application to bioprosthetic heart valves. *Computer Methods in Applied Mechanics and Engineering*, 284:1005–1053, 2015.
- [198] K. D. Lau, V. Diaz, P. Scambler, and G. Burriesci. Mitral valve dynamics in structural and fluid–structure interaction models. *Medical Engineering & Physics*, 32(9):1057–1064, 2010.
- [199] S. K. Dahl, J. Vierendeels, J. Degroote, S. Annerel, L. R. Hellevik, and B. Skallerud. Fsi simulation of asymmetric mitral valve dynamics during diastolic filling. *Computer Methods in Biomechanics and Biomedical Engineering*, 15(2):121–130, 2012.
- [200] K. B. Chandran and H. Kim. Computational mitral valve evaluation and potential clinical applications. *Annals of Biomedical Engineering*, 43(6):1348–1362, 2014.
- [201] H. Gao, D. Carrick, C. Berry, B. E. Griffith, and X. Y. Luo. Dynamic finite-strain modelling of the human left ventricle in health and disease using an immersed boundary-finite element method. *IMA Journal of Applied Mathematics*, 2014.
- [202] H. Gao, C. Berry, and X. Y. Luo. Image-derived human left ventricular modelling with fluid-structure interaction. In *Functional Imaging and Modeling of the Heart*, pages 321–329. Springer, 2015.
- [203] H. M. Wang, H. Gao, X. Y. Luo, C. Berry, B. E. Griffith, R. W. Ogden, and T. J. Wang. Structure-based finite strain modelling of the human left ventricle in diastole. *International Journal for Numerical Methods in Biomedical Engineering*, 29(1):83–103, 2013.

-
- [204] S. A. Niederer, P. J. Hunter, and N. P. Smith. A quantitative analysis of cardiac myocyte relaxation: a simulation study. *Biophysical Journal*, 90(5):1697–1722, 2006.
- [205] A. Vahanian, H. Baumgartner, J. Bax, E. Butchart, R. Dion, G. Filippatos, F. Flachskampf, R. Hall, B. Iung, J. Kasprzak, et al. Guidelines on the management of valvular heart disease. *European Heart Journal*, 28(2):230–268, 2007.